



The  
University  
Of  
Sheffield.

**New Applications of Gas Phase Vibrational  
Spectroscopies in Biochemistry and  
Microbiology**

**Thomas William Smith**

*A thesis submitted in partial fulfilment of the requirements for the degree of  
Doctor of Philosophy*

The University of Sheffield  
Faculty of Science  
Department of Chemistry

September 2017



## Acknowledgements

Interdisciplinary collaboration is a great way to develop new avenues of research. My PhD research has certainly been highly interdisciplinary and has taken me into new areas. As a result, I've had to learn a great deal of new theory and practical skills, both in microbiology and molecular biology but also laser spectroscopy and optics.

From the spectroscopy side, I'd like to thank previous PhD student Dr. Johnny Chu for his practical help, encouragement and advice. I would also to thank Dr. Mark Stringer for his advice and Dr. Robert Salter for previously setting up the CERS apparatus described in Chapter 5.

From the microbiology side, I have to thank Professor Robert K. Poole and Professor Jeff Green for their support and help – none of this work would have been possible without them or their research groups. In particular I would like to thank Dr. Mariana Trajeo and Namrata Rata for teaching me most of what I know about practical microbiology, Dr. Wenjing Jia for her help in the nitrous oxide project, Hannah Southam for her sound advice and for working with me on carbon monoxide releasing molecules and Dr. Jonathan Butler for his advice on microbiology and helping me run my first gel.

I would also like to thank all of the support staff at Sheffield (particularly the stores staff and Dan Jackson, the departmental glassblower) and my friends for helping me during my PhD and the write-up period. I would like to thank both the Engineering and Physical Sciences Research Council (EPSRC) for funding my studentship and giving me the opportunity to carry out research at Sheffield as well as the Royal Society of Chemistry (RSC) for providing financial support to allow me to present my results at both national and international scientific conferences.

I would like to thank my family in Sheffield who have been a great support both before and during my PhD. Finally and perhaps most importantly I'd like to thank my supervisor, Dr. Michael Hippler, for his patience, support and advice during my PhD; I really couldn't have wished for a better supervisor for my PhD research.

## Abstract

Vibrational spectroscopy has a number of strengths which make it a powerful analytical tool such as high selectivity and sensitivity as well as the ability to distinguish different isotopomers and isotopologues. Unlike conventional gas detection techniques, vibrational spectroscopy can be used to monitor the headspace of a reactor or fermenter online and *in situ* with no sampling requirements, high time resolution and with little involvement from the user. These strengths make it particularly suited to monitoring rapidly evolving biological processes. This thesis describes a number of new applications of both Infrared and Raman spectroscopies in monitoring the production and consumption of gases by microorganisms and biologically relevant carbon monoxide (CO) releasing molecules (CORMs).

A new 8 meter path length multiple pass gas absorption cell is characterised and applied to the simultaneous detection of microbial nitrous oxide (N<sub>2</sub>O) and carbon dioxide (CO<sub>2</sub>) by Fourier Transform Infrared (FTIR) Spectroscopy. Distinct phases in both N<sub>2</sub>O and CO<sub>2</sub> formation are observed from anaerobic *Escherichia coli* treated with either nitrate or nitrite.

CO release from two metal-based CORMs has been measured using FTIR spectroscopy in the gas phase. [Mn(CO)<sub>3</sub>(tpa-κ<sup>3</sup>N)]Br, a promising antimicrobial agent, was found to release CO photolytically even in dense bacterial cell suspensions. [Ru(CO)<sub>3</sub>Cl(glycinate)] (CORM-3) was found to rapidly lose its ability to release CO via a dithionite / sulfite triggered mechanism in phosphate buffer, defined minimal salts medium and complex bacterial and mammalian media. The first report of photolytic CO release from CORM-3 is also reported.

Cavity Enhanced Raman Spectroscopy (CERS), is introduced in its first reported application in monitoring molecular hydrogen (H<sub>2</sub>) metabolism in anaerobic cultures of *E. coli*. Similar yields of H<sub>2</sub> are observed from glycerol and glucose. Using D<sub>2</sub>, hydrogen production and uptake by the bacteria have been monitored simultaneously. Both techniques show great promise as novel bioanalytical tools.

# Abbreviations

A	Adenine
Am	Ampicillin
APEC	Avian pathogenic <i>Escherichia coli</i>
AR	Anti-reflection (coating)
bp	Base pair
C	Cytosine
Cm	Chloramphenicol
CaF <sub>2</sub>	Calcium fluoride
CEAS	Cavity Enhanced Absorption Spectroscopy
CERS	Cavity Enhanced Raman Spectroscopy
CERPAS	Cavity Enhanced Resonant Photoacoustic Spectroscopy
CORM	Carbon monoxide releasing molecule
CRDS	Cavity Ring Down Spectroscopy
CW	Continuous Wave
DFB	Distributed feedback
DMEM	Dubleco's Modified Eagles Medium
DNA	Deoxyribonucleic acid
ECDL	External Cavity Diode Laser (or Extended Cavity Diode Laser)
FTIR	Fourier Transform Infrared
FWHM	Full width at half maximum
G	Guanine
GaN	Gallium nitride
Hz	Hertz
InGaAs	Indium Gallium arsenide
InP	Indium phosphide
K	Kelvin
Kan	Kanamycin

Kbp	Kilo base pair
kHz	Kilohertz
LB	Lysogeny broth (also commonly referred to Luria-Bertani media)
mbar	millibar
LOD	Limit of detection
Mbp	Mega base pair
MH2	Müller-Hinton 2
MHz	Megahertz
MIR	Mid Infrared
mRNA	Messenger ribonucleic acid
MRSA	Methicillin resistant <i>Staphylococcus aureus</i>
mV	millivolt
mW	milliwatt
NAD <sup>+</sup>	Nicotinamide adenine dinucleotide (oxidised)
NADH	Nicotinamide adenine dinucleotide (reduced)
NADP <sup>+</sup>	Nicotinamide adenine dinucleotide phosphate (oxidised)
NADPH	Nicotinamide adenine dinucleotide phosphate (reduced)
NIR	Near Infrared
OA-ICOS	Off Axis Integrated Cavity Output Spectroscopy
PCR	Polymerase Chain Reaction
PD	Photodiode
QCL	Quantum Cascade laser
Rif	Rifampicin
RNA	Ribonucleic acid
RPMI	Roswell Park Memorial Institute 1640 media
$\tau$	decay time
T	Thymine
$\mu$	micro
U	Uracil
UPEC	Uropathogenic <i>Escherichia coli</i>

V Volt

W Watt

# Table of Contents

Acknowledgements.....	3
Abstract .....	4
Abbreviations.....	5
Table of Contents.....	8
Chapter 1 – Introduction .....	13
1.1 Spectroscopic Approaches to Gas Analysis .....	13
1.1.1 Fundamentals of Vibrational Spectroscopy .....	13
1.1.2 Failings of the Harmonic Oscillator Approximation .....	16
1.1.3 Vibrational Selection Rules .....	18
1.1.4 Rotational Fine Structure .....	20
1.2 Approaches to Vibrational Spectroscopy for Gas Analysis .....	22
1.2.1 Direct Absorption using Fourier-Transform Infrared Spectroscopy.....	22
1.2.2 Multipass Cells.....	24
1.2.3 Cavity Ring-Down Spectroscopy (CRDS) .....	28
1.2.4 Cavity Enhanced Absorption and Related Techniques.....	31
1.2.5 Raman Spectroscopy.....	33
1.3 <i>Escherichia coli</i> : A Model Bacterium.....	38
1.3.1 (An)aerobic Respiration.....	38
1.4 Aims and Thesis Structure.....	43

Chapter 2 – Construction and Characterisation of a Long Path Multiple-Pass White Cell for FTIR Spectroscopy with Applications in Culture Headspace Analysis .....	45
Abstract .....	45
2.1 Introduction .....	46
2.1.1 Nitrosative Stress in <i>Escherichia coli</i> .....	46
2.1.2 Achieving High Sensitivity with FTIR Spectroscopy.....	49
2.1.3 Aims .....	51
2.2 Experimental.....	52
2.2.1 White Cell Components and Assembly .....	52
2.2.2 Path Length Determination .....	53
2.2.3 Measuring NO Reduction by Nitrate and Nitrite treated cultures.....	56
2.3 Results & Discussion.....	58
2.3.1 White Cell Construction & Visible Alignment.....	58
2.3.2 Path Length Calibration with N <sub>2</sub> O .....	61
2.3.3 FTIR Measurements of Endogenous NO Reduction .....	67
2.4 Conclusions and Future Work.....	70
Chapter 3 - Measuring CO Release from [Mn(CO) <sub>3</sub> (tpa-κ <sup>3</sup> N)]Br, a Novel Antimicrobial Compound, with Headspace FTIR Spectroscopy.....	73
Abstract .....	73
3.1 Introduction .....	74

3.1.1	Carbon Monoxide as a Therapeutic Agent.....	74
3.1.2	Carbon Monoxide Releasing Molecules (CORMs).....	75
3.1.3	CORMs as Antimicrobials.....	77
3.1.4	Headspace FTIR Spectroscopy for Monitoring CO Release.....	81
3.1.5	Aims.....	82
3.2	Experimental.....	83
3.2.1	CO Diffusion Calibration.....	83
3.2.2	Growth of Dense <i>E. coli</i> EC958 Broth Cultures.....	83
3.2.3	FTIR Headspace Measurements of CO Release.....	84
3.2.4	Hemochrome Assay.....	84
3.3	Results & Discussion.....	86
3.3.1	CO Diffusion & Short Pass Cell Characterisation.....	86
3.4	Conclusions.....	91

## Chapter 4 - CO Releasing Properties of the Water Soluble

### [Ru(CO)<sub>3</sub>Cl(glycinate)] (CORM-3) in Bacterial and Mammalian

Media.....	93
Abstract.....	93
4.1 Introduction.....	94
4.1.1 Ruthenium (II) CO Releasing Molecules CORM-2 and CORM-3.....	94
4.1.2 CORM-3 – A Molecule with Extensive Aqueous Chemistry.....	96
4.2 Experimental.....	97
4.2.1 General Procedure for FTIR Measurements of CO Release.....	97

4.2.2	Media and Buffers.....	98
4.3	Results & Discussion.....	99
4.3.1	CORM-3 CO Release is triggered by Sulfite and Dithionite.....	99
4.3.2	CORM-3 CO Release is not triggered by Amino Acids.....	99
4.3.3	CORM-3 is rapidly deactivated in Phosphate Buffers.....	100
4.3.4	CORM-3 is deactivated in Non-Buffered Saline.....	103
4.3.5	Does CORM-3 Release CO in Bacterial and Mammalian Media?.....	104
4.3.6	CORM-3 is a PhotoCORM.....	109
4.4	Conclusions & Future Work.....	110
<b>Chapter 5 - Application of Cavity Enhanced Raman Spectroscopy to Biohydrogen Detection.....</b>		<b>113</b>
	Abstract.....	113
5.1	Introduction.....	114
5.1.1	Hydrogenases and Biological Hydrogen Metabolism.....	114
3.1.5	Aims.....	118
5.2	Experimental.....	118
5.2.1	Cavity Enhanced Raman Spectroscopy with Optical Feedback.....	118
5.2.2	Media and Conditions for Routine Growth of Bacteria.....	124
5.2.4	CERS Hydrogen Metabolism Measurements.....	125
5.3	Results & Discussion.....	126
5.4	Conclusions.....	135
<b>Chapter 6 - Conclusions and Outlook.....</b>		<b>137</b>

References ..... 142

# Chapter 1 – Introduction

## 1.1 Spectroscopic Approaches to Gas Analysis

Spectroscopic detection of gases relies upon the interaction of electromagnetic radiation with the molecule(s) of interest. Unlike chromatographic techniques or mass spectrometry, spectroscopic techniques can be used to detect gaseous species *in situ* and non-destructively without the need for sampling, which can be a major advantage for monitoring processes with rapid or complex kinetics. While direct absorption measurements represent the most widely used and simplest approach to gas detection, other techniques such as photoacoustic (PA) spectroscopy and cavity-ring down spectroscopy (CRDS) can provide indirect but highly sensitive measurements of molecular absorption by gases. In addition, other optical techniques for gas analysis exist which rely upon completely different optical phenomena such as Raman scattering, where a small proportion of light is scattered with wavelength shifts which are characteristic of the analytes present in the sample.

### 1.1.1 Fundamentals of Vibrational Spectroscopy

Direct infrared (IR) absorption spectroscopy is the simplest and most widely employed method for optical detection of gases. While a small number of gases have absorption bands in visible and near-UV regions suitable for analytical applications, most small gaseous molecules only have intense electronic transitions close to or within the vacuum UV region. These bands are very broad, often overlapping with other atmospheric components making them not particularly useful for analytical applications.

Unlike absorption at visible or UV wavelengths, which occur due to transitions between electronic states, absorption of IR radiation by a molecule corresponds to transitions between two vibrational states of the molecule. Just as with electronic states, the vibrational energy of a molecule is quantised; it cannot take any arbitrary value but only specific values of energy. The energy provided to a system by absorption of a photon of frequency  $\nu$  (or energy lost by emission) is given by the Planck-Einstein relationship,

$$E = h\nu = \frac{hc}{\lambda} = hc\tilde{\nu} \quad \text{Equation 1}$$

where  $E$  is the energy of the photon and  $h$  is Planck's constant. The energy of a photon may also be expressed as a function of the wavelength ( $\lambda$ ) or wavenumber ( $\tilde{\nu}$ ) which are more commonly used quantities in molecular spectroscopy.  $C$  is the speed of light in a vacuum. As the absorption of light corresponds to transition between two states, the energy of an absorbed photon will correspond to the *difference* in energy between two states as opposed to the absolute energy any particular state, so that Equation 1 can be also be expressed,

$$\Delta E = h\nu = \frac{hc}{\lambda} = hc\tilde{\nu} \quad \text{Equation 2}$$

where  $\Delta E$  is the difference in energy between the two states. Since IR radiation is of much longer wavelength than visible or UV radiation, vibrational states are much closer in energy than electronic states. On the other hand, IR photons have much higher energies than either the microwave or radiowave photons used to probe transitions between molecular rotational states, electronic spins states (Electron Paramagnetic Resonance Spectroscopy, EPR) or nuclear spins states (Nuclear Magnetic Resonance Spectroscopy, NMR) which are much closer in energy.

The vibrational term values,  $G(v)$ , are the absolute energies of vibrational states expressed as a wavenumber. For a diatomic gas such as carbon monoxide (CO), only a single vibrational mode is present which corresponds to extension and compression along the molecular axis. To a first approximation, the vibrational states of a diatomic molecule can be described using a quantised form of the harmonic oscillator approximation,

$$G(v) = \left(v + \frac{1}{2}\right) \tilde{\nu} , \quad v = 0, 1, 2, \dots \quad \text{Equation 3}$$

where  $v$  is the vibrational quantum number which is assigned to vibrational states in order of increasing energy,  $G(v)$  is the vibrational term value and  $\tilde{\nu}$  is the fundamental vibrational frequency (usually expressed in  $\text{cm}^{-1}$ ) as given by

$$\tilde{\nu} = \frac{1}{2\pi c} \sqrt{\frac{k}{m_{\text{Reduced}}}}, \quad m_{\text{Reduced}} = \frac{m_1 m_2}{m_1 + m_2} \quad \text{Equation 4}$$

here  $k$  is the force constant of the bond,  $m_{\text{Reduced}}$  is the reduced mass,  $m_1$  and  $m_2$  are the masses of the two atoms and  $c$  is the speed of light in vacuum. Equation 3 predicts that for a molecule with a single vibrational mode, there is a series of vibrational states which are equally spaced in energy. Since the difference between  $G(0)$  and  $G(1)$  is equal to  $\tilde{\nu}$ , it implies that the energy of any IR photons absorbed must be equal to  $\tilde{\nu}$  for that particular molecule, so the absorption wavenumber is directly influenced by both the bond stiffness (which can be seen as a measure of bond strength) and reduced mass (which depends on the mass of the atoms involved in the vibrational mode). This forms the basis of molecular characterisation using IR absorption spectroscopy as, even in large molecules, many vibrational modes are highly localised to only few atoms. As a result, characteristic stretching and bending modes are observed in the spectra which are indicative of particular functional groups.

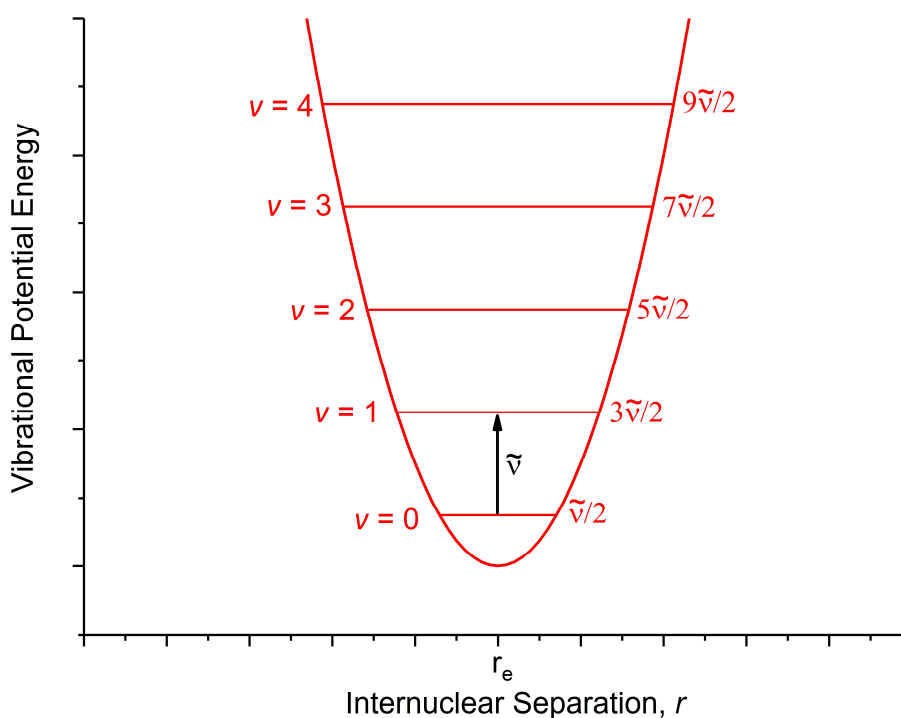


**Figure 1.1** – Harmonic vibrational potential as a function of internuclear separation for a one dimensional system (a diatomic molecule). The vibrational quantum number ( $\nu$ ) and state term values (expressed in terms of the fundamental frequency,  $\tilde{\nu}$ ) are shown next to their respective states. Note that the lowest vibrational state does not have zero energy but is in fact  $0.5 \tilde{\nu}$  above the bottom of the potential well.  $r_e$  is the equilibrium internuclear separation.

Due to the dependence of the fundamental vibrational frequency on the reduced mass, IR absorption and other forms of vibrational spectroscopy can be used to distinguish different isotopomers (e.g.  $^{12}\text{CO}_2$  and  $^{13}\text{CO}_2$ ). This enables these techniques to be employed for isotope labelling and tracer experiments, even with stable isotopes. As the isotopomer selectivity of vibrational spectroscopy is dependent upon the reduced mass, as opposed to the total mass of a molecular fragment or a molecular ion, vibrational spectroscopy is particularly sensitive to isotopic substitution involving light elements, such as proton / deuteron exchange. A novel labelling experiment which takes advantage of this shift is described in Chapter 5 of this thesis.

### 1.1.2 Failings of the Harmonic Oscillator Approximation

While the harmonic approximation reasonably describes vibrational behaviour of a molecule close to the equilibrium geometry, it fails to adequately describe the vibrational behaviour of a molecule in higher vibrational modes, where the internuclear separation is distorted far from the equilibrium bond length. The true vibrational potential energy surface is far steeper moving to smaller internuclear separations than moving to longer separation due to mutual repulsion between the electron clouds surrounding the two nuclei. In addition, the harmonic oscillator model predicts an entirely enclosed surface; the two nuclei can never dissociate, even at infinite internuclear separation. This prediction is clearly unphysical as bond dissociation will eventually occur if two nuclei are moved far enough apart.

The Morse potential provides a better description of the true potential energy surface,

$$V(r) = D_e \left(1 - e^{-\alpha(r-r_e)}\right)^2, \quad \alpha = \sqrt{\frac{k}{2D_e}} \quad \text{Equation 5}$$

where  $V(r)$  is the vibrational potential energy,  $D_e$  is the potential energy well depth,  $r$  is the internuclear separation,  $r_e$  is the equilibrium internuclear separation and  $k$  is the bond force constant. This function increases more rapidly in energy as  $r$  approaches

zero and approaches the well depth as  $r$  approaches infinity. The energies of the vibrational states is given by

$$G(\nu) = \left(\nu + \frac{1}{2}\right) \tilde{\nu} - \frac{\tilde{\nu}^2}{4D_e} \left(\nu + \frac{1}{2}\right)^2, \quad \nu = 0, 1, 2, \dots \quad \text{Equation 6}$$

where  $\nu$  is the vibrational quantum number which is assigned to vibrational states in order of increasing energy,  $G(\nu)$  is the vibrational term value and  $\tilde{\nu}$  is the fundamental vibrational frequency. The additional quadratic term means that, unlike the harmonic oscillator, the separation between vibrational states does not remain constant at the  $\nu_0$  but decreases with increasing quantum number. As can be seen in Figure 1.2, the Morse correctly predicts molecular dissociation as the curve becomes flat as the internuclear distance is increased, implying finite dissociation energy.

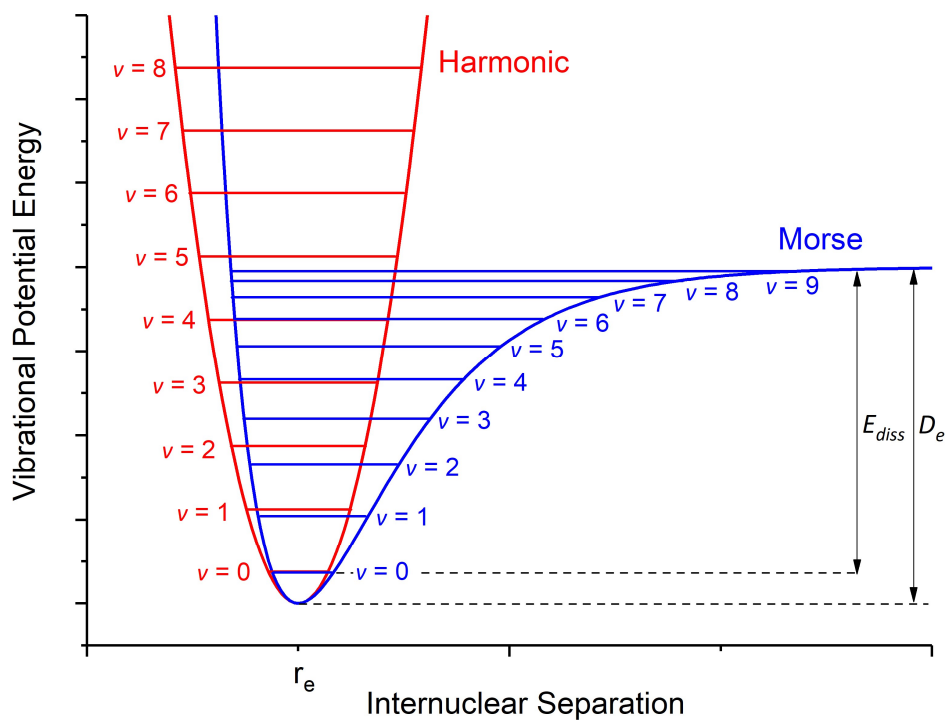


**Figure 1.2** – Comparison of the one dimensional harmonic and Morse potential energy curves for a diatomic molecule.  $E_{diss}$  is the true dissociation energy.

### 1.1.3 Vibrational Selection Rules

Absorption of IR radiation by a molecule leads to a transition between two vibrational states. However, not all transitions are equal; some transitions are completely forbidden while others are only weakly allowed, so that while they can still be observed with sensitive apparatus, the relative strength of the absorption band is low.

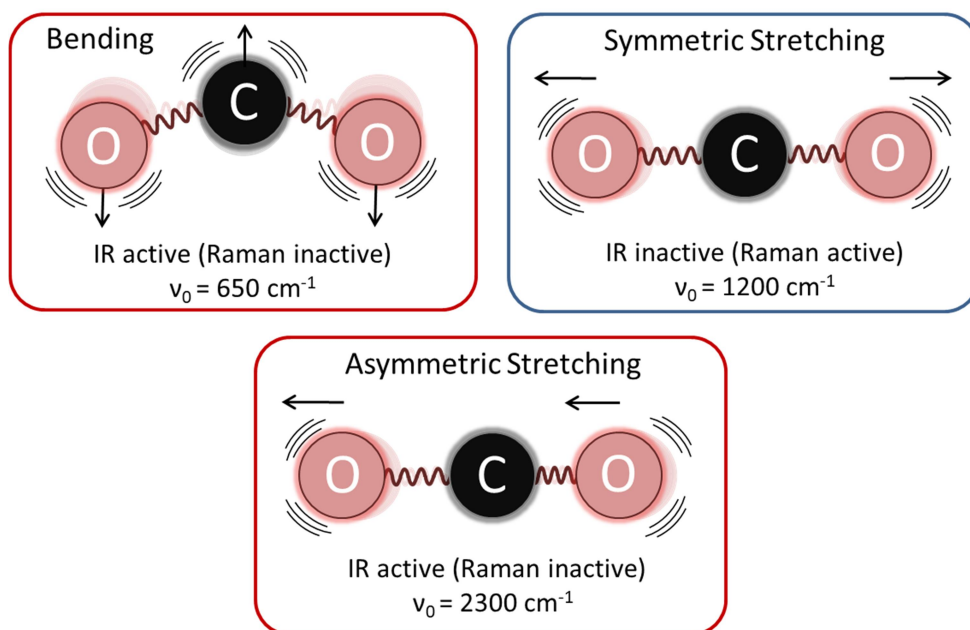


**Figure 1.3** – Vibrational modes of CO<sub>2</sub> and their fundamental frequencies expressed as a wavenumber value.

For a transition to be allowed through direct IR absorption there must be a change in electric dipole moment associated with the corresponding vibrational mode. The number of vibrational degrees of freedom is equal to  $3N - 5$  for a linear molecule and  $3N - 6$  for a non-linear molecule where  $N$  is the number of atoms in the molecule. Diatomic molecules ( $N = 2$ ) possess only one vibrational degree of freedom and a single vibrational mode. Heteronuclear diatomic molecules (e.g. CO, NO) satisfy the selection rule as they possess a permanent electric dipole moment; any change in the internuclear separation will necessarily give rise to a change in dipole moment. However, IR absorption is forbidden for homonuclear molecules (e.g. N<sub>2</sub>, O<sub>2</sub>) as the electric dipole moment remains zero irrespective of any distortion along the

bond axis. The excited vibrational states of homonuclear molecules can be accessed using Raman spectroscopy which is governed by different selection rules.

Polyatomic molecules possess multiple vibrational modes. Figure 1.3 shows the three non-degenerate vibrational modes of CO<sub>2</sub> and their fundamental frequencies. Although CO<sub>2</sub> actually possesses four vibrational degrees of freedom, two of these are degenerate bending modes which are observed at the same frequency but are mutually perpendicular to each other in space. At equilibrium, CO<sub>2</sub> has a zero electric dipole moment as the molecule is linear and both oxygen atoms lie the same distance away from the central carbon (i.e. the molecule is centrosymmetric). Bending and asymmetric stretching modes break this symmetry so that the two oxygen atoms are either no longer directly opposite each other or so that one oxygen is closer to the central carbon than the other, leading to a change in electric dipole moment. As a result, both the bending and asymmetric (or antisymmetric) modes are IR active and absorption bands corresponding to both bands can be observed in the IR. In contrast, while the symmetric stretching mode distorts the C=O bond lengths, it does so in a manner which preserves the symmetry of the molecule so that both bond lengths periodically increase and decrease together, leading to no change in electric dipole moment. Consequently, the symmetric stretching is IR inactive and there is no corresponding absorption band in the IR absorption spectrum. However, the symmetric stretching mode can be observed using Raman spectroscopy, while the other two modes are Raman inactive.

A somewhat less rigorous selection rule states that only transitions where the vibrational quantum number changes by one (i.e.  $\Delta V = \pm 1$ ) are allowed to occur. This means that IR absorption bands should only be observed at the fundamental frequency,  $\nu_0$ , which for most molecules falls within the range 250 – 4000 cm<sup>-1</sup> (40 – 2.5 μm), often referred to as the Mid-infrared (MIR) or fundamental region. Due to anharmonicity, this rule is partially relaxed so that higher overtone transitions ( $\Delta V = \pm 2, 3, 4\dots$ ) can be observed at higher frequencies. Nevertheless, these bands are typically orders of magnitude weaker than the corresponding fundamental bands. For modes with particularly high vibrational frequencies (C-H, N-H, O-H), all overtone transitions are found in the Near-infrared (NIR) region which extends from 4000 cm<sup>-1</sup> to around 14,000 cm<sup>-1</sup> at the edge of the visible region (2500 – 700 nm). In addition to overtone bands, weak combination bands can also be observed for polyatomic

molecules. These bands occur at frequencies corresponding to sums of the fundamental frequencies of different vibrational modes and correspond to excitation of multiple vibrational modes simultaneously.

#### 1.1.4 Rotational Fine Structure

When acquiring gas phase IR absorption spectra using equipment with reasonably high resolution, the appearance of additional fine structure within the absorption band is readily apparent. Linear molecules are the simplest case and are usually observed as two humps or branches of narrow lines which lie to either side of the centre of the vibrational fundamental frequency (Figure 1.4). This fine structure arises due to transitions between different rotational states which occur simultaneously with the vibrational transition. The separation of rotational states is considerably smaller than for vibrational states, typically only a few  $\text{cm}^{-1}$  for light molecules and less for heavier species. This energy difference is sufficiently small to ensure considerable thermal population of many of the higher rotational states at 298 K. This is in contrast to vibrational states where the difference between the ground and first excited state is usually large enough for negligible thermal population of the excited state.

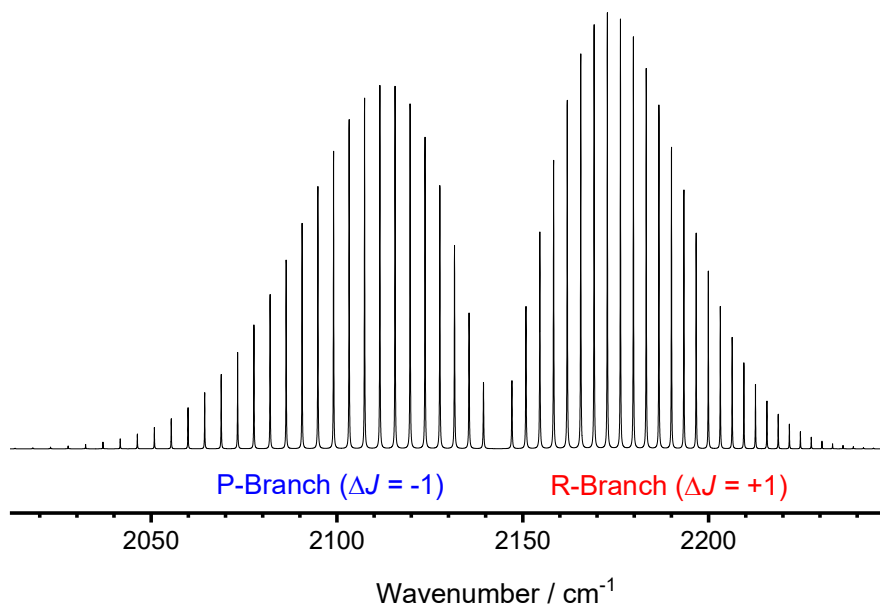


**Figure 1.4** – Simulated high-resolution fundamental absorption band of carbon monoxide (CO) generated using data from the HITRAN 2012 database.<sup>1</sup> The individual rotational lines forming *P*-branch ( $\Delta J = -1$ ) and *R*-branch ( $\Delta J = +1$ ) structures are clearly visible.

Like vibration, molecular rotation is also quantised, with each state having a rotational quantum number,  $J$ . The rotational term value,  $F(J)$ , can be approximated by,

$$F_v(J) = B_v J(J + 1) , J = 0, 1, 2, \dots \quad \text{Equation 7}$$

where  $F_v(J)$  is the rotational term value of the rotational state with rotational quantum number  $J$  in the vibrational state with quantum number  $v$ ,  $J$  is the rotational quantum number and  $B_v$  in the vibrational state with quantum number  $v$ . Note that unlike vibrational states, which to a first approximation are equally separated in energy, the spacing of rotational states increases with increasing  $J$ .

For vibrational bands in linear molecules where the change in dipole moment is along the internuclear axis, only  $\Delta J = \pm 1$  transitions are allowed, except if the molecule has non-zero electronic or vibrational angular momentum (e.g. radicals such nitric oxide, NO); in these cases,  $\Delta J = 0, \pm 1$ . Unlike vibrational states, there is considerable thermal population of rotational states above the ground state. This gives rise to a set of approximately equally spaced rotational lines in two branches corresponding to  $\Delta v = +1, \Delta J = +1$  transitions to higher wavenumbers (R-branch) and  $\Delta v = +1, \Delta J = -1$  to lower wavenumbers (P-branch). The individual lines of each branch are usually designated P(n) or R(n) depending on which branch the line is located in and the rotational quantum number of initial rotational state (e.g. the P(1) line corresponds to a transition from  $J = 1$  to  $J = 0$ ). For molecules where  $\Delta J = 0$  is also allowed, a third branch (the Q-branch) can be observed. This branch lies at the fundamental vibrational frequency and appears as a narrow, often unresolvable feature as opposed to the typically much broader P and R-branches.

In the case of Raman spectroscopy, transitions with  $\Delta J = +2, 0$  and  $-2$  are normally allowed for most vibrational modes (giving O, Q and S branches respectively). The Q-branch is usually extremely sharp and the dominant feature in most gas phase spectra. This can be a major advantage over direct absorption techniques as certain absorbers, most notably water vapour, have a large spread of rather intense rotational lines in their absorption spectra which make certain spectral region practically unusable in a water saturated environment.

## 1.2 Approaches to Vibrational Spectroscopy for Gas Analysis

### 1.2.1 Direct Absorption using Fourier-Transform Infrared Spectroscopy

Fourier Transform Infrared Spectroscopy (FTIR) is widely used for material characterisation, measuring reaction kinetics, functional group identification, process monitoring and a plethora of other tasks. While gas-phase analysis is something of a niche application, the technique has nevertheless found applications in atmospheric studies, reaction headspace monitoring and more fundamental studies on the nature of intra- and intermolecular interactions for simple model systems.<sup>2,3</sup>

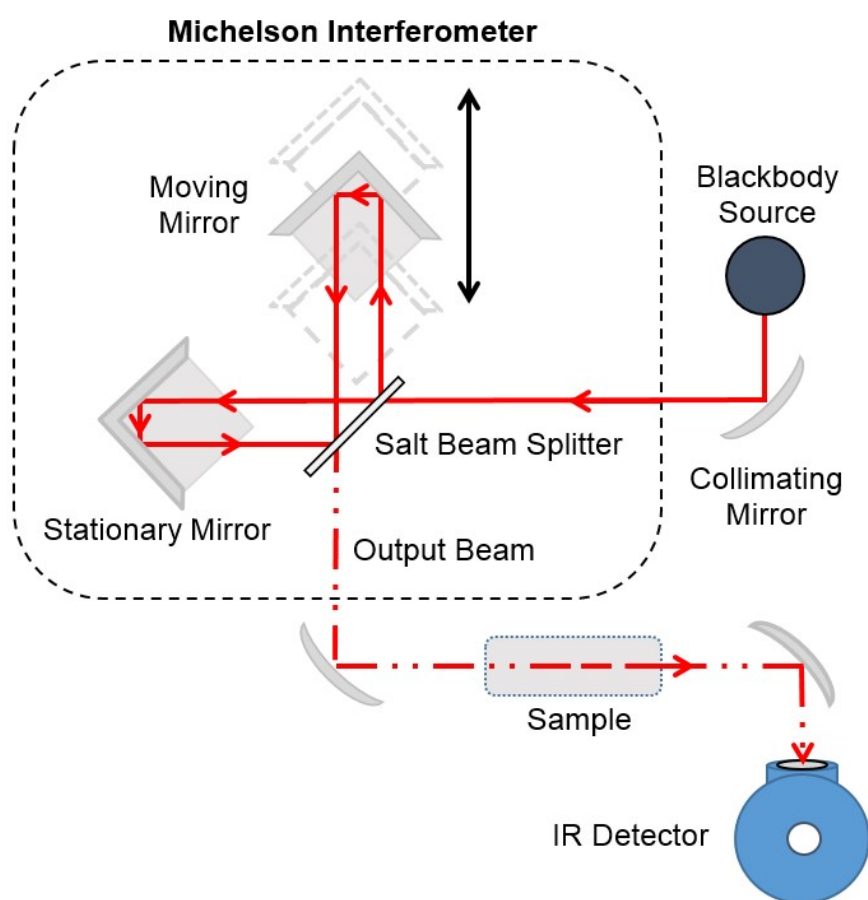


**Figure 1.5** – Outline of a typical FTIR Spectrometer. Rather than relying on a dispersive element, FTIR generates an interference pattern using a Michelson interferometer. This avoids the use of slits and increases the amount of light reaching the detector.

Rather than using a dispersive element such as a grating, FTIR spectroscopy relies upon the constructive and destructive interference of IR radiation (a blackbody source such as a globar) inside a Michelson interferometer. The interferometer consists of an IR-transparent salt beamsplitter (typically KBr) and a pair of retroreflecting mirror cubes which are used to split and then recombine the IR beam used to interrogate the sample. The outgoing beam can then be used for absorption measurements by passing it through a sample in exactly the same way as conventional absorption spectrometers. During a measurement, one of the retroreflecting mirrors cubes is moved back and forth so that the path length difference travelled by the two split beams is varied over time. At any given mirror displacement, certain wavelengths will constructively interfere at the beam splitter while other wavelengths will undergo destructive superposition; only wavelengths which are in phase when recombined at the beamsplitter will pass through to the sample.

As the mirror displacement is varied, different wavelengths fulfil the phase matching criteria. Only at zero path difference (ZPD) do all wavelengths combine constructively. The raw FTIR data is recorded as an interferogram which is a plot of intensity measured at the detector against mirror displacement. Although each point in the interferogram has intensity from multiple wavelengths, the way that the intensity of each wavelength varies as a function of mirror displacement will be different. This forms the basis of wavelength discrimination in FTIR spectroscopy. Fourier transformation of the interferogram is used to recover the 'normal' single beam spectrum of intensity as a function of wavenumber. Essentially the interferogram can be considered as a sum of many cosine functions, with each function corresponding to a single point within the 'normal' frequency domain spectrum.

While the Fourier transform approach may appear convoluted, it does offer several advantages over traditional dispersive instruments, most notably wavelength multiplexing ( Fellgett's advantage), enhanced light throughput as no slit is required (Jaquinot's advantage) and very high wavenumber accuracy and stability (Conne's advantage). The first two advantages essentially mean that more light hits the detector than in a comparable dispersive instrument, which is particularly advantageous in the MIR region where detectors are considerably less sensitive than photodiodes employed in the UV, visible and NIR regions. Although modern NIR and visible spectrometers equipped with CCD cameras and similar multi-pixel devices also

benefit from wavelength multiplexing, they can still only measure a relatively narrow range in one shot, normally sacrificing resolution to capture a large range of wavelengths. In contrast, interferometric techniques such as FTIR measure all wavelengths simultaneously (within the working wavelength range of the detector and light source).

The very high wavenumber accuracy is governed by a reference laser source with a well-defined emission wavelength which is also passed through the interferometer, typically a 632.8 nm HeNe laser. As the laser is monochromatic and the wavelength is much shorter than the IR radiation, a single sinusoidal interference pattern with a comparatively high frequency is observed. The zero-point crossings of this sinusoid are then used to time data acquisition with very high precision. Note that the reference wavelength provides a theoretical limit to the range an FTIR as shorter wavelengths cannot be discriminated; in practice, the detector and blackbody light source performance limits most instruments to wavelengths far longer than the commonly employed 632.8 nm HeNe emission.

### 1.2.2 Multipass Cells

A major challenge which faces all forms of gas analysis with samples at ambient pressures is the relatively low density of the gas phase. Preconcentration methods using chemical or cryogenic traps can be employed for spot sampling (e.g. atmospheric studies) but is completely inappropriate for monitoring rapidly evolving processes occurring in closed systems (which includes all of the systems addressed in this thesis). The most common method for achieving higher sensitivities with optical techniques is to increase the sample path length. According to the Beer-Lambert-Bouguer law,

$$I = I_0 e^{-\sigma[c]l} \quad \text{Equation 8}$$

where  $I_0$  is the initial intensity,  $I$  is the intensity after the absorbing medium,  $\sigma$  is the absorption cross-section,  $[c]$  is the concentration of the analyte and  $l$  is the sample depth or absorption path length. Absorbance is defined, using the natural logarithm,

$$A = \sigma[c]l = \ln\left(\frac{I_0}{I}\right) \quad \text{Equation 9}$$

or alternatively, using the decadic logarithm,

$$A = \varepsilon[c]l = \log\left(\frac{I_0}{I}\right) \quad \text{Equation 10}$$

In this thesis, the natural logarithm form is employed for all gas phase measurements for consistency with the majority of high resolution gas phase databases which use absorption cross-sections based on the natural logarithm form. While the absorbance measured at the peak of one particular feature can be a very quick way of determining sample concentration in solution, the peak intensities of gas phase samples in IR absorption spectroscopy are strongly dependent upon the total pressure of the sample due to pressure broadening effects. For gaseous samples, it is often better to use the integrated absorbance of a selected line or band as this is entirely independent of total pressure.

$$\int_a^b A d\tilde{\nu} = [c]l \int_a^b \sigma d\tilde{\nu} \quad \text{Equation 11}$$

where,  $a$  and  $b$  are the start and end wavenumber of the line or band of interest and all other variables are as previously defined. Many of the integrated absorption coefficients for rotational lines in the IR spectra of small molecules are known to a high degree of accuracy as detailed knowledge of their spectra is particularly important for atmospheric studies.

One method for increasing the sensitivity of absorption measurements is to increase the sample path length. As maintaining as low a sample volume as possible is important to avoid dilution effects, multiple pass cells which use two or more mirrors to reflect the IR beam back and forth through the same sample and the preferred means of improving sensitivity. The White cell, originally described by J. White in 1942, is the most commonly used multipass design for FTIR spectroscopy.<sup>4</sup> The basic design is shown in Figure 1.6. With careful alignment, White cells with path lengths of tens of meters can be achieved within a sample volume only a few tens of centimetres in length. Some of the longest path lengths reported are over 100 m, although these systems typically have complex mirror arrangements.<sup>5</sup>

The simplest White cell design is based around three concave mirrors arranged in a V-shaped configuration within a sealed enclosure. Steering mirrors are usually employed to divert the IR beam into and out of the measurement cell. Sealing the mirrors inside the system is normally preferred as this significantly reduces transmission losses which would be incurred from multiple passes through the cell windows. After entering the cell, the beam is reflected back and forth between the two upper mirrors (A and C) and the lower mirror (B) known as the field mirror. All three mirrors have the same focal length and are separated at twice the focal length (the radius of curvature). The total number of passes is dictated by the how mirrors A and C are angled relative to the incoming and outgoing beam.

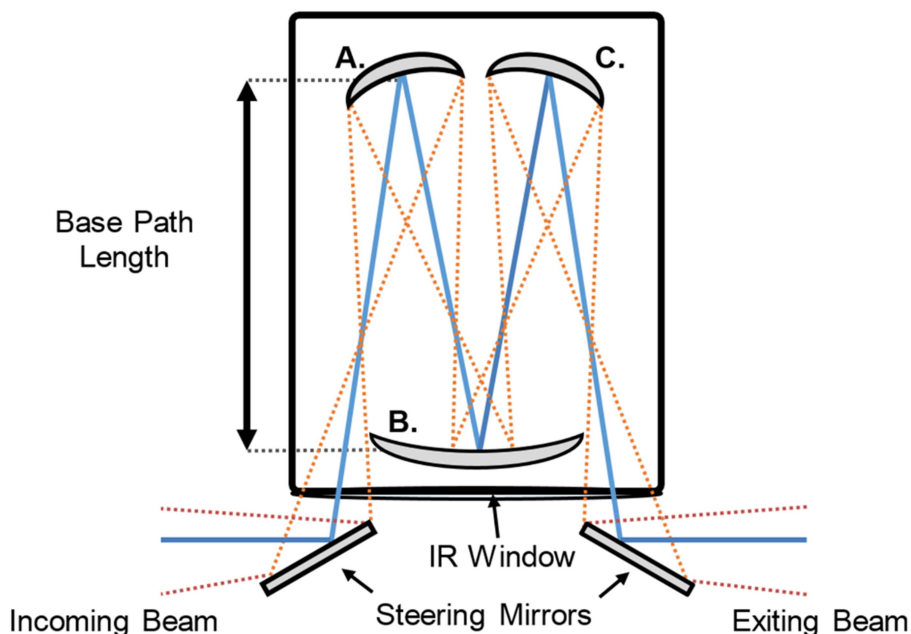


**Figure 1.6** – The basic design of a four pass White gas cell. The cavity consists of three concave mirrors, A, B and C, with the same focal length. Blue solid lines show the path taken by an idealised ray of light; the red dashed lines show more realistic behaviour the beam from an FTIR spectrometer. Due to the arrangement of mirror foci, the image of the entrance aperture is always brought to focus on the lower field mirror. The grey line indicates the sealed volume of the gas cell.

The Herriott cell is the second most widely used multipass design.<sup>6</sup> This multipass cell consists of concave mirrors with identical focal lengths arranged to form a linear

cavity, as shown in Figure 1.7. A small hole is cut in one of the mirrors and the input beam is injected through it at an angle to the optical axis of the cavity. The light is then continually reflected back and forth between the two mirrors before exiting through a second hole cut in either of the two mirrors. Alternatively, the output beam can simply exit through the input hole at a different angle to input beam. The total number of passes can be varied simply by changing the separation of the two mirrors. While the Herriott design is optically much simpler than the White cell, the former design requires the use of low numerical aperture beams for efficient coupling into the cavity. This makes it unsuitable for use with FTIR spectrometers where the beam diameter is quite large. Instead, the Herriott cell is better employed for laser-based absorption measurements where the beam profile of the light source is much narrower, meaning that it can be efficiently coupled into the cell.

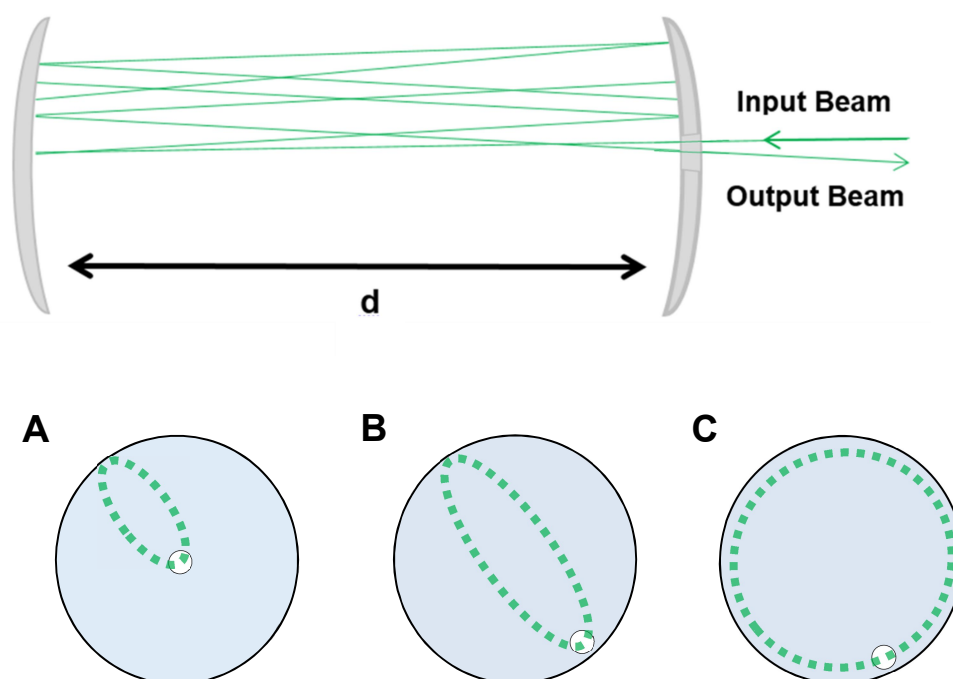


**Figure 1.7** – Top: the basic Herriott cell design consists of two opposing concave mirrors typically with one or more apertures cut into a mirror to allow beam injection. Bottom: pattern of reflections on the input mirror side of a Herriott cell. The reflection patterns for different mirror configurations where the output and input hole is the same are shown. **A** Injection hole is placed at the centre of the mirror. **B** Placing the injection hole at the edge of the mirror uses the mirror more efficiently. **C** Careful alignment of the mirrors can lead to a circular arrangement of reflections, further increasing the number of passes.

### 1.2.3 Cavity Ring-Down Spectroscopy (CRDS)

Cavity Ring-Down Spectroscopy (CRDS) is the most widely used form of resonant cavity enhanced spectroscopy and can trace its routes to a serendipitous discovery made in 1980 by Herbelin *et al.* while developing a novel method for testing high reflectivity mirror coatings based on how long a pulse of light could be stored within a cavity formed from the mirrors.<sup>7</sup> They found that the lifetime of light stored within the cavity after the pumping laser source was switched off varied depending on the local air quality, with higher concentrations of absorbing pollutants significantly shortening the lifetime of light stored within the cavity. This approach was developed and refined by Anderson *et al.* and Crawford *et al.* although they were still largely interested in measuring the reflectance of the high performance mirrors which made up the cavity.<sup>8,9</sup> O’Keefe and Deacon described the first application of high-finesse cavity decay measurements for spectroscopic applications, specifically detection of an extremely weak magnetic dipole transition in O<sub>2</sub>, demonstrating how the technique could be used to detect even weakly absorbing bands.<sup>10</sup> Since then, CRDS has remained one of the most sensitive techniques for optical detection of gaseous species, being successfully employed for the study of molecular clusters in jet expansions<sup>11</sup>, measurement of weak overtone and combination transitions<sup>12,13</sup> and studies of short lived radical species generated during photolysis<sup>14</sup> and in combustion processes.<sup>15,16</sup> In addition to fundamental chemical physics, CRDS has also been employed for environmental trace gas monitoring<sup>17–19</sup>, isotopic tracer studies<sup>20</sup> and breath analysis.<sup>21–23</sup>

In CRDS, a laser (either a continuous wave, CW, or pulsed source) is directly injected into a high finesse cavity formed from two or sometimes three high reflectivity (> 99.98 %) mirrors. Since the mirror losses are extremely low, once inside the cavity, the laser light can be reflected back forth many thousands of times. This means that, even when the light source is switched off or removed, appreciable intensity can remain inside the cavity for tens or even hundreds of microseconds.

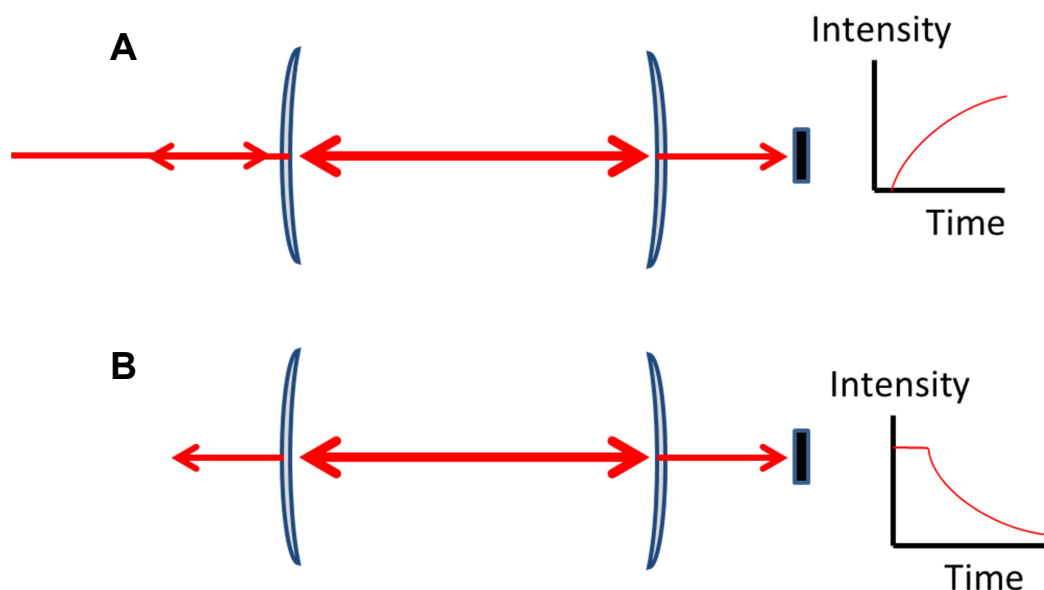


**Figure 1.8** – Simple schematic of CRDS in a two mirror cavity. **A** While the pumping light source remains on, light is continually injected into the cavity through one of the two mirrors and the intracavity intensity increases until a steady state is achieved between optical pumping and losses due to mirror transmission (which occurs through both mirrors), absorption and scattering losses. **B** Upon removal of the pumping light, the intensity of light within the cavity (and the intensity of light leaking through the mirrors) decreases exponentially. By measuring the lifetime in the presence and absence of an absorbing analyte, the concentration of the analyte can be determined.

In CW CRDS schemes, light is continuously injected into the cavity until it reaches a steady state where the rate of light loss from inside the cavity is equal to the rate of injection into the cavity. At this point, the laser source is rapidly switched off (using either a Pockels cell or acousto-optic modulator) or the cavity length or laser wavelength is slightly detuned so that the resonance conditions are no longer fulfilled. If a photodiode is placed on the opposite side of the cavity to the laser source, the resulting decay in light exiting the cavity can be measured. Pulsed CRDS schemes work in a similar manner except that injection into the cavity only occurs over the duration of the pulse and the resulting decay (the ring-down event) is a necessary implication of the pulsed nature of the light source.

By comparing the rate of decay in the empty cavity (i.e. inside an evacuated system) with the rate of decay when an absorbing analyte is present between the two mirrors, it is possible to determine the concentration of the absorption species. During

the a ring-down event, the intensity of light leaving the cavity at time  $t$  after the laser is taken out of resonance with the cavity is given by an exponential decay,

$$I = I_0 e^{-\frac{t}{\tau}} \quad \text{Equation 12}$$

where  $I_0$  is the initial intensity exiting the cavity at the beginning of the decay and  $\tau$  is the ring-down time which is dependent upon various losses within the cavity. For a simple linear (two mirror) cavity sat within an enclosure with no absorbing species, the ring down time is given by

$$\tau_0 = \frac{l}{c(1-R)} \quad \text{Equation 13}$$

where  $l$  is the cavity length,  $c$  is the speed of light in a vacuum and  $R$  is the mirror reflectivity. When an absorbing species is present, the ring down time is shorter due to the additional absorption losses and is given by

$$\tau = \frac{l}{c(1-R+\sigma[c]l)} \quad \text{Equation 14}$$

where  $\sigma$  is the absorption cross-section and  $[c]$  is the concentration of analyte. As CRDS relies on measuring ring-down times rather than any discrete intensity, the technique is insensitive to large variations in initial intensity within the cavity at the start of a ring-down event. This is particularly advantageous when the cavity is pumped with sources which have highly variable outputs, particularly pulsed lasers which are nevertheless advantageous for some applications due to their large spectral range. This is a major advantage over other cavity enhanced techniques and direct absorption spectroscopy which rely upon measuring intensity as a function of wavelength rather than a decay constant and therefore require stable light sources. From comparison of Equation 13 and 14 it can be shown that

$$\sigma[c] = \frac{1}{c\tau} - \frac{1}{c\tau_0} \quad \text{Equation 15}$$

where all terms are as previously defined. In practice, this method can be used to detect weak absorption features, far below noise floor of conventional absorption measurements, either from an intrinsically weak absorption band (e.g. a weak formally

forbidden transition) or to measure very low concentrations of gaseous species utilising a stronger absorption band to maximise sensitivity.

#### **1.2.4 Cavity Enhanced Absorption Spectroscopy (CEAS) and Related Techniques**

While CRDS represents the most widely used form of cavity enhanced spectroscopy for gas sensing applications, there are other techniques which utilise high finesse cavities either for the extreme path length enhancement (the average mean trip of a photon around a cavity can be a thousand times or more) or for the large intracavity optical powers which can be generated. Integrated Cavity Output Spectroscopy (ICOS), sometimes referred to as Cavity Enhanced Absorption Spectroscopy (CEAS), is a more conventional approach as the intensity of light transmitted through the cavity *during* resonance is measured as a function of wavelength as opposed to the decay measured in the case of CRDS.<sup>24</sup> The path length enhancement of up to several kilometres provided by resonant cavities is sufficient to directly observe extremely weak absorption bands while the cavity remains in resonance. ICOS is somewhat simpler than CRDS to implement from the point of view of data acquisition and processing; as ICOS relies upon simply measuring the light transmitted during resonance (which can be stable for minutes), there is no need for the high time resolution or careful synchronisation to ring-down events which is required for CRDS where typical ring-down times are of the order of microseconds. The process of fitting an exponential function also introduces an additional data analysis step to CRDS in order to obtain a ‘normal’ absorption spectrum; ICOS simply collects intensity data which can be used to plot simple single beam spectra with little or no data processing. On the other hand, while CRDS is immune to fluctuations in source intensity, the integrated signal measured after the cavity in ICOS is strongly dependent on the intensity of light entering the cavity and is therefore more suited to light sources with stable output power such as CW diode lasers.

CW diode lasers are particularly attractive for cavity enhanced laser spectroscopy and gas sensing in general as they have a very small footprint, low power consumption, relatively low cost, large number of supported wavelengths (from the MIR to near-UV) and the ability to tune the laser wavelength through changes in

temperature or by feedback from an optical element such as a diffraction grating. While the wide tunability of diode lasers can be extremely beneficial for gas sensing as it allow for scanning over a narrow range to capture the fine rotational detail of a vibrational band, it also means that the laser wavelength can shift very easily with changes in ambient temperature leading to the cavity falling out of resonance with the laser. Electronic locking approaches such as the Pound-Drever-Hall (PDH) locking technique or optical feedback can be used to force the diode laser to lase in resonance with the cavity so that the cavity up-time can be maximised.<sup>25,26</sup> In practice, some sort of locking technique is essential for successful implementation of ICOS in high finesse cavity enhanced schemes.

Off-axis approaches, where the beam is injected at a considerable angle to the optical axis of the cavity in a similar manner to the Herriot multypass design, have significantly higher stability than ICOS schemes where the beam is coupled along the optical axis into only the fundamental Gaussian ( $TEM_{00}$ ) mode.<sup>27</sup> While the off-axis approach leads to a slight reduction in path length enhancement, there is a significant gain in resonance stability and the typical path length enhancements are still orders of magnitude higher than those obtained in conventional multipass cells. Off-axis ICOS and CRDS technology has already been commercialised, the added stability over on-axis approaches being particularly attractive to ensure rugged and reliable operation for field measurements. While CRDS and ICOS approaches are the most widely reported cavity enhanced techniques, there are many different approaches to their implementation and many other cavity enhanced techniques which are too numerous to list here, although several excellent reviews have been published. A few notable examples which will be mentioned here are the use of high finesse cavities for photoacoustic spectroscopy<sup>28,29</sup> and their application to Raman spectroscopy.<sup>30</sup> Cavity Enhanced Raman Spectroscopy (CERS) is a comparatively new technique and is the focus of Chapter 5 where its operation is described in detail. The basic underlying principle of Raman spectroscopy is discussed in the next section.

### 1.2.5 Raman Spectroscopy

The inelastic scattering of light by materials was first predicted by Adolf Smekal in 1923.<sup>31</sup> However, the effect was first observed in liquids by Chandrasekhara V. Raman with his student Kariamanickam S. Krishnan and independently in crystalline samples by Grigory Landsberg and Leonid Mandelstam.<sup>32,33</sup> Somewhat controversially, only Raman was awarded the 1930 Nobel Prize in Physics for the work. Raman spectroscopy is often described as being complementary to IR absorption; while it probes vibrational and rotational states as in IR spectroscopy, the underlying principle, practical implementation and selection rules are distinct from IR absorption techniques

In Raman spectroscopy, a UV, visible or NIR laser is used to illuminate the sample of interest while scattered light is collected and either dispersed in a conventional grating spectrometer or passed through an interferometer analogous to FTIR before detection using a camera, photodiode or photomultiplier tube. The vast majority of photons are scattered elastically (i.e. with no change in energy), referred to as Rayleigh scattering. Spectroscopically, this is simply observed as a narrow band at the same wavelength as the laser source. In addition to Rayleigh scattering, there are also extremely weak bands to either side of the excitation frequency which arise due to Raman (elastic) scattering where energy is transferred from the scattered photon to excite the molecule to a higher energy vibrational state (Stokes) or, for vibrational states with none negligible thermal population, energy is transferred from a vibrationally excited state to the scattered photon (Anti-Stokes). Since the Stokes emission arises from transfer of energy to the molecule, the scattered photons are necessarily of lower energy than the excitation light and therefore redshifted. Likewise, as Anti-Stokes emission essentially ‘borrows’ energy from a low lying vibrational state, the photon energy is higher and the emission wavelength blueshifted.

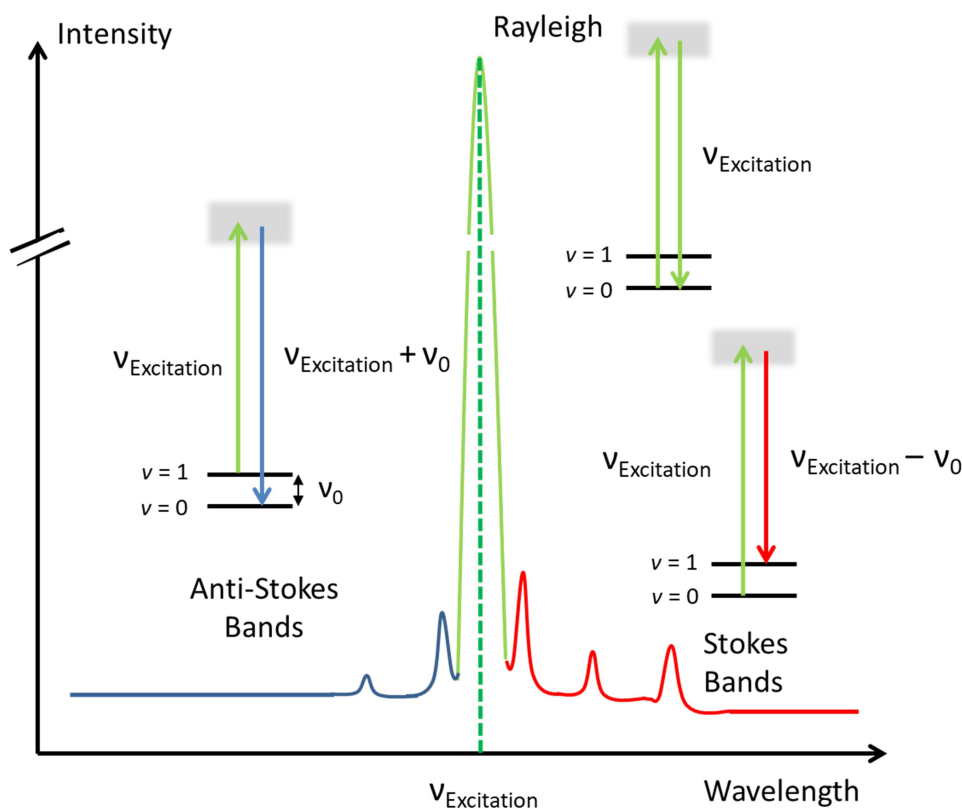


**Figure 1.9** – Depiction of Raman (Stokes and Anti-Stokes) and Rayleigh scattering as observed in a typical Raman spectrum along with the two photon transitions which give rise to the observed bands. Elastic Rayleigh scattering at the excitation frequency is the most likely occurrence and dominates the spectrum. A very small proportion of scattered photons are scattered with either loss of energy to (Stokes) or gain of energy from (Anti-Stokes) the molecule, resulting in a red- or blueshift respectively in the scattered light.

Unlike direct absorption, Raman scattering is a two photon process which occurs via an extremely short lived ( $\tau < \text{fs}$ ) virtual state, which is in reality an electronic state or collection of electronic states which are broadened due to the rapid interaction. This contrasts with fluorescence where the excited singlet state has a short but measurable lifetime, usually in the nanoseconds, and is therefore far better defined. The practical implication of this is that, while fluorescence normally requires that the fluorophore of interest must be excited within a particular wavelength band, the precise excitation wavelength employed for Raman is not absolutely critical. Whereas the fluorescence emission spectrum of a given fluorophore occurs at a fixed wavelength and will only change in intensity as the excitation wavelength is shifted, any Raman emission will move with the excitation wavelength so that the difference in wavenumber (and

therefore difference in energy) between scattered and excitation light remains constant for any given band. As a result, Raman spectra are normally plotted against Raman shift or the wavenumber shift from the excitation wavenumber. This allows spectra recorded at different excitation wavelengths to be easily compared, as the Raman shift will be identical, and also allows direct comparison with IR absorption spectra as both the IR absorption wavenumber and Raman shift of any given band should be identical.

As with direct IR absorption, Raman is governed by a number of selection rules. The selection rule relating to changes in rotational energy occurring alongside vibrational transitions in the case of Raman has already been discussed (namely that  $\Delta J = 0, \pm 2$ ). For any given vibrational transition to be allowed there must be a change in polarizability associated with the vibrational mode. For centrosymmetric molecules (e.g. CO<sub>2</sub>, HCCH, H<sub>2</sub>, N<sub>2</sub>, O<sub>2</sub>), the IR and Raman selection rules are mutually exclusive (see Figure 1.3 for an example of this). For non-centrosymmetric molecules (e.g. CO, HCl, N<sub>2</sub>O, H<sub>2</sub>O) this is not the case and all vibrational modes give rise to transitions which can be observed in both IR and Raman spectra. The ability of Raman spectroscopy to detect homonuclear diatomic molecules is a particular advantage for gas sensing, opening up a number of other potential applications such as monitoring hydrogen isotopomers released from nuclear fuels, probing biological nitrogen fixation and monitoring industrial processes utilising H<sub>2</sub> as a reductant. Raman spectroscopy is also relatively insensitive towards water vapour. As common Raman excitation wavelengths are in the visible and NIR regions, the optics and detectors employed are usually cheaper and provide better performance than their counterparts in the MIR region.

Unlike diode laser absorption approaches, which require the laser to be tuned over the absorption feature, Raman spectroscopy can capture an entire spectrum containing multiple components with no scanning. A major technical limitation of laser based multipass and cavity enhanced absorption schemes is that spectral bandwidths beyond a few hundred cm<sup>-1</sup> cannot be achieved using a single diode laser. To obtain a larger scanning range, multiple diodes are required, increasing the system's cost. For Raman spectroscopy, only a single laser is required with good wavelength stability but no requirement for tuning. As a result solid state rare-earth doped lasers, which have much higher central wavelength stability but lack the tuning ability of diode lasers, are often preferred for Raman applications. Neodymium-doped yttrium aluminium garnet

(Nd:YAG or Nd:YAlO<sub>4</sub>) and yttrium vanadate (Nd:YVO<sub>4</sub>) lasers are widely used, both at their fundamental wavelength (1064 nm) and shorter wavelength harmonics (particularly the first harmonic, the 532 nm emission line also used in laser pens).

While Raman spectroscopy retains the extremely high selectivity of direct IR absorption, the intrinsic weakness of the Raman effect limits sensitivity. Sensitive cooled detectors or photomultipliers alongside high performance blocking filters with excellent rejection of the excitation light are usually required to acquire spectra even in the most favourable of cases. Raman signals can be enhanced by moving away from spontaneous Raman scattering to a more efficient technique such as Resonant Raman (where the excitation wavelength is carefully chosen so that it matches an electronic transition of the molecule of interest) or Stimulated Raman (where a second laser is employed at the scattered wavelength) and while these techniques can improve sensitivity by orders of magnitude, they remove a major advantage of spontaneous Raman spectroscopy, specifically its ability to detect all components in a mixture simultaneously. New developments in Raman such Surface Enhanced Raman Spectroscopy (SERS) allows for extremely sensitive detection of analytes.<sup>34,35</sup> Surface enhancement is usually observed for analytes adsorbed to a roughened or nanostructured noble metal surface, possibly through some enhancement from surface plasmon resonance effects. While the sensitivity gained from SERS is immense, analytes must be chemically or physically adsorbed to the metal surface. Since different substrates will have different affinities for the surface and there is a considerable risk that a surface may become contaminated or poisoned, SERS is not particularly well suited to quantitative real-time monitoring processes particularly if analytes with extremely high affinities for typical metal substrates (e.g. amines, thiols, phosphines) are present in the system.

The simplest approach to improving the sensitivity of spontaneous Raman spectroscopy extremely powerful laser sources (e.g. several W CW solid state lasers) as the number of Raman scattered photons increases with the number of scattering events. Raman scattering also has a  $\lambda^{-4}$  dependency on the excitation wavelength, so moving to shorter wavelength excitation should improve sensitivity (assuming the same optic, grating and detector performance). While fluorescence at shorter wavelengths is a major issue for most Raman applications, it is less problematic in the

gas phase meaning that shorter wavelength sources can be employed with relatively little danger of the Raman signals becoming drowned out by background fluorescence.

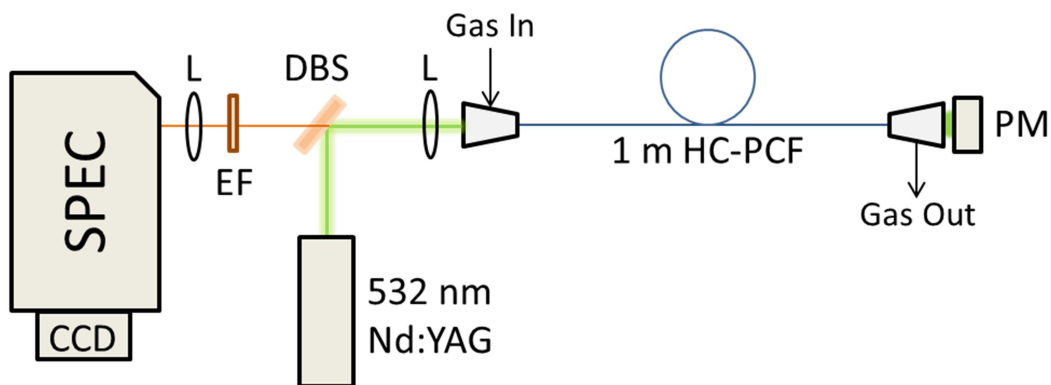


**Figure 1.10** – Typical FERS setup based on Hanf *et al.* A powerful laser source (in this case a frequency doubled Nd:YAG) is coupled into a length of hollow core photonic crystal fiber (HC-PCF) *via* a microscope objective. Gaseous analyte is flowed along the fiber. Power monitor **PM** allows total power transmitted through the fiber to be measured. In this configuration, back scattered Raman light is passed back through the objective and is transmitted through dichroic beamsplitter **DBS** (the excitation light is selectively reflected by this beamsplitter). Edge filter **EF** is employed to remove remaining excitation light before light is focused into a dispersive spectrometer equipped with a CCD detector.

Fiber-Enhanced Raman Spectroscopy (FERS) is a recently introduced approach where a hollow core photonic crystal fiber (HC-PCF) to trap the excitation light along with the gaseous analyte (see Figure 1.10 for a typical setup).<sup>36,37</sup> The resulting Raman scattered light is also confined within the fiber rather than being scattered isotropically, meaning that a much larger proportion of the light can be collected than using conventional optics. Using this approach and 2 W 532 nm excitation, detection limits of below 20 ppm have been reported for a number of gases.<sup>37</sup> FERS has also been successfully employed for breath analysis, where the ability to detect H<sub>2</sub> (an important product and metabolite of strict and facultative anaerobes) could be a potential over other optical techniques.<sup>36</sup>

Multipass and cavity enhanced schemes have been reported for Raman gas analysis, the extended path lengths allowing for more interaction events and therefore a noticeable enhancement in Raman scattered light. A number of groups, including the Hipper group, have demonstrated how resonant cavities similar to those employed in CRDS can be used to obtain a large enhancement in Raman scattering.<sup>30,38–40</sup> Cavity

Enhanced Raman Spectroscopy (CERS) has been employed for natural gas and fuel analysis and for a number of isotopic labelling studies utilising  $^{14}\text{N}$  and  $^{13}\text{C}$  sources. Chapter 5 describes the first application of CERS to the study of a model biological system for hydrogen metabolism and sustainable ‘biohydrogen’ production.

## 1.3 *Escherichia coli*: A Model Bacterium

### 1.3.1 (An)aerobic Respiration

*Escherichia coli* is a Gram-negative facultative anaerobe which physically appears as approximately  $1\ \mu\text{m}$  long rods which elongate during the course of the cell cycle before dividing. Many strains are motile, possessing multiple flagella which aid in cell movement towards source of nutrients (chemotaxis). The bacterium contains a single circular chromosome of approximately 4.6 Mbp in length.

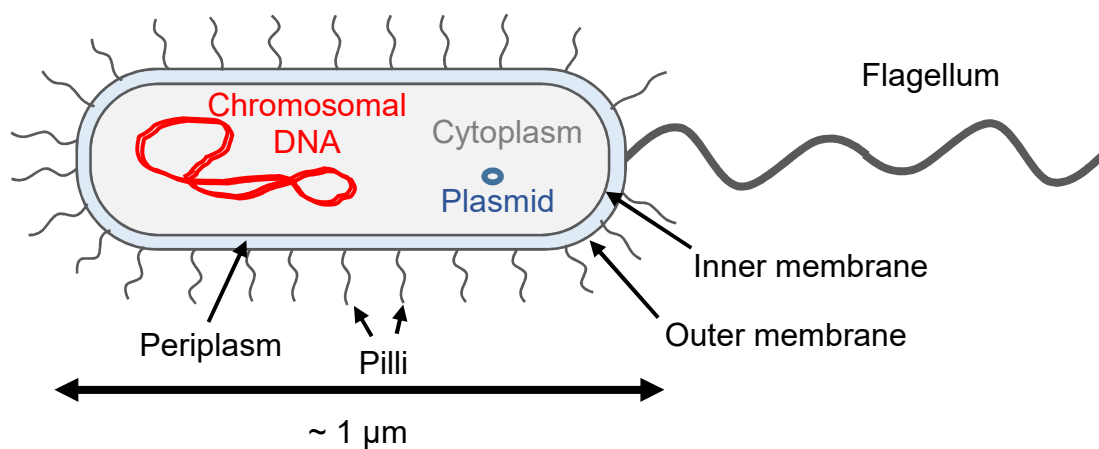


**Figure 1.11** – Basic cellular structure of *E. coli* showing the most important structural features.

Like other Gram-negative bacteria, *E. coli* has two lipid membranes: an outer membrane which encompasses the entire cell volume and an inner membrane which divides the cell into an outer volume, the periplasmic compartment, and the inner cytoplasmic compartment. The cellular structure of Gram-negative cells is closely tied

to the generation of an electromotive force (EMF) which is then employed to drive phosphorylation of ADP to ATP in a way entirely analogous to the mitochondrion.

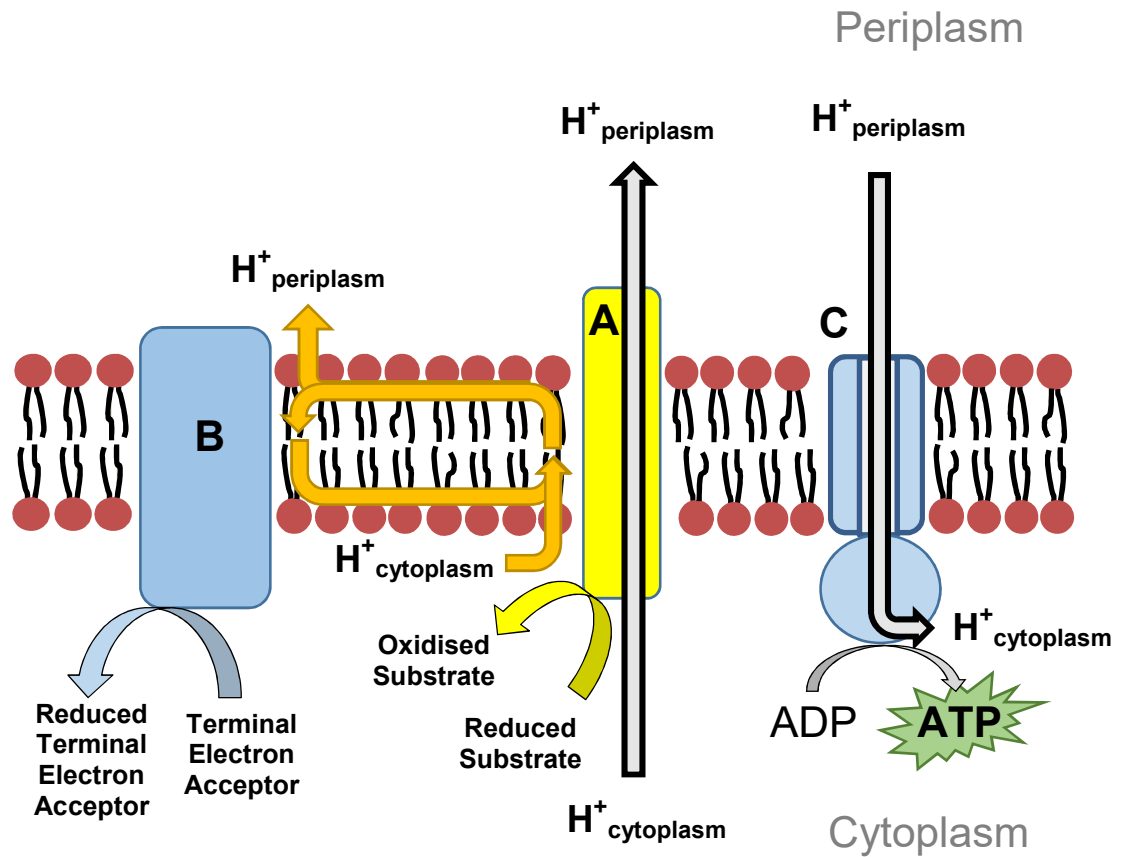


**Figure 1.12** – Scheme of a hypothetical respiratory electron transport chain in a Gram-negative bacterium such as *E. coli*. Unlike the mitochondrial electron transport chain, the electron transport chains found in *E. coli* are typically quite short, often with only a dehydrogenase (A) and a reductase / oxidase (B) present. Normally at least one of the either A or B are proton pumps, although this is not always the case. Electrons are shuttled from A to B via lipid soluble quinones; the site of quinone oxidation / quinol reduction at A and B respectively is normally arranged so that the quinone pool itself also contributes to proton exchange across the membrane. The proton gradient generated by this process is then harnessed by ATP synthases (C) to generate ATP. Some reductases (e.g. respiratory nitrite reductase) are water soluble and not closely associated with the membrane. In this case, a water soluble electron cytochrome is required for electron transfer.

The inner cytoplasmic membrane is peppered with several redox active, multisubunit membrane proteins which form electron transport chains. One of these enzymes (termed a dehydrogenase) catalyses the oxidation of a reduced substrate,

which in the case of *E. coli* is normally either some organic substrate or H<sub>2</sub>. Typically the active site of the dehydrogenase is somewhat removed from the membrane and a number of metal cofactors, typically [Fe<sub>4</sub>S<sub>4</sub>] clusters or heme groups, shuttle the electrons away. Within the membrane, the quinone pool mediates electron transfer from the dehydrogenase to a reductase which catalyses the reduction of a terminal electron acceptor. The energy gained from this electron transfer is used to shuttle protons across the membrane, generating both a concentration and charge gradient as the membrane is impermeable towards protons except through dedicated proton channels. This gradient can then be used to drive exergonic processes occurring at the membrane, including active transport of certain nutrients into the cell and, most importantly, the phosphorylation of ADP to ATP.

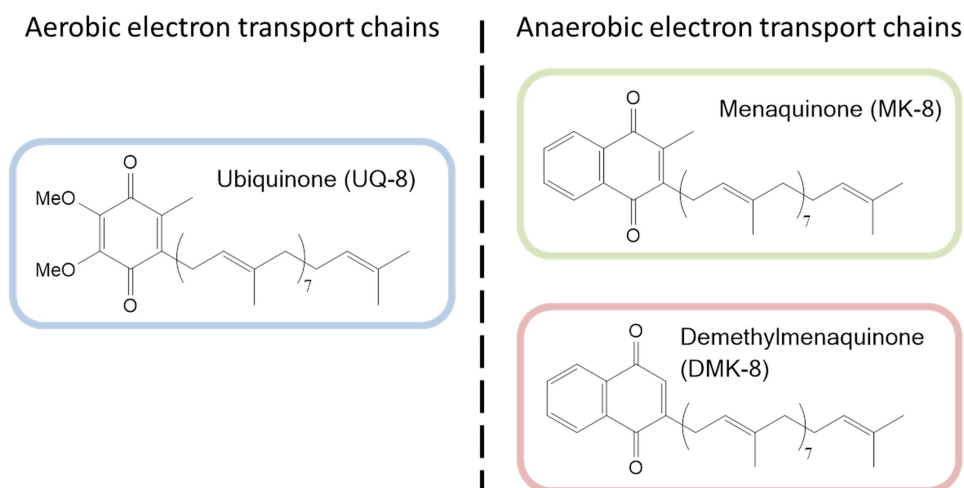


**Figure 1.13** – Structures of the three quinones which mediate electron transfer in *E. coli*. *E. coli* primarily employs (benzo)quinones with eight isoprene subunits.

Proton transfer is mediated both by certain dehydrogenases and some reductases which serve as proton pumps, proton transfer from the quinone / quinol redox reactions and proton consumption or release by the redox processes are localised in such a way that the protons used to form the quinol are taken from the cytoplasm; upon re-oxidation, the same protons are released into the periplasm, further contributing to the formation of a proton gradient and EMF. Finally, the terminal redox reactions themselves can play a role in generating a proton gradient, such as the

reduction of O<sub>2</sub> which is exclusively carried out in the cytoplasm and consumes four protons to generate two moles of H<sub>2</sub>O.

While O<sub>2</sub> is used as the terminal electron acceptor under aerobic conditions, under anaerobic conditions, *E. coli* can express one of several anaerobic electron transport chains which utilise nitrate, nitrite, trimethylamine oxide (TMAO), dimethylsulfoxide (DMSO) or fumarate as the terminal electron acceptor.<sup>41</sup> Expression of these alternative chains is tightly controlled by a number of regulatory proteins, such as FNR ('fumarate and nitrate reduction') and ArcA, which prevent the expression of a number of anaerobic enzymes in the presence of O<sub>2</sub> and stimulate expression in its absence. To aid in the transition from aerobic to anaerobic conditions, *E. coli* constitutively expresses a number of isoenzymes of the anaerobic terminal reductases, meaning that the cells can a small amount of anaerobic respiratory and dehydrogenases under aerobic conditions, albeit at much lower levels than the aerobically repressed enzymes. This means that a small amount of enzyme will always be present to take advantage of changes in environmental conditions, probably aiding the bacterium in rapidly shifting between aerobic and anaerobic environments. While some degree of 'mixing and matching' of the various reductases and dehydrogenases can occur under anaerobic conditions, expression of the various protein components of the electron transport chain is usually regulated in such a way that only a small number of energetically feasible dehydrogenase / reductase pairs are ever co-expressed. The utilised quinone / quinol also varies depending on the electron transport chain; ubiquinone (UQ) is utilised for aerobic electron transport chains and for the NADH / nitrate couple while menaquinone (MK) and demethylmenaquinone (DMK) are employed as the electron transfer agents in other anaerobic pathways. Figure 1.13 summarises some of the key respiratory reductases and dehydrogenases and their membrane orientation.

### A. Terminal Reductases / Oxidases

#### **Periplasmic oriented**

Nitrate	NapABCGH
Nitrite	NrfAB
TMAO	{ TorAC TorZY
DMSO	{ DmsABC YnfFGH
N / S-oxides	MsrPQ

#### **Cytoplasmic oriented**

Oxygen	{ CyoABCD (cytochrome <i>bo</i> <sub>3</sub> ) CydAB (cytochrome <i>bd-I</i> ) CyxAB (cytochrome <i>bd-II</i> )
Nitrate	{ NarXYZ NarGHI
Fumarate	FrdABCD

### B. Respiratory Dehydrogenases

#### **Periplasmic oriented**

Formate	{ FdnGHI FdoGHO
Hydrogen	{ HyaABC HybOABC
Glucose	Gdh
Aldoses	Asd

#### **Cytoplasmic oriented**

NADH	{ NuoA-N Ndh
Lactate	{ Dld LldD
Glycerol-3-phosphate	{ GlpD GlpABC
Succinate	SdhABCD
Pyruvate	PoxB
Fatty acids	YdiR

**Figure 1.14** – Summary of the major respiratory enzymes and their orientation along the inner membrane.

Correct localisation and assembly of respiratory enzymes is essential for their function. Excretion of periplasmic respiratory enzymes from the cytoplasm (where protein synthesis occurs) is usually accomplished by the twin-arginine translocation or transport (Tat) pathway.<sup>42</sup> This pathway relies upon the recognition of a particular short signal peptide of around 20 – 40 residues in length which is appended to the N-terminus of proteins which require exporting. Unlike Sec, the other major protein export system in *E. coli*, Tat exports the proteins in a fully folded state. Tat also incorporates a proofreading mechanism which seems to prevent misfolded proteins being exported to the periplasm.

## 1.4 Aims and Thesis Structure

The increasing interest in gas biology, particularly in relation to the so-called ‘gasotransmitters’ nitric oxide (NO), carbon monoxide (CO) and H<sub>2</sub>S, makes it increasingly important to be able to detect these gases. Many existing analytical techniques have various flaws – they are either unable to detect gases online or *in situ* or they only show limited selectivity or have problems of cross-sensitivity which can be particularly problematic in the complex chemical environments within or surrounding cells. New more selective analytical techniques are therefore required which can detect biologically relevant gases both selectively and *in situ*.

The aim of the work described in this thesis is to develop and employ new and existing gas-phase vibrational spectroscopies for use in monitoring gas metabolism by microorganisms and the release of an important gaseous signalling molecule, CO, by CO releasing molecules (CORMs) which have been employed as CO donors in both *in vitro* and *in vivo* studies. Two complementary approaches to optical gas detection are presented: FTIR spectroscopy and Cavity-Enhanced Raman spectroscopy (CERS).

**Chapter 2** describes the construction and characterisation of a new 8 m path length multiple pass cell for use in FTIR gas-phase spectroscopy. Using the new cell, preliminary measurements of NO reduction to N<sub>2</sub>O by nitrate and nitrite treated *E. coli* are reported along with simultaneous measurements of CO<sub>2</sub> generated by the bacteria.

**Chapter 3** describes the first application of gas-phase FTIR spectroscopy for measuring CO release from a CORM in the presence of cells. In this case, CO release from a UV photoactivated CO releasing molecule (PhotoCORM) which possesses demonstrable antimicrobial activity is monitored by gas-phase FTIR in both sterile media and thick cell suspensions.

**Chapter 4** reports new findings on the CO releasing properties of [Ru(CO)<sub>3</sub>Cl(glycinate)], a CORM widely employed in biological studies, as measured using gas-phase FTIR spectroscopy.

**Chapter 5** presents CERS as a novel technique for monitoring hydrogen metabolism by microorganisms such as *E. coli* and demonstrates how this can be combined with isotopic labelling to simultaneously follow both hydrogen uptake and hydrogen production by the bacteria.



## Chapter 2 – Construction and Characterisation of a Long Path Multiple-Pass White Cell for FTIR Spectroscopy with Applications in Culture Headspace Analysis

### Abstract

In order to detect trace quantities of biologically relevant gases using IR absorption spectroscopy, extended absorption path lengths are required without significantly increasing the sample volume. Multiple-pass cells which use reflective optics to pass the same beam through the same sample volume multiple times can be used to achieve extremely long path lengths in a relatively small volume. In this chapter, the construction and characterisation of a new in-house built two row White cell is described. Using a CW alignment laser, the setup is aligned to give a total of 40 passes corresponding to a folded path length of 8 m. Nitrous oxide (N<sub>2</sub>O), an important intermediate in denitrification, is employed as a calibration gas to allow a more accurate determination of the path length and check the linearity of the technique over a range partial pressures. Backing up samples with air was found to be critical to capturing the true band structure; when only a low pressure of N<sub>2</sub>O was present in the cell, anomalously weak absorption intensities were observed due to a mismatch between the linewidth of individual rovibrational lines at low pressure and the best resolution of the FTIR spectrometer. Using backed up samples and remaining below N<sub>2</sub>O pressures where absorption band saturation was observed, the path length of the White cell was found to be within 1 % of the predicted 8 m path length, which is well within the accuracy of the path length determination method. Using the newly calibrated White cell, N<sub>2</sub>O and CO<sub>2</sub> evolution from anaerobic cultures of *E. coli* treated with either nitrate or nitrite was measured, allowing a direct measurement of both NO reductase activity and general metabolic activity.

## 2.1 Introduction

### 2.1.1 Nitrosative Stress in *Escherichia coli*

Nitrosative stress can be caused by a large number of reactive nitrogen species (RNS) generated either as a by-product of the cell's own metabolism or from external sources. In the case of *E. coli* and related pathogenic organisms such as *Salmonella* species, anaerobic nitrate and nitrite respiration is an important intracellular source of RNS while the mammalian host immune system is known to actively utilise RNS to disrupt and destroy pathogens.<sup>43</sup> The chemical species involved in nitrosative stress are highly reactive, making their detection in the cellular environment challenging. This difficulty in detection and rapid interconversion of different RNS has led to considerable debate over the relative importance of one molecular species over another to the overall cytotoxic effects of RNS. Nitric oxide (NO) is probably the best recognised RNS due to its importance as a low molecular weight signalling molecule in mammalian biology and while it may not be the most cytotoxic of RNS, it lies at the centre of most reactive nitrogen (bio)chemistry, as shown in Figure 2.1.

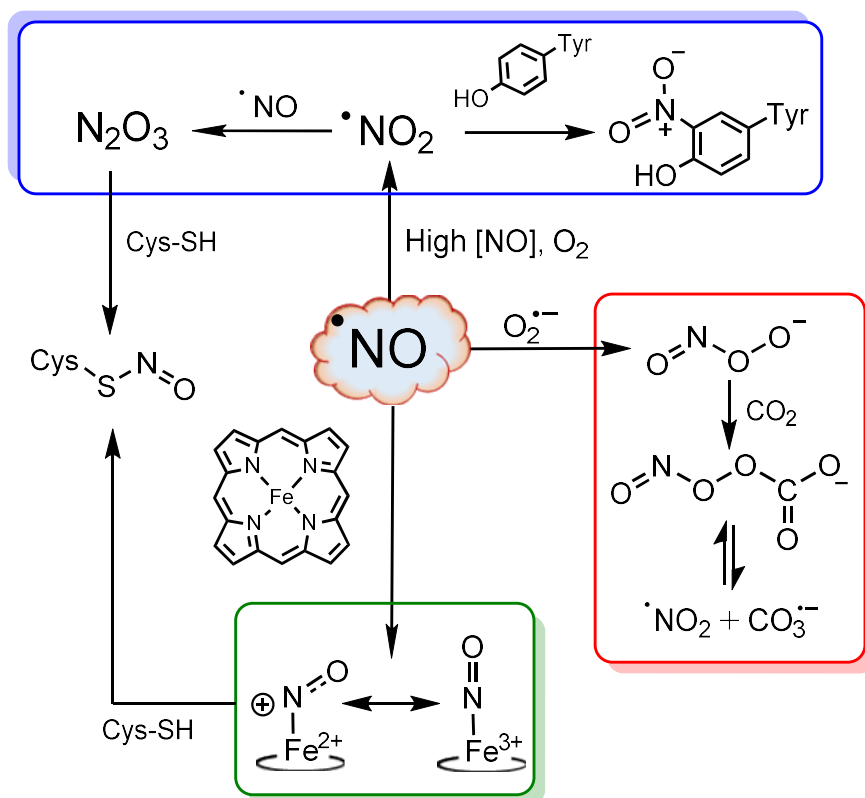


**Figure 2.1** – Some elements of the biological chemistry of NO and related biologically relevant N-oxides and oxanions which contribute to oxidative stress and nitrosative stress.

NO itself can target both heme and non-heme Fe sites and superoxide ( $O_2^{\bullet-}$ ). In aerobic environments, oxidation of NO to nitrogen dioxide ( $^{\bullet}NO_2$ ) becomes increasingly important.  $NO_2$  can nitrate strongly activated aromatic systems such as phenolic tyrosine residues in certain proteins as well as nucleobases. NO can react with the superoxide radical ( $O_2^{\bullet-}$ ) to form peroxynitrite ( $ONOO^-$ ). Peroxynitrite usually rapidly reacts with dissolved  $CO_2$  to form nitrosoperoxycarbonate ( $ONOOCO_2^-$ ) which then decomposes to give  $NO_2$  and carbonate radicals ( $CO_3^{\bullet-}$ ). These radical species can either undergo a recombination reaction or can go on to react with other cellular components, causing significant oxidative and nitrosative damage.

The ability to remove and detoxify RNS is important for survival in the host and both aerobic and anaerobic pathways exist for NO detoxification in *E. coli*.<sup>43</sup> Under aerobic conditions, *E. coli* detoxifies NO primarily through oxidation to nitrate by a flavohaemoglobin known as Hmp.<sup>44-46</sup> NO oxidation requires  $O_2$  and the efficiency of Hmp to function as a NO dioxygenase is therefore reduced under microaerobic conditions, leading to an enhanced sensitivity towards NO stress. Under anaerobic conditions, such as during nitrate respiration, *E. coli* relies upon NO reductases to remove the radical, generating the relatively unreactive nitrous oxide ( $N_2O$ ) as a by-product. Corker *et al.* identified soluble periplasmic cytochrome c nitrite reductase (Nrf) as the primary source of NO when endogenous nitrite was added to anaerobic nitrate respiring cells.<sup>47</sup> On the other hand, a number of other studies have identified nitrate reductase NarG as the primary source of NO under high nitrite / low nitrate conditions. In addition to difficulties in identifying the precise source of NO during nitrate respiration, there has also been considerable difficulty in identifying precisely which enzymes act as NO reductases *in vivo*; flavorubredoxin NorV (along with its reductase NorW) is generally accepted to be a dedicated NO reductase, although Hmp also has NO reductase activity under anaerobic conditions.<sup>48</sup> Vine *et al.* found that while the rate of NO reduction in *E. coli* mutants lacking four putative NO reductases was reduced, the rate of NO removal in a *nirBDC nrfAB norV hmp* mutant was still around 80 % of the parent strain, indicating additional pathways.<sup>49</sup> More recently, Wang *et al.* showed that hybrid cluster protein Hcp acts as a high affinity NO reductase under anaerobic conditions while NorVW is primarily employed for dealing with high concentrations of NO.<sup>50</sup>

Given that NO can bind irreversibly to a number of different biochemically relevant functional groups, it is clearly important to assess to what extent reduction in NO concentration reflects true NO reductase activity and the influence of other mechanisms such as gaseous loss to the headspace and sequestration by irreversible reaction cellular components. For this, good analytical assays are required for measuring both NO and its reduction product, N<sub>2</sub>O. Given the importance of NO as a signalling molecule, numerous fluorescent, electrochemical and spectroscopic assays have been developed for its detection. In *E. coli*, NO selective amperometric sensors and a sensitive biochemical approach based on the β-galactosidase assay have been particularly useful for probing NO biology.<sup>51</sup> In contrast, there is a current lack of powerful analytical techniques for sensitive and selective N<sub>2</sub>O detection. A sensitive gas phase assay based on an automated sampling mass spectrometer has recently been reported for measuring N<sub>2</sub>O above anaerobic cultures but this requires the addition of a correction function to account for gas consumed during the sampling stage. Although N<sub>2</sub>O selective amperometric sensors exist, they have yet to find extensive use, are considerably less sensitive than the equivalent NO amperometric sensors and show some cross-sensitivity with NO and other nitrogen oxides which might be expected to be present in solution.

As a relatively unreactive gas with low solubility, gas phase detection of N<sub>2</sub>O above broth or agar cultures is clearly a viable solution for detection of NO reductase activity. A powerful greenhouse gas, N<sub>2</sub>O is a particularly strong absorber of IR radiation, making it an attractive target for gas-phase IR absorption spectroscopy. There is very little literature on the use of vibrational spectroscopy in the gas-phase to monitor N<sub>2</sub>O generated by microorganisms; Keiner *et al.* demonstrated that a cavity enhanced Raman approach could be used to follow N<sub>2</sub>O and N<sub>2</sub> metabolism the denitrifying organism *Pseudomonas stutzeri*, which when combined with measurements of nitrate and nitrite in solution allowed the researchers to follow the flow of nitrogen through each stage of denitrification.<sup>52</sup> While Raman spectroscopy allows detection of all molecular gases, including both N<sub>2</sub>O and N<sub>2</sub>, the weakness of Raman scattering limits this approach to systems where these gases represent major metabolites (i.e. in true denitrifying organisms). For studying systems where N<sub>2</sub>O is a minor product, such as in enteric bacteria, direct IR absorption spectroscopy using a commercial FTIR spectrometer represents a reasonably sensitive and accessible system for measuring total NO reductase activity.

### 2.1.2 Achieving High Sensitivity with FTIR Spectroscopy

Most commercial FTIR spectrometers are designed specifically for condensed phase measurements such as surface reflectance measurements, transmission through thin films, absorption by solid suspensions and solution phase measurements. For gas phase measurements, most instruments are only supplied with simple single pass cells with IR transmissive windows which, due to the short absorption path length, only allows detection of major gaseous metabolite with large absorption cross-sections (in particular  $\text{CO}_2$ ). While  $\text{N}_2\text{O}$  is in fact a somewhat stronger absorber than  $\text{CO}_2$ , a much lower quantity of the gas will accumulate in a sealed culture as  $\text{NO}$  is only generated by nitrite respiring cells as a comparatively minor by-product.

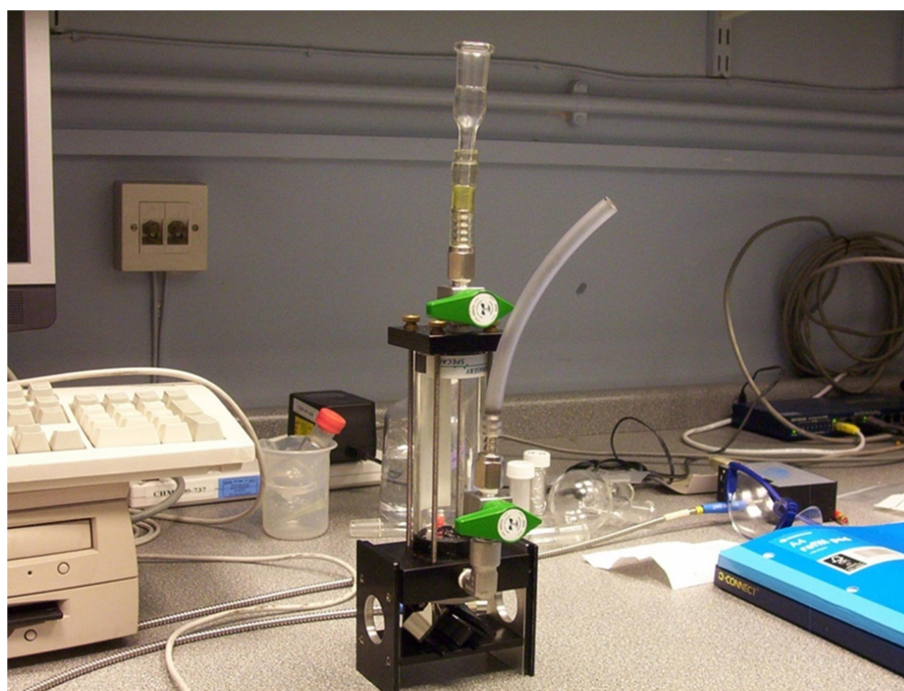
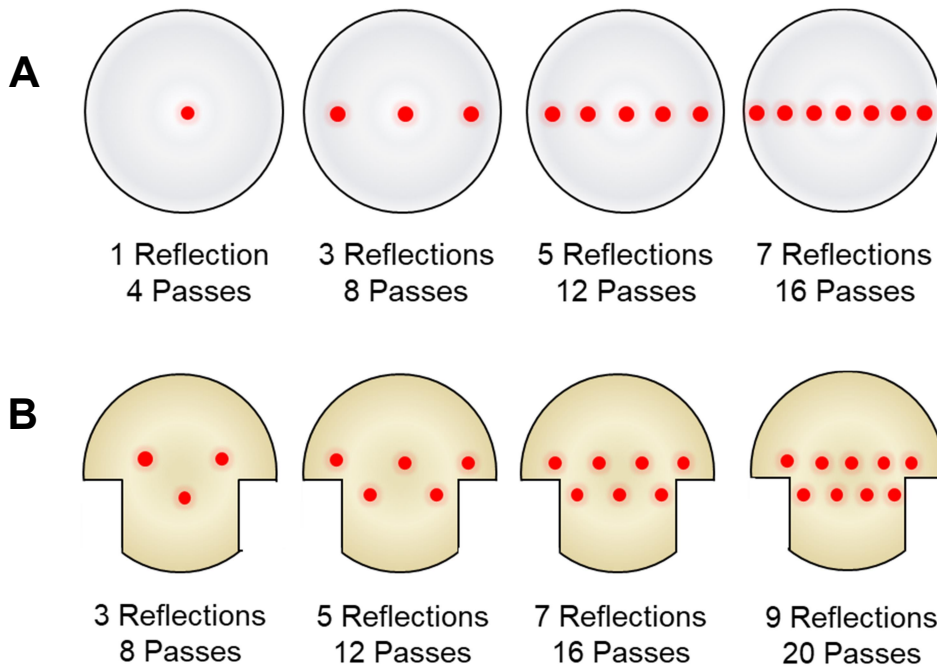


**Figure 2.2** –Specac 2.4 m fixed path length White cell. The three concave mirrors are housed within the glass tube.

As mentioned in section 1.2.2, long absorption path lengths are required for sensitive absorption spectroscopy. Both the limited dimensions of the instrument sample compartment and the limited amount of  $\text{N}_2\text{O}$  available from metabolism mean that simply using an extremely long single pass system is unfeasible due to dimensional constraints and dilution. The multipass White cell design is perfectly suited to such measurements, allowing increased sensitivity without vastly increasing

the headspace volume. A commercially available cell with a folded absorption path length of 2.4 m is shown in Figure 2.2.

The number of passes supported by a White cell is dependent upon the angle of the two upper mirrors with respect to each other and the incoming beam. The total number of passes can only increase in multiples of four; each cycle of four passes consists of the beam passing from the field mirror (or from the input aperture for the first pass) to one of the two upper mirrors before being reflected back to the field mirror. This beam is then reflected to the second of the two angled mirrors before passing back to the field mirror (or passing through the exit aperture in the case of the final pass).



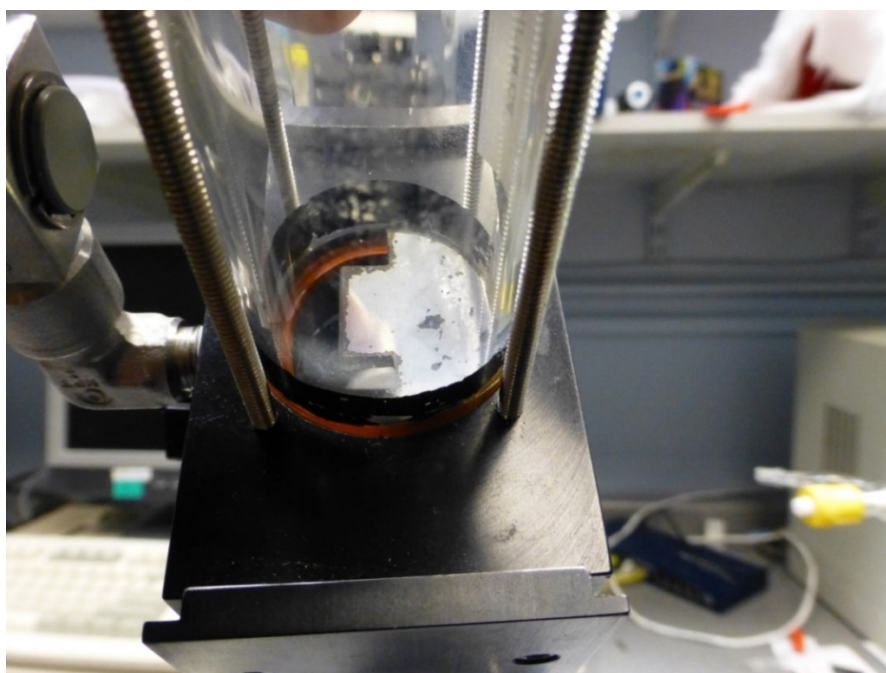
**Figure 2.3** – Number and arrangement of reflections on the field mirrors of single row (A) and two row (B) White cells. In both cases the total number of passes is equal to the  $2(N + 1)$  where  $N$  is the number of spots visible on the field mirror. The two row design uses the mirror area more efficiently

Figure 2.3 visualises the reflections formed on the field mirror by the reflected beam as the number of passes increases. Note that as the number of passes increases, the outermost spots move further to the edges of the field mirror; the maximum number of passes is usually limited by the total number of discrete images which can be fitted along the field mirror diameter. A slightly more complex design employs a mushroom shaped mirror and relies upon the incoming beam entering the cavity

slightly away from the field mirror to generate two rows of images. This design uses the mirror surface more efficiently, allowing a larger number of passes to be accommodated without increasing the mirror diameter. The number of passes can be determined by visualising these reflections using a low power visible CW laser source with spatial high coherence such as a Helium-Neon (HeNe) laser; the total number of passes is equal to  $2(N+1)$  where  $N$  is the number of reflections on the field mirror.

### 2.1.3 Aims

To measure trace gases generated by microorganism such as N<sub>2</sub>O, long absorption path lengths are required. Unfortunately, due to previous work on hydrogen sulfide (H<sub>2</sub>S) metabolism, the silver mirrors of the Hippler group's commercial multipass White cell had become severely corroded, significantly reducing light throughput (see Figure 2.4). This chapter describes the assembly and characterisation of a new White cell was designed around readily available optical parts (sourced from Thorlabs Inc.). In addition, as a demonstration of the utility of FTIR gas phase spectroscopy for online detection of gases generated by microorganisms, preliminary measurements of biological NO reduction by *E. coli* using the new White cell is also described.



**Figure 2.4** – Severe corrosion of the silver field mirror of the commercial 2.4 m White cell due to reaction with H<sub>2</sub>S and other volatile sulfur species.

## 2.2 Experimental

### 2.2.1 White Cell Components and Assembly

The White cell was constructed using commercially available components. Two protected gold coated mirrors (Thorlabs,  $f = 100$  mm, 2 inch diameter) were treated with a protective overcoat to protect the delicate mirror surface from scratches during the cutting process. Two wedges were cut from one mirror to give the T-shaped field mirror required for a two row White cell while the second mirror was cut along the diameter to give the two refocusing mirrors. Once cut, the protective coating was removed with successive acetone and ethanol washes before the mirrors were left to air dry.

After drying, the mirrors were placed inside a purpose-built glass tube ( $l = 250$  mm,  $d = 55$  mm) equipped with two Teflon taps for controlled introduction of gases and to allow continuous-flow measurements. The mirrors were carefully aligned inside the tube using a 632.8 nm HeNe laser (Milles Griot 05 STP 903 stabilised HeNe, 1 mW output) and the angle of the two refocusing mirrors were adjusted in order to obtain the optimum number of passes while avoiding clipping the beam on the entrance or exit apertures (Figure 2.5). Once the position of the mirrors had been finalised, they were epoxied in place and the guiding rods and mounts used to position the mirrors were removed. The tube was sealed by epoxying an IR transparent window (Crystran Ltd.,  $\text{CaF}_2$ ,  $d = 55$  mm, 3 mm thickness) adjacent to the field mirror to allow the IR beam to pass into and out of the cell while a 1 mm thick glass window was epoxied on the opposite side of the tube. The glass cell was then mounted in a 60 mm optical cage system (Thorlabs) which had been cut to accept the glass tube and equipped with two plane diverting mirrors (Thorlabs, protected gold, 24.5 mm). After assembly and sealing, the cell was placed under vacuum in order to check for leaks in the system. After leaks had been identified and sealed with further application of epoxy, the cell was pumped down continuously until a base pressure of approximately  $1 \times 10^{-3}$  mbar could be maintained using an oil diffusion pump (Edwards Speedivac).

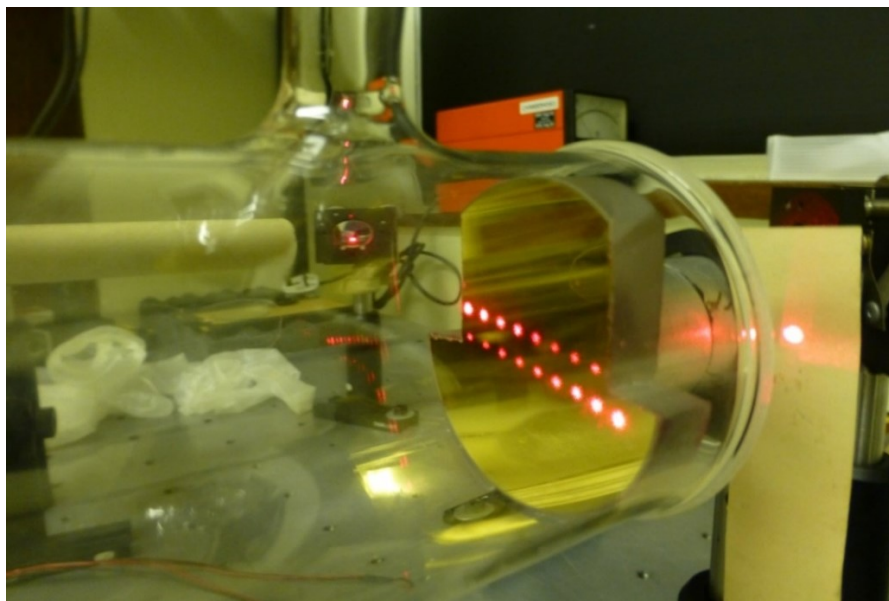


**Figure 2.5** – T-shaped field mirror during the initial alignment inside the glass vessel. The laser beam enters from the left hand slit and is reflected between the field mirror and the pair of mirrors located at the top of the tube. This arrangement leads to the two rows of images formed on the surface of the field mirror. The exit beam is visualised on the piece of paper on the right of the image to check for beam clipping.

## 2.2.2 Path Length Determination

To determine the White cell path length, known pressures of  $\text{N}_2\text{O}$  were introduced into the cell using a gas handling Schlenk line (Figure 2.6). The line is equipped with Teflon Youngs-style greaseless taps, a Pirani pressure gauge for low pressure measurements ( $1 \times 10^3 - 5 \times 10^4$  mbar range) and a 100 Torr range diaphragm gauge (Leybold Vacuum GmbH CTR 90) for accurately measuring higher pressures. In order to thoroughly evacuate the system, the line is equipped with an oil diffusion pump (Edwards Speedivac) backed up by a rotary vane roughing pump (Edwards RV5). Working together, the system can be routinely operated down to a baseline pressure of less than  $1 \times 10^{-3}$  mbar. A liquid nitrogen cooled cryogenic trap is used to prevent condensable gases reaching the pumps. The vacuum / gas manifold is equipped with B14/23 Quickfit<sup>®</sup> connectors which allow a range of custom flasks, ampules and the White cell itself to be quickly connected to the rest the system for controlled addition, purification and dilution of gases and evacuation and leak testing of gas tight vessels.

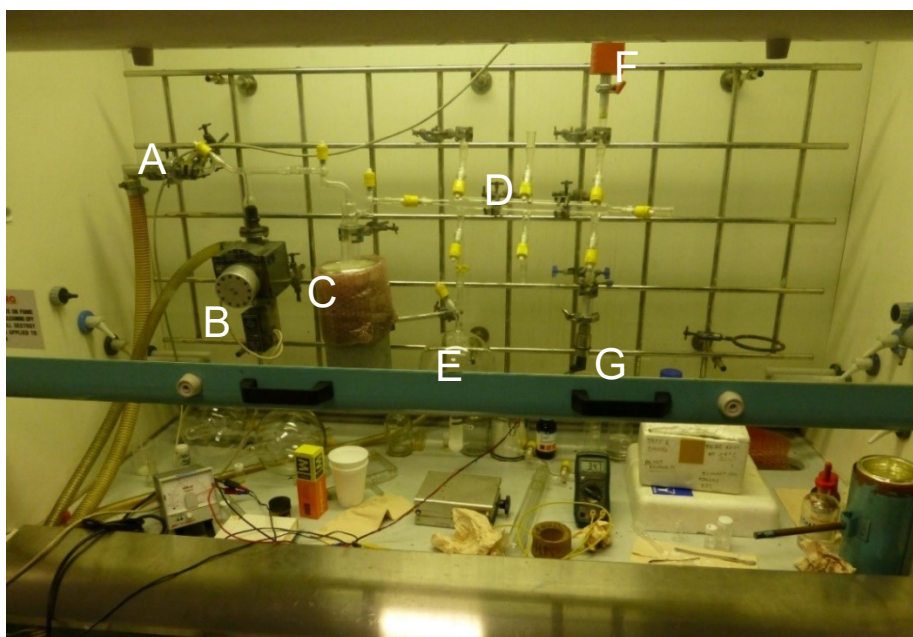


**Figure 2.6** – Gas handling line used to purify gases and introduce defined pressures into the White cell and single pass cells for path length calibration. From left to right: roughing bypass tap (A), oil diffusion pump (B), liquid nitrogen trap (C), vacuum manifold (D) and sample bulb (E). A Pirani gauge (F) was used to monitor low pressures while a diaphragm gauge (G) was employed to accurately measure filling pressures.

$\text{N}_2\text{O}$  (99.998 %, Fluka) was flushed through an evacuated cold trap cooled with liquid  $\text{N}_2$ . After sufficient  $\text{N}_2\text{O}$  has been condensed, the sample was transferred by cryogenic distillation into a previously evacuated 2 L capacity glass bulb. The bulb is equipped with a Youngs tap, which allows the bulb to be isolated from the rest of the system, and a cold finger which is used for cryogenic trapping and purification of gases (Figure 2.7). Previous experience in the group has shown that such bulbs can maintain the integrity of low pressure gaseous samples for several weeks. Non-condensable gases ( $\text{N}_2$  and  $\text{O}_2$ ) were removed by repeated freeze-pump-thaw cycles, using liquid  $\text{N}_2$  to condense  $\text{N}_2\text{O}$  into the cold finger of the glass bulb. After the final cycle, the bulb was isolated from the rest of the line and the purified  $\text{N}_2\text{O}$  was allowed to expand inside the bulb.

For each calibration point, a controlled pressure of purified  $\text{N}_2\text{O}$  (0.1 – 4 mbar), was introduced into the evacuated White cell. Samples were backed up to atmospheric pressure with air before single beam FTIR spectra were recorded (Matteson Research Series FTIR, 512 scans,  $0.4\text{ cm}^{-1}$  resolution, MCT detector). A spectrum of the White

cell filled with lab air recorded before evacuating and filling the cell was used as a background for all measurements on that particular day.



**Figure 2.7** – Sample bulb equipped with a cold finger to allow freeze-pump-thaw purification and cryogenic transfer of gases. A makeshift air-insulated Dewar formed from two polystyrene cups is used to condense  $\text{N}_2\text{O}$  into the cold finger while the line is opened to vacuum to remove any non-condensable gases.

Absorbance spectra, defined as  $\ln(I_{\text{Background}}/I_{\text{Sample}})$ , were compared with reference spectra generated using absorption cross-sections from the HITRAN 2012 database for  $\text{N}_2\text{O}$  ( $^{14}\text{N}^{14}\text{N}^{16}\text{O}$  isotopomer, > 99 % natural abundance) assuming 1 bar  $\text{N}_2$  pressure broadening and using rotational state populations calculated for 298 K. In house software was used to extract the data, calculate the correct rotational state populations (which influence the relative intensities of individual rotational lines) and convolute the reference data with a Lorentzian lineshape to simulate the effect of 1 bar  $\text{N}_2$  pressure broadening giving an approximate linewidth of  $0.1 \text{ cm}^{-1}$ . Experimental absorption band integrals for the  $\nu_1 + 2\nu_2$  and  $2\nu_2$  bands were compared with band integrals from a simulated spectrum based on the HITRAN 2012 cross-sections and assuming an 8 m path length in order to determine the true path length of the White cell.<sup>1</sup> To test the validity of the approach, a single pass absorption cell with a well-defined path length ( $\text{CaF}_2$  windows,  $l = 14.5 \text{ cm}$ ) was filled with higher pressures of  $\text{N}_2\text{O}$  to compensate for the reduced path length. These experimental spectra were then

compared with spectra simulated using the same HITRAN 2012 cross-sections but assuming a 14.5 cm path length.<sup>1</sup> Absorption band integrals of the experimental and simulated spectra showed good agreement over the range of pressures tested for the single pass cell.

### 2.2.3 Measuring NO Reduction by Nitrate and Nitrite treated cultures

For each experiment, a single colony of *E. coli* K-12 MG1655, isolated from antibiotic free LB-agar (plates previously prepared from 50:50 LB:glycerol stock, was used to inoculate 50 mL of sterile LB growth medium and placed in an orbital incubator (200 rpm, 37 °C, 16 hours). After overnight growth, 1 mL of the overnight culture was transferred to a sterile five neck custom B19/26 Quickfit<sup>®</sup> adaptor flask filled equipped with a 2 cm magnetic stirrer and charged with 49 mL of sterile Evans medium (prepared according to Evans *et al.* with additional modifications described by Rolfe *et al.*, replacing citrate with nitriloacetic acid as the chelator and with addition of sodium selenite).<sup>53</sup> This was supplemented with 20 mM glucose (filtered sterilised through 0.22 µM Millipore sterile filter).

Figure 2.8 shows the experimental setup used for online FTIR measurements of NO reduction by *E. coli*. After transfer to the FTIR apparatus, the flask was connected to the White cell via 3 mm internal diameter polyethylene tubing and a custom Quickfit<sup>®</sup> B19/26 stopper with two glass capillary feedthroughs to allow gas to be circulated through the system. The flask was placed in a water bath and held at 37 °C using a stirrer hotplate while the headspace was circulated through the White cell and back into the flask using a peristaltic pump providing a nominal flow rate of 7 L h<sup>-1</sup>. Continually stirring was employed to maintain good gas transfer between the solution and headspace. The White cell was wrapped in thermal resistive tape to maintain an internal temperature of 40 – 45 °C in order to prevent condensation on the White cell optics. After connecting the flask, the system was rapidly evacuated and flushed with N<sub>2</sub> before a FTIR spectrum of the headspace was recorded. This was used as a background for all subsequent single spectra recorded during the biological measurement. One of either potassium nitrate (10 mM final concentration) or potassium nitrite (2.5 mM final concentration) was injected into vessel through a suba

seal. Headspace FTIR spectra ( $0.4\text{ cm}^{-1}$ ,  $400 - 7000\text{ cm}^{-1}$ ) were recorded at 15 minute intervals to follow the evolution of  $\text{N}_2\text{O}$  and other IR active gases for 16 hours.

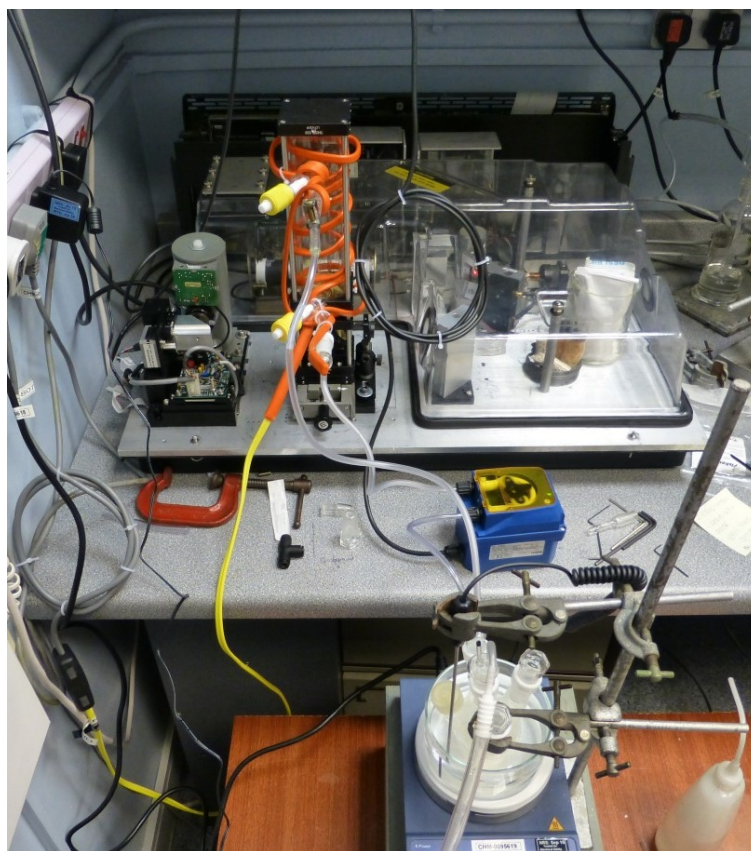


**Figure 2.8** – Experimental setup for online FTIR headspace monitoring of NO reduction /  $\text{N}_2\text{O}$  evolution by nitrate / nitrite respiring *E. coli* cultures. The culture headspace is continually circulated through the system by means of a peristaltic pump

To quantify  $\text{N}_2\text{O}$  and  $\text{CO}_2$ , absorption spectra were generated using each experimental spectrum and the background spectrum recorded at the start of each measurement series.  $\text{N}_2\text{O}$  partial pressure was determined by integrating the  $2\nu_1$  combination band ( $2505 - 2613\text{ cm}^{-1}$ ) and comparing the integral with a simulated 1 mbar  $\text{N}_2\text{O}$  absorption spectrum generated using absorption cross-sections taken from HITRAN 2012.<sup>1</sup>  $\text{CO}_2$  partial pressure was determined by integrating a high frequency combination band ( $4905 - 5033\text{ cm}^{-1}$ ) and comparing this spectrum with a simulated 1 mbar  $^{12}\text{CO}_2$  generated using HITRAN 2012 cross-sections for this isotopomer.<sup>1</sup> For both simulated spectra, in house software was used to simulate 1 bar pressure broadening so that the individual rotational lines better represent the lines structure of experimental spectra.

## 2.3 Results & Discussion

### 2.3.1 White Cell Construction & Visible Alignment

In order to avoid the problems with mirror corrosion observed with the commercial White cell, gold was chosen as the optical material for the mirrors as it shows good chemical resistance towards  $H_2S$  and thiols. Although gold has comparatively poor reflectivity in the visible region due to surface plasmon resonance bands, its reflectivity in the MIR range is excellent, around 98 % over the majority of the fundamental region. Apart from reflection losses, the total number of passes is ultimately limited by the number of images which can be fit along the diameter of the field mirror, so it was decided that two inch (50.4 mm) gold mirrors should be employed to allow for an increase in total number of passes and therefore sensitivity over the original White cell. Two inch mirrors also provide more rear surface for stable mounting during the delicate alignment process. The entire cell was built within a 60 mm optical cage system to provide maximum rigidity (Figure 2.9).

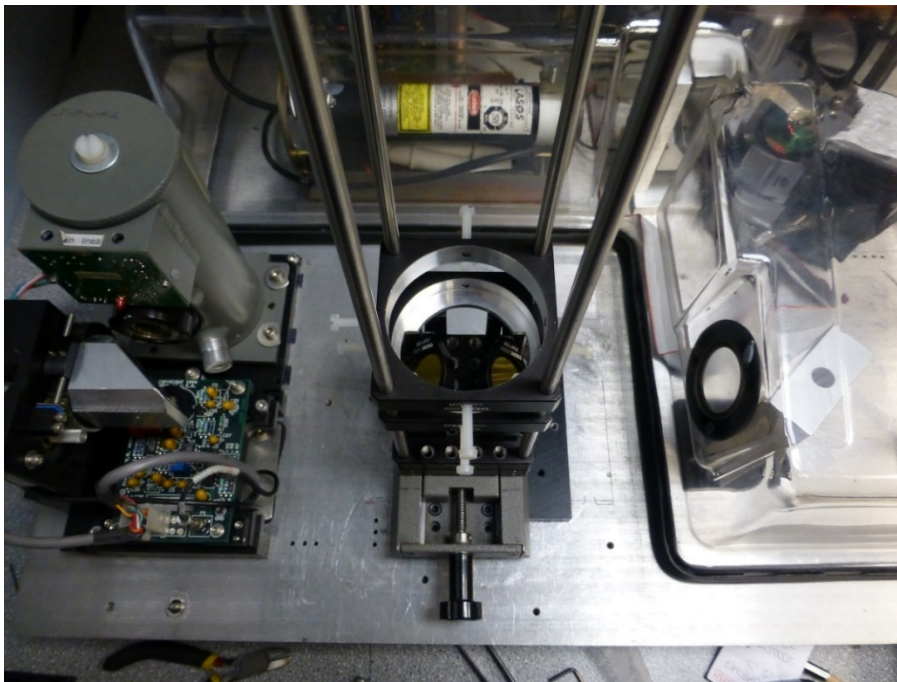


**Figure 2.9** – Initial setup of the mounting plates before installation of the main body of the White cell showing the steering mirrors, supporting rods and plates. The lower base provides a rigid and stable mounting platform for the White cell. A single axis translation stage provides a greater degree of flexibility during alignment. Two 1 inch steering mirrors are used to inject the IR beam into the cell and divert the exiting beam to the detector.

CaF<sub>2</sub> was chosen for the IR window as it represents a good compromise between moisture resistance and good transmission over most of the IR and visible region. While the transmission of CaF<sub>2</sub> cuts off sharply at wavenumbers below 1000 cm<sup>-1</sup>, meaning that low wavenumber vibrational modes are lost, most small molecules have their fundamental absorption bands at comparatively high wavenumbers, with stretching modes typically above 1500 cm<sup>-1</sup>. Salt optics such as NaCl and KBr cut off at much lower wavenumbers but they are also extremely hygroscopic making them less than ideal for *in situ* headspace measurements of microbial cultures where the water vapour concentration essentially remains at saturation. CaF<sub>2</sub>, by contrast, is essentially completely insoluble in water making it ideal for situations where excess water vapour is unavoidable.

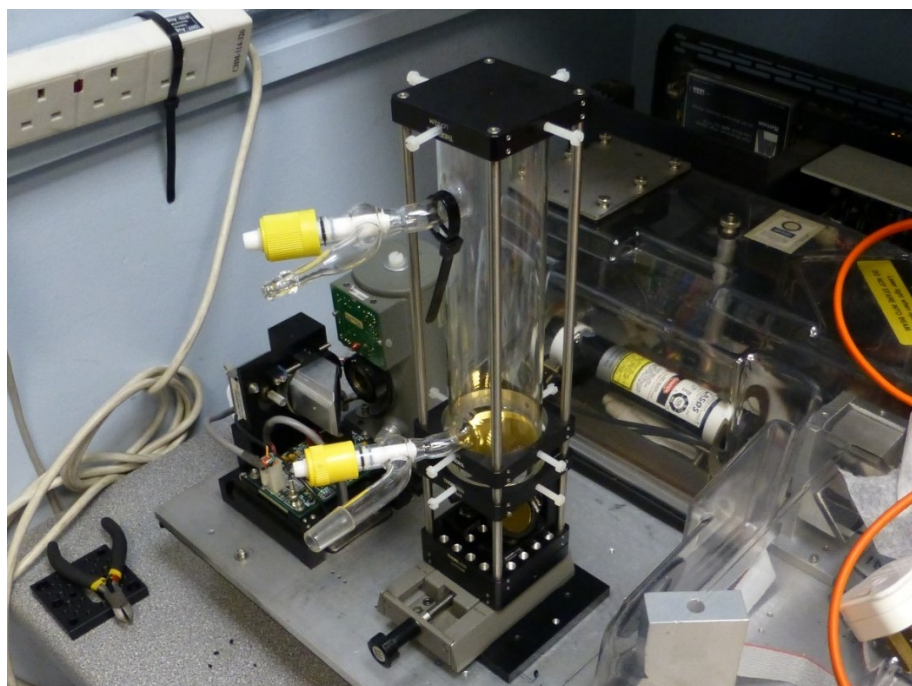


**Figure 2.10** – Completed White cell mounted inside FTIR spectrometer. The White cell can be removed for evacuation or filling with gases using the B14/23 Quickfit<sup>®</sup> adaptor arm on the lower segment. The flask is equipped with a second arm with a tubing adaptor to allow the system to be purged or for flow measurements. Teflon Youngs taps provide gas tight, grease free seals to allow the cell to be isolated.

By placing a red 636 nm HeNe alignment laser collinear with the IR beam, the number of passes in the aligned White cell could be determined by simply counting the total number of spots on the field mirror (Figure 2.10). The total number of passes

is equal to twice the number of spots plus an additional 2 passes to account for the beam passing through the exit slit of the field mirror. In Figure 2.11, there are 19 spots, corresponding to 40 passes through the cell volume. As the mirror separation is 20 cm, this gives a total folded path length of approximately 8 m.

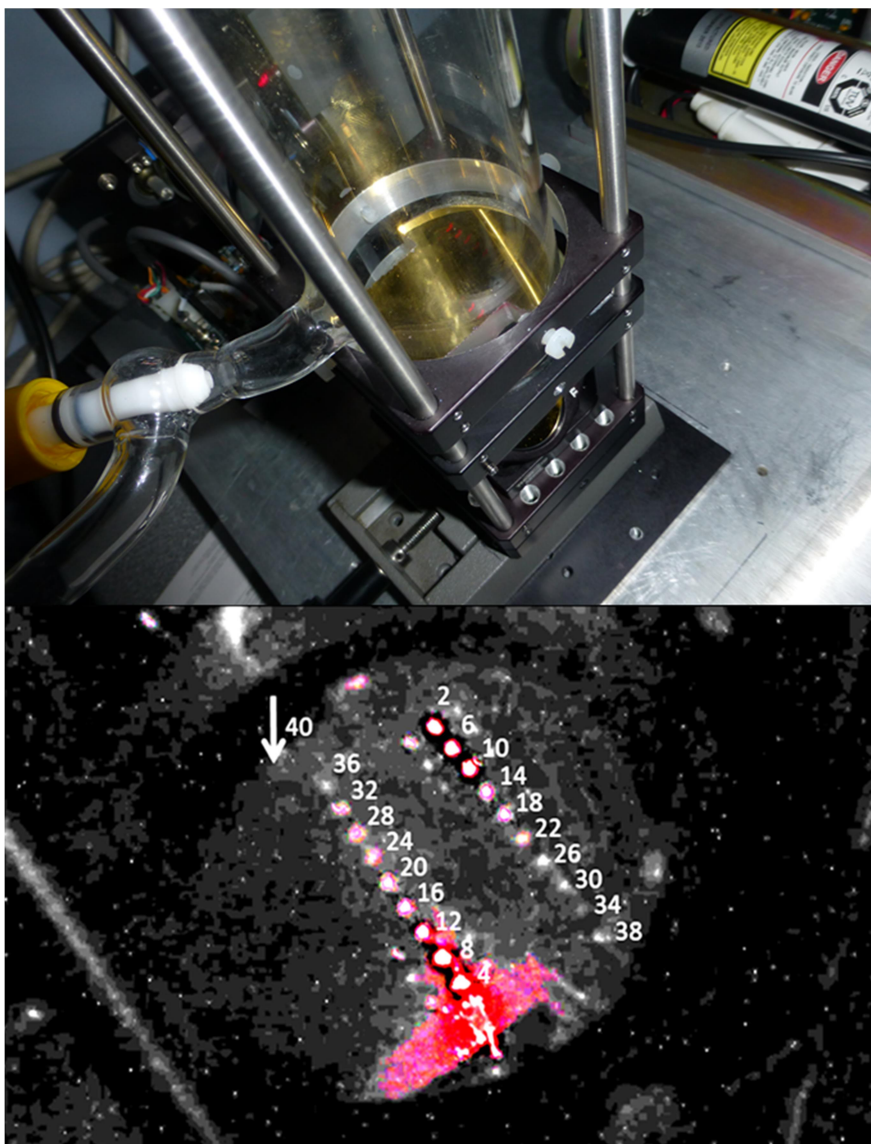


**Figure 2.11** – Top: Field mirror of the aligned White cell mounted within the FTIR measurement compartment with a HeNe laser collinear with the IR beam of the spectrometer. While spots were not too difficult to visualise by eye, the spots proved difficult to capture using a commercial camera. Bottom: Overexposed image of the same configuration from the same angle. The later spots appear much dimmer due to absorption from repeated reflection from the gold mirrors which have poor performance in the visible region. Each spot corresponds to two passes through the cell volume. After 40 passes, the laser leaves through the exit slit cut in the field mirror (top left cut out).

### 2.3.2 Path Length Calibration with N<sub>2</sub>O

While the total number of passes is easily determined simply by visualising the beam path with a visible laser, the actual path length is somewhat harder to directly determine. To a good first approximation, the path length is equal to the mirror separation (or base path length) multiplied by the number of passes. However, this method fails to take account of the fact that the beam is always somewhat angled with respect to the optical axis of the cell so that it takes a slightly longer path. The beam also travels through an additional 2 - 3 cm of sample volume at either side of the field mirror as the beam enters and exits the cell. In addition, although a visible alignment laser is useful for accurate positioning of the mirrors, the IR beam diameter is significantly larger than that of the HeNe alignment laser when entering the White cell, meaning that the IR ‘spots’ formed on the field mirror are typically quite large. It is possible that some light which has travelled a shorter number of passes might potentially leak through the exit aperture of the field mirror (e.g. from spot 36 in Figure 2.11).

Given these difficulties, clearly an accurate determination of the cell path length was required before the system could be used for any analytical applications. By using a simple Schlenk-style single manifold gas handling system equipped with accurate pressure gauges and a cryogenic trap, it was possible to purify and introduce known pressures of IR-active gases into the White cell. Since N<sub>2</sub>O represents a biologically relevant and particularly promising target for IR detection, it was chosen as the calibration gas for determining the White cell path length. N<sub>2</sub>O has a number of attractive properties for use for path length calibration; it is easily condensable using liquid nitrogen (b.p. – 88 °C, m.p. – 91 °C), relatively unreactive and has a number of well characterised absorption bands of varying strength within the MIR region which are well separated from water and CO<sub>2</sub> bands.<sup>54</sup> Figure 2.12 shows the strongest IR absorption bands of N<sub>2</sub>O above 1000 cm<sup>-1</sup> (the low wavenumber cut-off for CaF<sub>2</sub>). Like other linear molecules, N<sub>2</sub>O has well defined rovibrational band structure consisting of evenly spaced rotational lines. Unlike CO<sub>2</sub>, N<sub>2</sub>O is not centrosymmetric meaning that all of the fundamental transitions are IR active. The three fundamental bands have vibrational frequencies of 1284.91 cm<sup>-1</sup> ( $\nu_1$ , asymmetric stretching), 588.77 cm<sup>-1</sup> ( $\nu_2$ , bending) and 2223.76 cm<sup>-1</sup> ( $\nu_3$ , symmetric stretching).<sup>54</sup> Unfortunately the bending transition cannot be observed when using CaF<sub>2</sub> optics;

most materials with transmission to longer wavelengths are hygroscopic and therefore completely unsuitable for work in high humidity environments.

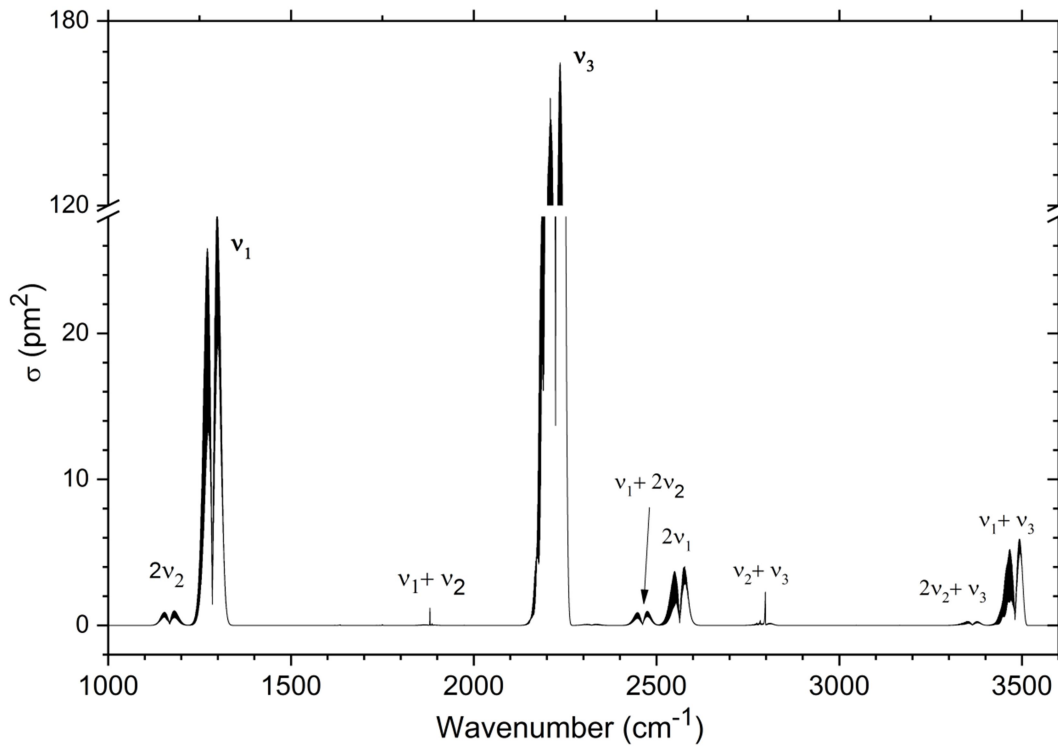


**Figure 2.12** – Simulated absorption spectrum of the major isotopomer of  $\text{N}_2\text{O}$  ( $^{15}\text{N}^{15}\text{N}^{16}\text{O}$ ) showing molecular absorption cross-section as a function of wavenumber. The data is convoluted with Lorentzian broadening to simulate the spectroscopic lineshape at 1 bar  $\text{N}_2$  pressure broadening. The  $\nu_1$  (asymmetric stretching) and  $\nu_3$  (symmetric stretching) are the strongest bands within the  $\text{CaF}_2$  transmission window, although the weaker  $2\nu_1$  overtone band and  $\nu_1 + 2\nu_2$  and  $\nu_2 + \nu_3$  combination bands proved more useful for calibration purposes as the stronger fundamental bands were found to saturate even at low pressures.

In addition to the fundamental bands, a number of weaker overtone bands (occurring from excitation to higher vibrational states) and combination bands (simultaneous excitation of two or more vibrational modes) can be observed. The two bands situated between 2400 and 2650  $\text{cm}^{-1}$ ,  $\nu_1 + 2\nu_2$  (centred at 2461.5  $\text{cm}^{-1}$ ) and  $2\nu_1$  (centred at 2563.5  $\text{cm}^{-1}$ ), are particularly well separated from most other gaseous absorption bands, in particular water vapour lines which heavily contaminate other regions.

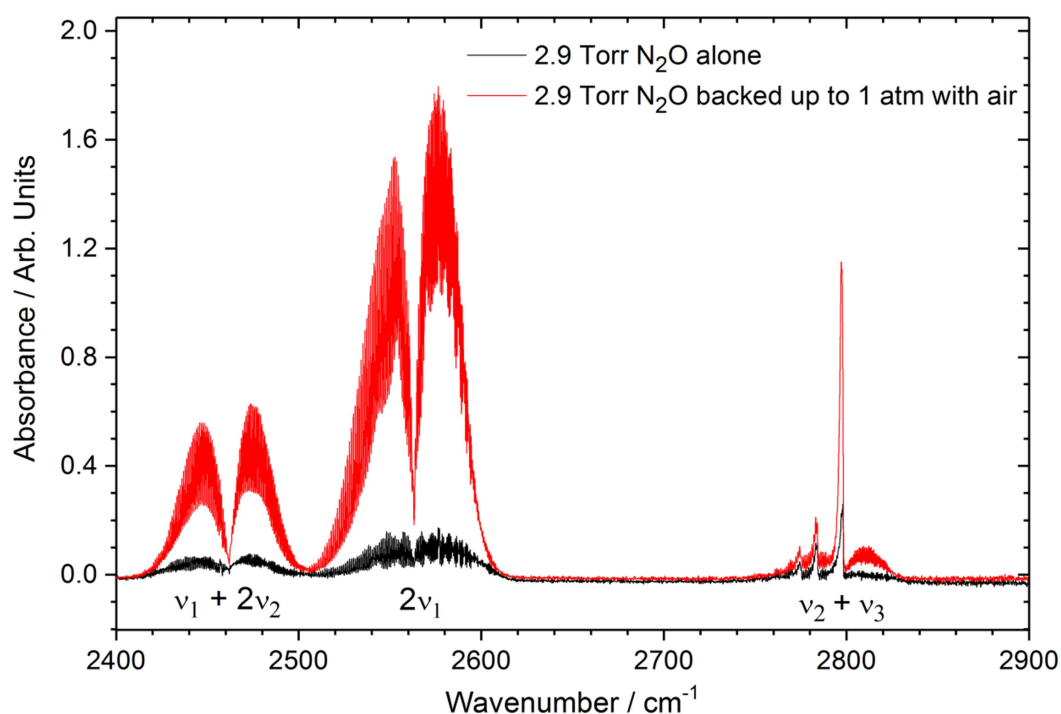


**Figure 2.13** – Drastic impact on the spectrum of N<sub>2</sub>O upon increasing the total pressure within the system. Black spectrum shows 2.9 Torr N<sub>2</sub>O recorded using the White cell, MCT detector and 0.4 cm<sup>-1</sup> resolution. The red spectrum shows the same sample after backing up the sample with air.

After recording preliminary spectra with N<sub>2</sub>O, it rapidly became clear that the stronger fundamental bands were simply too strong to use, with severe saturation effects noticeable for even very low pressures. To avoid introducing additional dilution steps which would inevitably reduce the accuracy of the calibration, the much weaker  $\nu_1 + 2\nu_2$  and  $2\nu_1$  bands were selected. These bands are in a region which is essentially free of interfering CO<sub>2</sub> and water vapour absorption lines which is an additional advantage over the stronger fundamental bands. Even with these weaker bands, saturation effects were noticeable at N<sub>2</sub>O partial pressures above 2 Torr (2.67 mbar), so the path length calibration was carried out using N<sub>2</sub>O filling pressures between 0.2 and 1.0 Torr (0.27 and 1.33 mbar).

Preliminary measurements with N<sub>2</sub>O at low pressure within the White cell showed noticeable discrepancies with the experimental and predicted band shape and strength (black trace Figure 2.13). As a result, the integrated band intensities corresponded to a path length much shorter than expected based on the visible alignment. While band distortion can be observed when absorption bands become highly saturated (i.e.

$\ln(I_0/I) \gg 1$ ), the peak absorbance of these bands was below 0.2 for the highest pressure tested. Initially it was suspected that the anomalous band intensities might be caused by the White cell itself or the liquid N<sub>2</sub> cooled mercury cadmium telluride (MCT) photovoltaic detector which had only just been reinstalled into the apparatus. In order to test this, a single pass absorption cell with a well-defined path length (14.5 cm) was filled with a defined pressure of purified N<sub>2</sub>O and IR spectrum recording using a room temperature pyroelectric deuterated triglycine sulfate (DTGS) detector. When the sample cell was filled with N<sub>2</sub>O alone, a similar but less noticeable discrepancy in peak intensity was observed (Figure 2.14, black trace). When the same samples were backed up with to atmospheric pressure by quickly opening up the cell to air, the strength of absorption bands increased significantly (red trace in Figure 2.14).

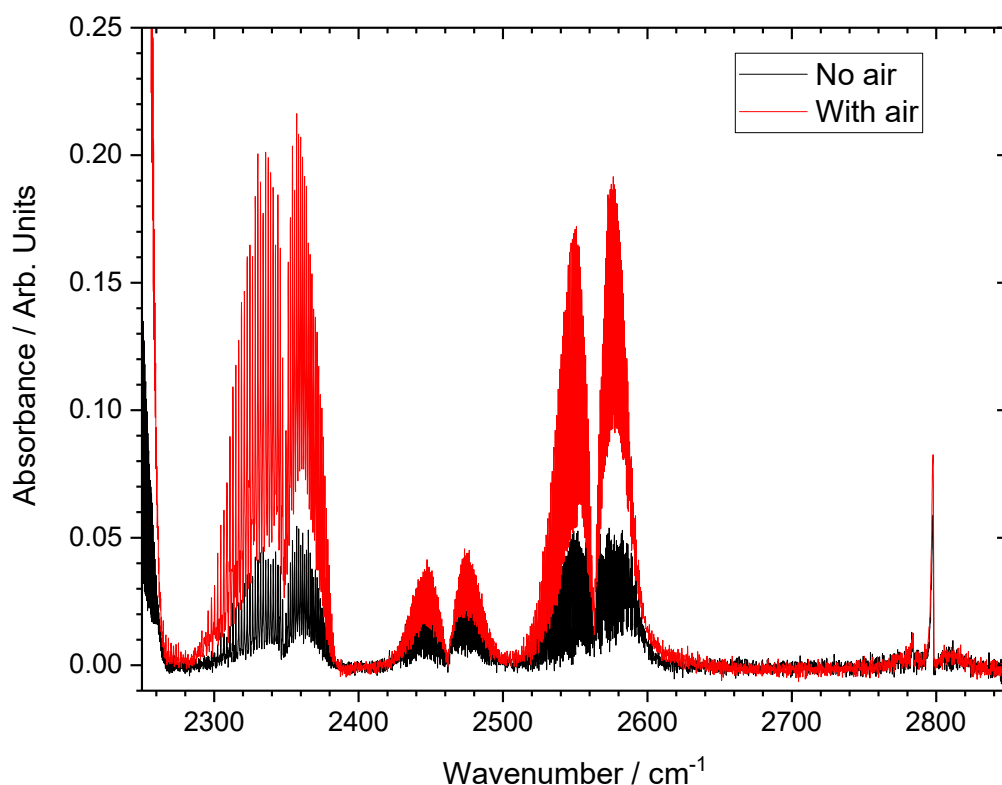
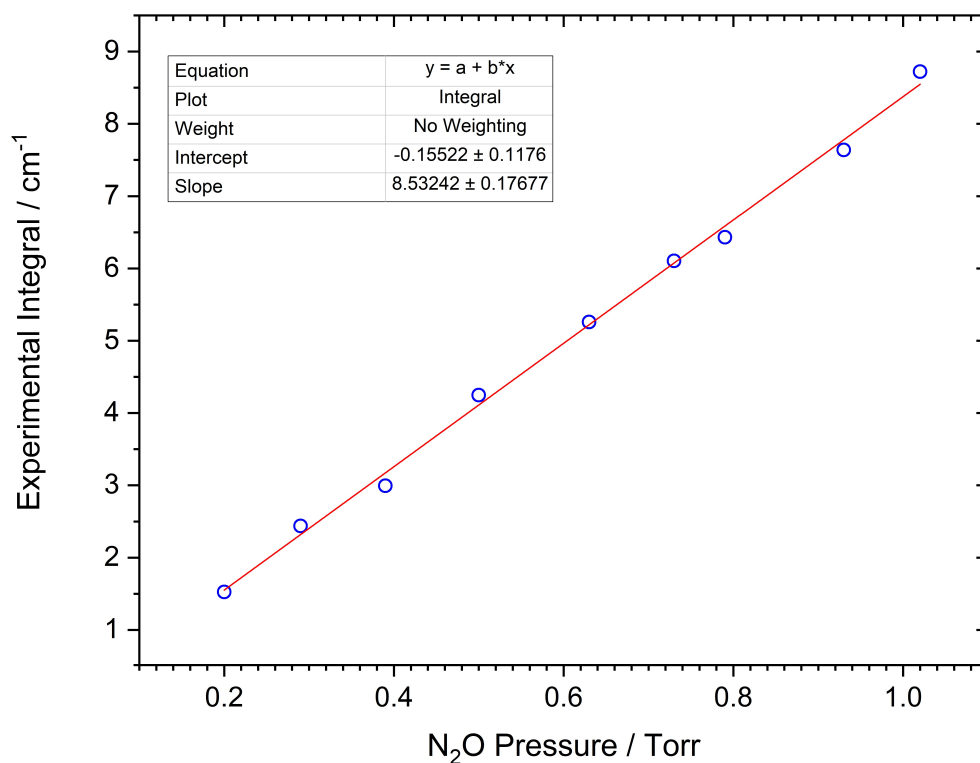


**Figure 2.14** – Single pass measurement of N<sub>2</sub>O using a single pass cell ( $l = 14.5$  cm) and a pyroelectric DTGS detector. As in Figure 2.12, the black trace is an FTIR spectrum recorded with N<sub>2</sub>O alone; the red trace shows the impact of backing up the same sample with air.

Since the same anomaly was observed even with a much simpler optical setup and using an entirely different class of IR detector, it was clear that the anomalous peak

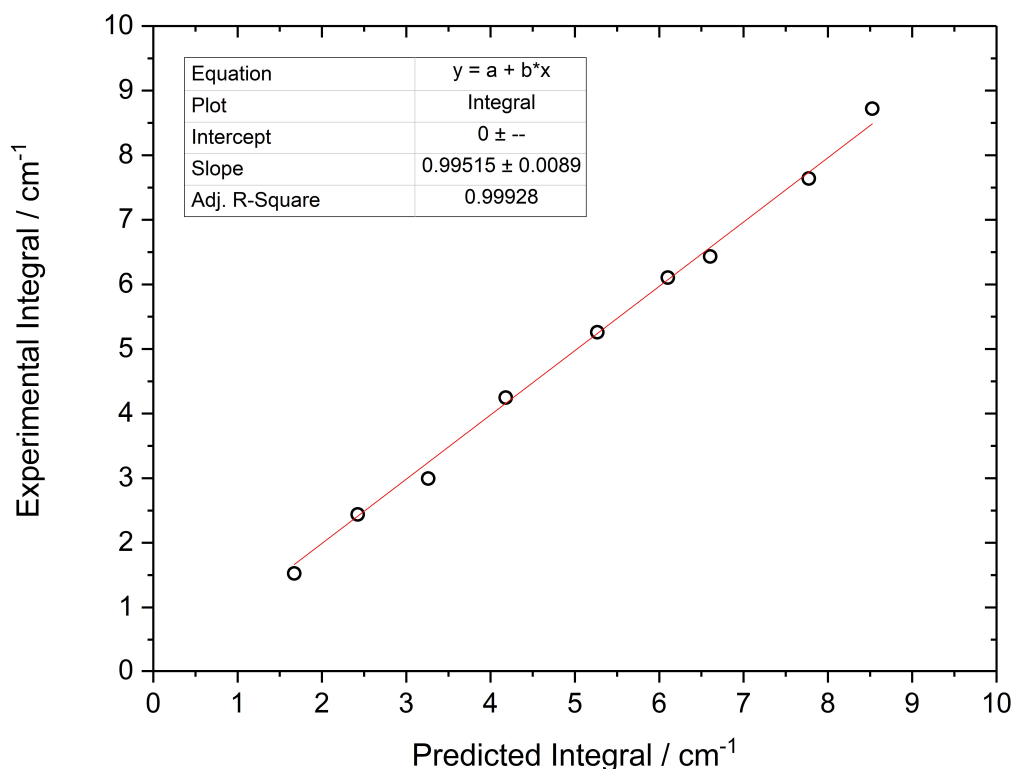
intensities were most likely due to the sample itself and probably reflected a mismatch between the instrument resolution ( $0.4 \text{ cm}^{-1}$ ) and the true linewidth of each rotational line. According to theory, the width of rovibrational lines for gases in the IR region is governed by a number of factors including the temperature and total pressure. Under standard conditions, the width of the rovibrational lines is dominated by pressure or lifetime broadening and typical linewidths (full width at half maximum, FWHM) are of the order of  $0.1 \text{ cm}^{-1}$ . At lower total pressures, the time between collisions is lower, meaning that vibrational lifetimes are shorter and lines are correspondingly much sharper with higher peak intensities. Based on this, it might be expected that the lower pressure sample where  $\text{N}_2\text{O}$  is only under its own pressure and not buffered with air would lead to much more intense absorption bands, whereas in fact the reverse appears to be the case Figures 2.13 and 2.14. In fact, the rovibrational lines in the low pressure spectra are simply too narrow to be correctly captured by the FTIR spectrometer even using the highest resolution setting available on the instrument ( $0.4 \text{ cm}^{-1}$ ). Upon backing up the samples with air, the rate of collisions increases significantly, leading to shorter vibrational lifetimes and much broader rovibrational lines, with typical linewidths around  $0.1 \text{ cm}^{-1}$ . While this is still below the maximum resolution of the spectrometer, the instrument can now capture the majority of each rovibrational line leading to only a very small deviation of the measured lineshape from the true lineshape. In order to better capture the true lineshape and carry out an accurate path length calibration, each sample of  $\text{N}_2\text{O}$  used for the calibration procedure was backed up with air before taking a measurement.

Figure 2.15 shows a nine point calibration based on the integral of the  $\text{N}_2\text{O}$   $2\nu_1$  band. As can be seen, within this pressure range, the band shows excellent linearity with increasing  $\text{N}_2\text{O}$  filling pressure. At higher pressures, the band begins to saturate and the integral no longer increases linearly with the  $\text{N}_2\text{O}$  partial pressure ( $p \text{ N}_2\text{O}$ ). For somewhat higher concentrations, the weaker  $\nu_1 + 2\nu_1$  band can be used, extended the dynamic range



**Figure 2.15** – White cell calibration plot showing the integral of the  $2\nu_1$  band as a function of  $N_2O$  partial pressure. In this region, this particular feature is not saturated and shows excellent linearity across the range of pressures tested.

In order to determine the White cell path length, the measured band integrals were compared with band integrals from spectra simulated using data extracted from the HITRAN 2012 database with rotational lines convoluted with a Lorentzian profile to simulate the effects of 1 bar pressure broadening in air.<sup>1</sup> For each filling pressure, a simulated absorption spectrum was generated assuming an 8 m path length. Figure 2.16 shows the measured  $2\nu_1$  band integral for each filling pressure against the integrals for the same band in simulated spectra generated using cross-sections from HITRAN 2012 and assuming an 8 m absorption path length. The gradient of the plot is  $0.995 \pm 0.009$ , indicating that the predicted and measured spectra show very good agreement and that the White cell path length must be close to 8 m, as predicted by counting the total number of reflections.

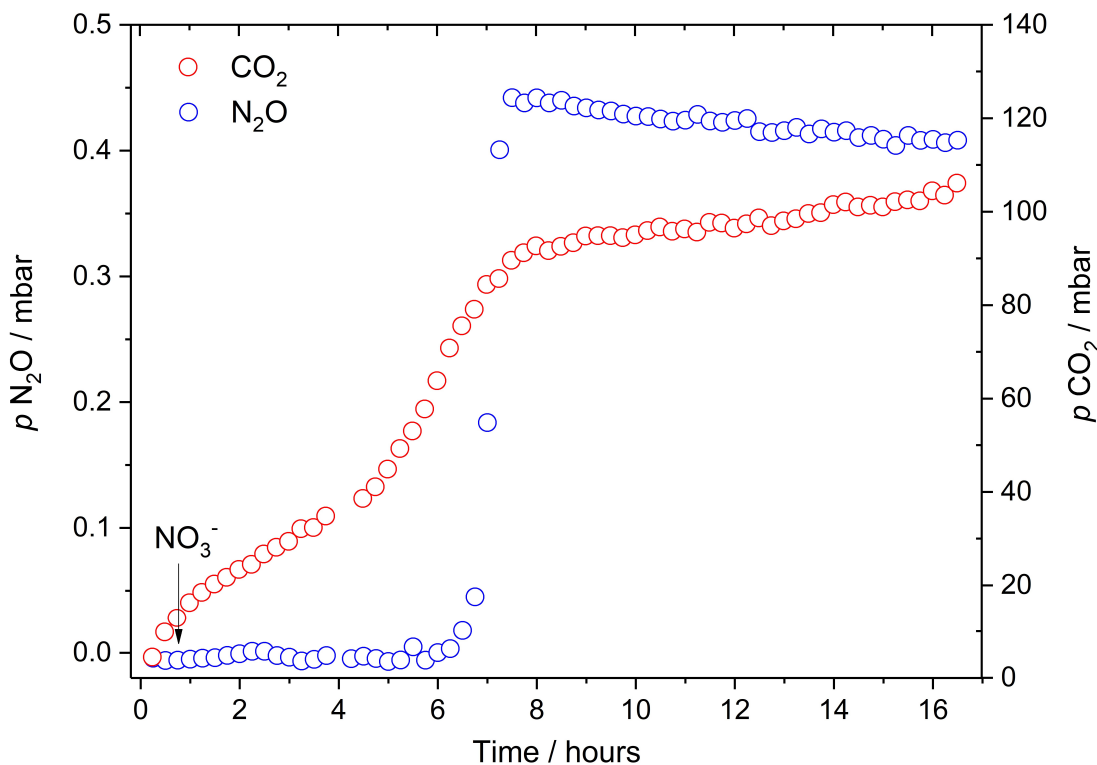


**Figure 2.16** – Comparison of N<sub>2</sub>O 2ν<sub>1</sub> experimental and predicted band integrals over the range of N<sub>2</sub>O partial pressures which showed a linear response in absorption intensity. Predicted band integrals were determined from simulated <sup>14</sup>N<sup>14</sup>N<sup>16</sup>O spectra generated using data from HITRAN and assuming 8 m absorption path length.<sup>1</sup>

### 2.3.3 FTIR Measurements of Endogenous NO Reduction

As a preliminary demonstration of the ability of FTIR to monitor NO reduction, anaerobic suspensions of *E. coli* K-12 MG1655 were prepared in a glucose-supplemented defined minimal growth medium and treated with either nitrate or nitrite. The appearance of N<sub>2</sub>O in the headspace was monitored by FTIR spectroscopy with the long path length White cell. Unlike amperometric NO measurements, FTIR spectroscopy allows direct detection of the reduction product (i.e. N<sub>2</sub>O) and provides an extremely stable system which is insensitive to solution ion concentrations and shows negligible signal drift in long term experiments carried out over several hours or even days. As an additional benefit, CO<sub>2</sub> also has strong absorption bands in the MIR region which allows for simultaneous measurements of carbon source metabolism and NO reductase activity from live cells. Attempts were made to measure NO in solution *in situ* using an amperometric sensor (ISO-NOP, World Precision Instruments) inserted into the flask through a custom built Quickfit<sup>®</sup>

adaptor. Unfortunately these measurements showed considerable instabilities in baseline current which made any accurate measurement of NO concentration impossible. This may have been due to use of a rapidly stirring magnetic stirrer bar to rapidly bring the system to equilibrium.



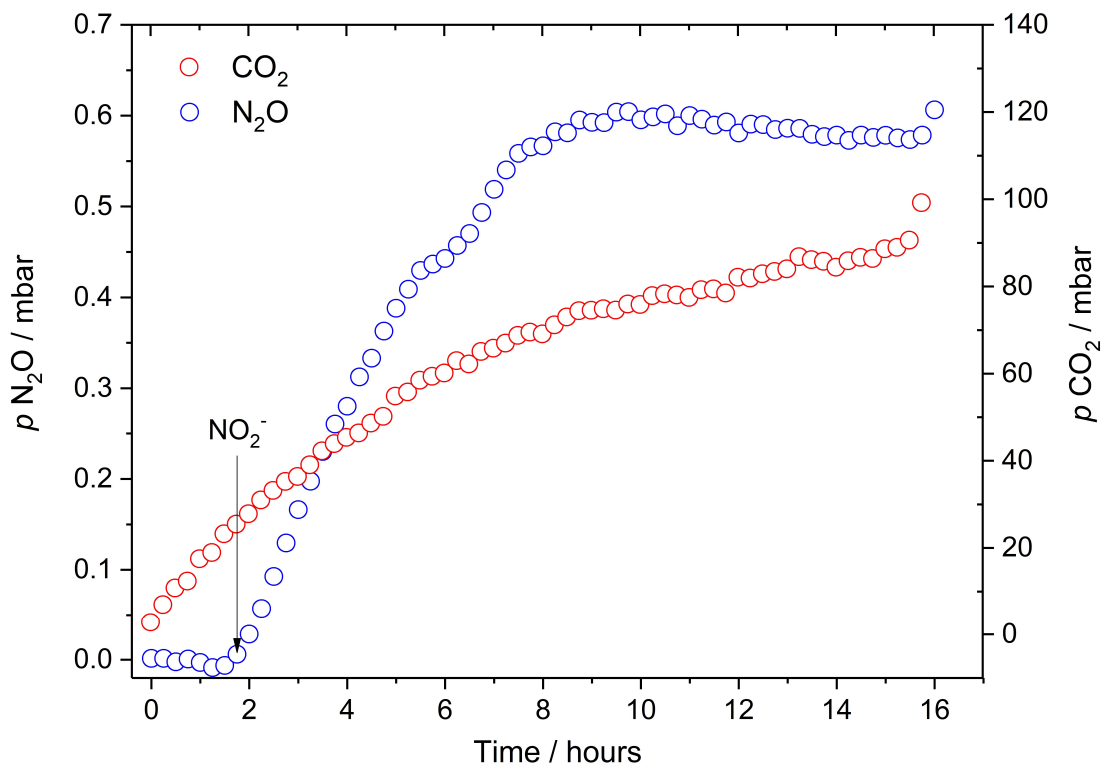
**Figure 2.17** – Kinetic plot showing  $\text{N}_2\text{O}$  and  $\text{CO}_2$  formation by nitrate treated *E. coli* as measured using FTIR spectroscopy with the 8 m White cell. Data points depict a single representative measurement. The arrow indicates when 10 mM  $\text{KNO}_3$  was added aseptically to the anaerobic culture. No  $\text{N}_2\text{O}$  was observed before nitrate addition. Rapid  $\text{N}_2\text{O}$  accumulation in the headspace occurs around five hours after addition, suggesting that some intermediate species generated from nitrate must reach a critical concentration before NO reductase activity is observed.  $\text{CO}_2$  continues to accumulate throughout the experiment, although a number of distinct phases with different rates of production are observed, possibly indicating shifts between different pathways of energy recovery (e.g. mixed acid fermentation and nitrate respiration).

Figure 2.17 shows the formation of  $\text{CO}_2$  and  $\text{N}_2\text{O}$  from a nitrate treated anaerobic culture. After allowing the culture to sit for 45 min under anaerobic conditions,  $\text{KNO}_3$  (10 mM final concentration in the culture) was added. This seems to be accompanied by an immediate slowdown in the rate of  $\text{CO}_2$  production, although no  $\text{N}_2\text{O}$  is detectable even four hours after nitrate addition, reflecting that nitrate is not directly

converted to NO in the intracellular environment. During anaerobic nitrate respiration, nitrite is generated inside the cytoplasm and exported to prevent accumulation of this potentially toxic metabolite. Unlike nitrate, nitrite can act as a NO source through both abiotic chemistry at low pH and through reactions with various metalloenzymes. While the NAD(P)H-linked nitrite reductase NirBD primarily catalyses the reduction of nitrite to ammonia, it may well represent a major source of NO *in vivo*. Six hours into the FTIR experiment, a sudden surge in N<sub>2</sub>O is detected in the system, generating a pressure of more than 0.4 mbar N<sub>2</sub>O in the headspace within an hour. This event coincides with a change in rate of CO<sub>2</sub> production, possibly indicating that a distinct shift in metabolism occurs at this point (e.g. switching from nitrate to nitrite respiration). The sudden surge N<sub>2</sub>O is not due to a blockage within the tubing suddenly being cleared during the experiment as CO<sub>2</sub> is observed to increase continuously both leading up to and after the N<sub>2</sub>O surge. After peaking, N<sub>2</sub>O is observed to decrease over time, possibly indicating either a slow leak or gas adsorption to surfaces. While *E. coli* does not possess a nitrous oxide reductase, N<sub>2</sub>O is known to attack certain cobalamin (Vitamin B12) containing enzymes, such as methionine synthase, reacting with the reduced Co(I) form to generate highly reactive oxygen radicals and N<sub>2</sub> gas.<sup>55,56</sup>

Figure 2.18 shows the formation of CO<sub>2</sub> and N<sub>2</sub>O from a nitrite treated anaerobic culture and accumulation of these gases within the enclosed system. The kinetic behaviour in this case is much simpler, with both CO<sub>2</sub> and N<sub>2</sub>O showing essentially a single kinetic regime (although there does appear to be a noticeable kink in the rate of N<sub>2</sub>O formation after six hours). Unlike nitrate treated cells, addition of nitrite leads to the immediate appearance of N<sub>2</sub>O gas in the headspace, indicating that low levels of NO are generated and reduced immediately under these conditions. Rather than releasing all of the N<sub>2</sub>O in a sudden surge, the nitrite treated culture evolved N<sub>2</sub>O continuously for seven hours, indicating either that the cellular capacity to reduce NO had become overwhelmed or that nitrite generates NO relatively slowly in the intracellular environment. Slightly more N<sub>2</sub>O is observed in the nitrite treated culture, even though the concentration of nitrite added to the culture is a quarter of the amount of nitrate added, indicating that more nitrogen is coupled into NO from exogenous nitrite than from endogenous nitrite generated by nitrate reductase activity. While further work is required to pin down the exact mechanisms behind the observed

kinetics, these preliminary data show that headspace FTIR spectroscopy can be an extremely useful new analytical tool for monitoring CO<sub>2</sub> and N<sub>2</sub>O metabolism.



**Figure 2.18** – Kinetic plot showing both N<sub>2</sub>O and CO<sub>2</sub> formation by nitrite treated *E. coli* as measured using FTIR spectroscopy with the 8 m White cell. Data points depict a single representative measurement. The arrow indicates when 2.5 mM KNO<sub>2</sub> was added aseptically to an anaerobic culture. No N<sub>2</sub>O was observed before addition of nitrite. After addition, a rapid accumulation of N<sub>2</sub>O was observed with essentially no lag phase, suggesting that NO is rapidly generated after nitrite addition.

## 2.4 Conclusions and Future Work

An 8 m path length double-row White cell has been successfully constructed, aligned and characterised using N<sub>2</sub>O. It was found that, due to the limited spectral resolution of the FTIR spectrometer, samples required buffering with air in order to avoid anomalously weak peak absorbance values. In air buffered samples, integrals obtained from experimental spectra show very good agreement with integrals from simulated spectra generated assuming an 8 m path. By comparing the experimental and predicted integrals of the 2ν<sub>1</sub> band over a range of pressures and fitting a linear

function, the White cell path length has been found to be within 1 % of the predicted 8 m path length (i.e. well within the experimental uncertainty of this method).

Using the newly characterised White cell, NO reductase activity has been measured by detecting N<sub>2</sub>O generated by anaerobic cultures of *E. coli* treated with either nitrate or nitrite. Due to the broad spectral range of FTIR and spectral discrimination, simultaneous detection of CO<sub>2</sub> was also possible, allowing general microbial metabolism to be monitored. Whereas a nitrate treated culture showed no N<sub>2</sub>O formation for six hours before a sudden burst of NO reductase activity was observed, a nitrite treated culture grown under similar conditions released N<sub>2</sub>O continuously for seven hours after addition of nitrite.

While this chapter only presents preliminary data on measurements of NO reductase activity using gas phase FTIR spectroscopy, this assay clearly holds a great deal of promise as a useful tool for exploring N<sub>2</sub>O biology in a range of organisms, not only *E. coli*. The ability to simultaneously measure CO<sub>2</sub> and N<sub>2</sub>O online and without sampling is a major advantage over other sensitive gas phase assays. In future work, the group plans to look at various mutant strains (e.g. an *E. coli* strain lacking Hcp) to see if any residual NO reductase activity can be measured. Due to the ability of FTIR spectroscopy and other forms of vibrational spectroscopy to distinguish different isotopomers, this assay can also be used for stable isotope labelling experiments (e.g. <sup>15</sup>N and <sup>13</sup>C labelling). Further applications of the White cell to CO detection are described in Chapter 4.



# Chapter 3 - Measuring CO Release from $[\text{Mn}(\text{CO})_3(\text{tpa-}\kappa^3\text{N})]\text{Br}$ , a Novel Antimicrobial Compound, with Headspace FTIR Spectroscopy

## Abstract

In this chapter, the CO release properties of a novel manganese-based carbon monoxide releasing molecule (CORM) with antimicrobial activity is reported. Headspace FTIR spectroscopy is found to be a suitable assay for monitoring CO release from  $[\text{Mn}(\text{CO})_3(\text{tpa-}\kappa^3\text{N})]\text{Br}$ , a UV photoactivatable CORM, in both sterile media and in thick broth cultures of a multidrug resistant uropathogenic *E. coli* strain.  $[\text{Mn}(\text{CO})_3(\text{tpa-}\kappa^3\text{N})]\text{Br}$  was found to release approximately 2.0 - 2.5 equivalents of CO during a 10 minute illumination phase, slightly higher than reported from the myoglobin assay carried out in sterile media. It is suggested that the higher CO yield is largely due the presence of additional ligands in the cell suspension which could displace the final CO ligand. Even in thick cell suspensions, the total free heme content is on the order of 2  $\mu\text{M}$ , meaning that CO sequestration by the cell suspension cannot be observed by FTIR spectroscopy using a conventional single pass cell. The fact that the CO yield is similar in both sterile media and thick cell suspensions indicates that photolysis represents a viable route for compound activation even in strongly scattering environments (e.g. in a heavily infected wound).

This work forms part of a scientific publication (ref. 57):

*Antimicrobial activity of the manganese photoactivated CO-releasing molecule  $[\text{Mn}(\text{CO})_3(\text{tpa-}\kappa^3\text{N})]^+$  against a pathogenic Escherichia coli that causes urinary infections*

Mariana Tinajero-Trejo, Namrata Rana, Christoph Nagel, Helen Elizabeth Jesse, Thomas W. Smith, Lauren Katie Wareham, Michael Hippler, Ulrich Schatzschneider and Robert K Poole, *Antioxidants & Redox Signaling*, 2016, **24**, 765–780.

DOI:10.1089/ars.2015.6484

## 3.1 Introduction

### 3.1.1 Carbon Monoxide as a Therapeutic Agent

Although normally considered a highly toxic gas with no role in living systems other than as an unwanted toxin, carbon monoxide (CO) is one of a number of reactive gases which is increasingly being recognised as an important messenger or signalling molecule in biology.<sup>58</sup> CO has been found to have a number of beneficial effects, including vasodilatory, cytoprotective, anti-inflammatory, anti-proliferative and anti-apoptotic actions.<sup>59</sup> Endogenous application of low levels of CO gas has been shown to protect against both hyperoxic and ischemic lung injury and suppress the rejection of transplants.<sup>60,61</sup>

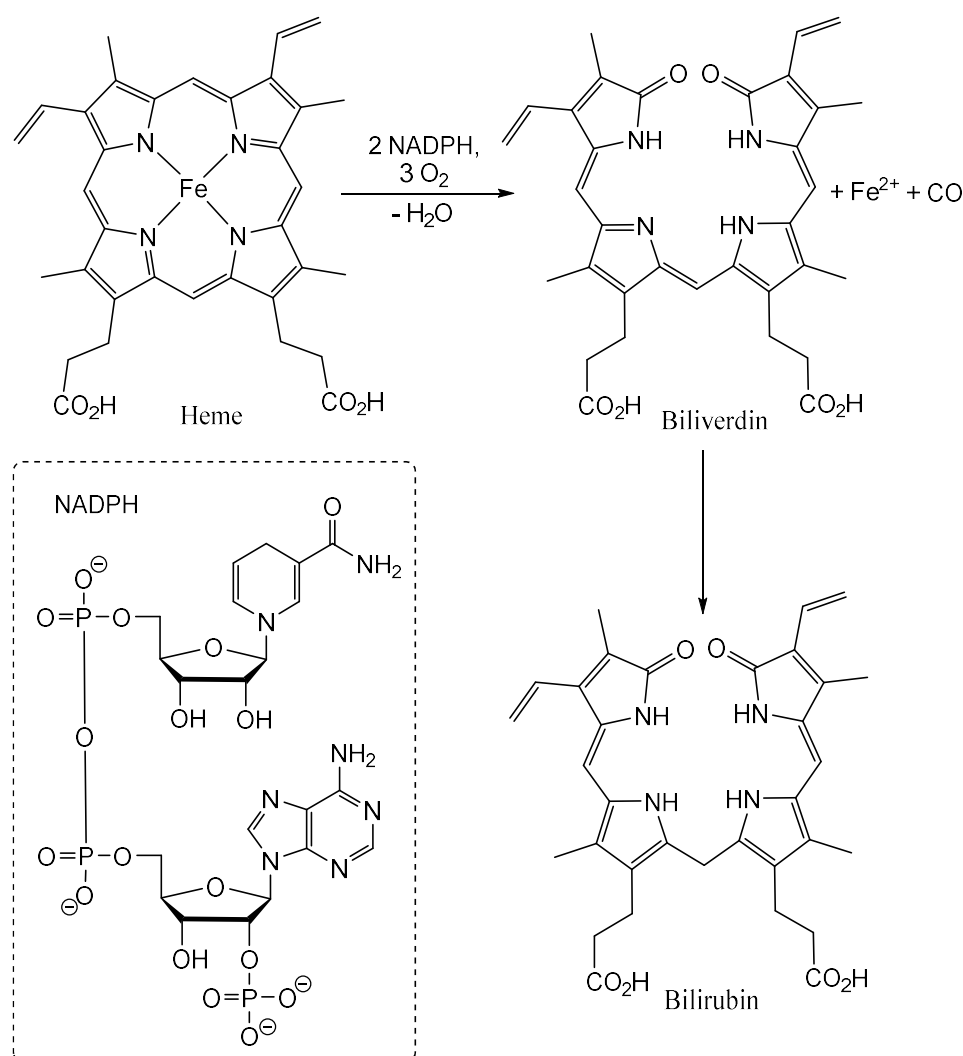


**Figure 3.1** – Heme degradation by heme oxygenase.

In eukaryotes, CO is generated almost exclusively by heme oxygenase enzymes during the oxidative degradation of heme (Figure 3.1).<sup>14</sup> This process requires three equivalents of oxygen and two equivalents of the reducing agent nicotinamide adenine dinucleotide phosphate (NADPH).<sup>15</sup> Oxidation and loss of Fe<sup>2+</sup> and CO generates biliverdin, a yellow pigment which gives the distinctive colouration to newly formed bruises. Over time, this pigment is broken down further to give bilirubin, a purple coloured pigment. The absence of one of the heme oxygenase isoenzymes, heme oxygenase 1 (HO-1), leads to serious growth defects, chronic inflammation and mortality in mice. A HO-1 deficient human patient showed similar changes in phenotype as observed in HO-1 deficient mice.<sup>62</sup> This has led to the suggestion that the ability to generate CO is essential to mammalian life, although HO-1 is also critical for heme salvage, Fe<sup>2+</sup> recovery and the formation of bilirubin and biliverdin, both of which act as reactive oxygen species (ROS) scavengers.<sup>63</sup>

Given that low level administration of CO has been reported to have numerous beneficial actions in relation to a number of disease states, developing methods for controlled CO delivery has been the focus of a great deal of research over the past 15 years.<sup>64</sup> While direct gaseous administration of CO has been demonstrated to have some beneficial therapeutic actions, it provides very little control over tissue localisation. In addition, the need to have highly specialised equipment limits this approach to specially equipped clinics. Stable CO releasing molecules (often referred to in the literature as CORMs) which release CO in a controlled and selective manner *in vivo* are the most promising approach both for biological and medical research and for clinical administration of CO. A CO prodrug could be administered through more conventional routes, either intravenously, topically or orally, making it much more viable as a treatment and could potentially lead to CO-based drugs which could be self-administered.

### 3.1.2 Carbon Monoxide Releasing Molecules (CORMs)

While a number of interesting purely organic CORMs have been reported<sup>65-67</sup>, the vast majority of CORMs in the literature are organometallic compounds based around either a transition metal or boron coordinated to one or more CO moieties.<sup>68-72</sup> Metal carbonyls have been particularly popular as candidates for CORMs due to the large

coordination sphere, which means that each molecule can carry multiple CO ligands in addition to other ligands which can be tuned to modify solubility, biodistribution and the rate of CO release (see Figure 3.2 for structures of some selected CORMs). Whereas almost all reported organic CORMs release CO photochemically and the boron-based sodium boranocarbonate ( $\text{Na}_2[\text{H}_3\text{BCO}_2]$ , CORM-A1) releases CO in response to a pH shift, metal-based CORMs demonstrate a much larger range of mechanisms through which CO can be released including ligand substitution, changes in the oxidation state of the metal and enzyme-triggered CO release in addition to pH and photochemical mechanisms. Due to the importance of transition metal carbonyls as precursors and intermediates in a number of important industrial processes, the chemistry of these complexes was already well explored before they were ever considered as CO releasing agents for biological applications. Indeed, the first example of the use of metal carbonyls in industry was the Carbonyl or Mond Process developed in the 1890s after Ludwig Mond found that metallic nickel reacted with CO gas at room temperature to form nickel tetracarbonyl,  $[\text{Ni}(\text{CO})_4]$ .<sup>73</sup> Today, transition metal carbonyls are important in a number of homogenous catalytic processes including hydroformylation of alkenes and industrial acetic acid production.<sup>74-77</sup>

The homoleptic transition metal carbonyls dimanganese decacarbonyl  $[\text{Mn}_2(\text{CO})_{10}]$  (CORM-1), and iron pentacarbonyl,  $[\text{Fe}(\text{CO})_5]$ , along with the dimeric ruthenium complex  $[\text{Ru}(\text{CO})_3\text{Cl}_2]_2$  (CORM-2) were the first synthetic organometallic complexes to be employed as CO releasing agents in a biological study.<sup>78</sup> While these compounds have less than ideal properties, they showed that metal carbonyls could be successfully employed in a biological setting for CO delivery and elicit the same biological effects as direct administration of CO gas. Despite requiring solubilisation in DMSO,  $[\text{Ru}(\text{CO})_3\text{Cl}_2]_2$  (CORM-2) has become one of the most popular CORMs for biological studies as the CO depleted species generated after CO loss do not precipitate in biological media and the compound can release CO without requiring photoactivation. In addition, CORM-2 can be synthesised relatively easily from  $\text{RuCl}_3 \cdot 3\text{H}_2\text{O}$  and is available commercially due to its use as a catalyst precursor and additive. A CORM-2 derivative,  $[\text{Ru}(\text{CO})_3\text{Cl}(\text{glycinate})]$  (CORM-3) also releases CO without requiring photoactivation but has the added benefit of being water soluble. Despite the development of newer CORMs with better physical and chemical properties, CORM-2 and 3 represent the most widely employed transition metal CORMs for biological studies.

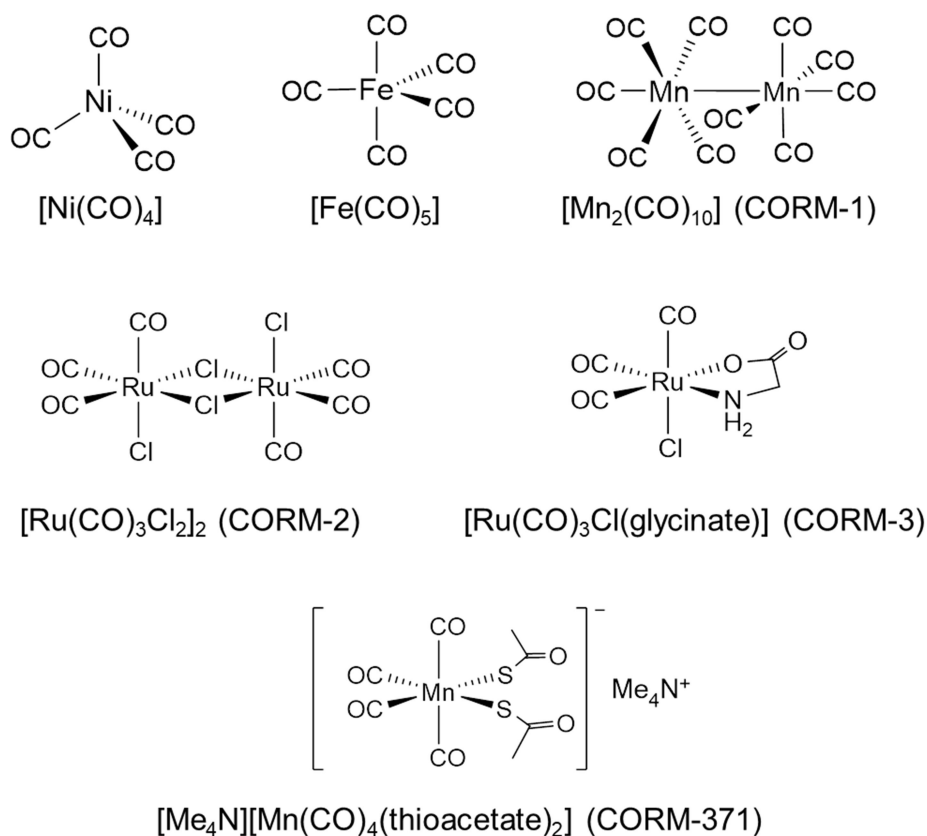


**Figure 3.2** –Structures of some selected transition metal CORMs and nickel tetracarbonyl, the first metal carbonyl to be characterised.

### 3.1.3 CORMs as Antimicrobials

A growing field of CORM research is their application as antimicrobial agents and adjuncts to improve the efficacy of existing antibiotics.<sup>79</sup> This is particularly important given the spread of resistance towards many existing antibiotics amongst pathogenic species. Ru(II)-based CORM-2 and CORM-3 have been shown to have wide spectrum activity against both Gram-negative and Gram-positive bacteria including pathogenic strains of *E. coli*, *Campylobacter jejuni*, *Staphylococcus aureus* and *Pseudomonas aeruginosa*.<sup>79–83</sup> A tryptophan functionalised Mn(I) carbonyl has recently been shown to be effective against *E. coli* and *Neisseria gonorrhoea*.<sup>84,85</sup> CORM-2 has been shown to be effective at attenuating biofilm formation in *P. aeruginosa*.<sup>86</sup> Nobre *et al.* showed that a series of structurally unrelated CORMs based around Ru, Fe and Mo had antimicrobial activity against *E. coli* and that some of these complexes also showed relatively little toxicity towards macrophages, indicating that metal-based CORMs could be developed into selective antimicrobial agents.<sup>87</sup>

There is still considerable controversy over the precise mechanism(s) of CORM's toxicity towards bacterial cells, particularly since CO gas alone often cannot reproduce the antimicrobial activity observed in CORM-treated suspensions. Catalytic ROS generation certainly seems to occur, although the study by Nobre *et al.* showed that CORM toxicity does not necessarily correlate with generation of intracellular reactive oxygen species (ROS), suggesting it may only be a minor contributor to the antimicrobial activity of metal CORMs.<sup>88</sup> On the other hand, whereas boron-based CORM-A1 only shows a bacteriostatic effect towards *P. aeruginosa*, metal-based CORM-2, CORM-3 and [Me<sub>4</sub>N][Mn(CO)<sub>4</sub>(thioacetate)<sub>2</sub>] (CORM-371) showed strong bactericidal activity, indicating the presence of a transition metal carrier is key to bacterial killing in this case.<sup>89</sup> While CO clearly does have an impact on microbial metabolism, these results suggest that the CO released by metal-based CORMs is only part of the picture. In addition to ROS generation, other potential routes of toxicity which have yet to be explored in detail are metal binding to biological Lewis bases (e.g. DNA bases, exposed N, O and S amino acid residues), a process which readily occurs when protein suspensions are exposed to CORMs with labile ligands such as CORM-3.<sup>90-93</sup> In addition, interference of foreign metals in the uptake and processing of 'natural' metals may also make a substantial contribution to the observed antimicrobial activity of CORMs.

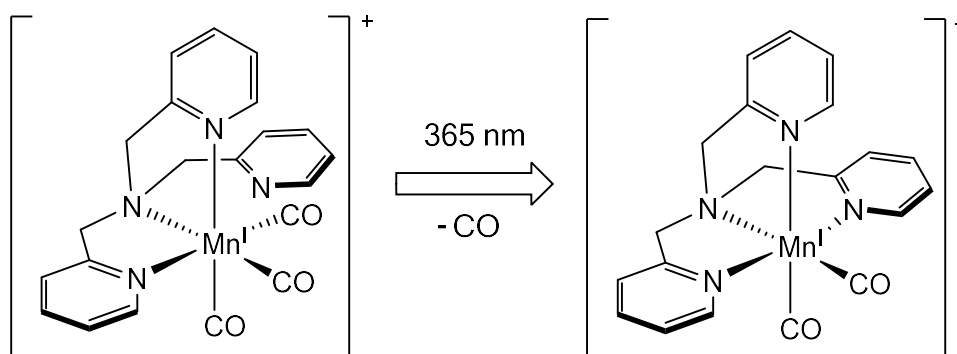


**Figure 3.3** – Structure of the UV activated photoCORM [Mn(CO)<sub>3</sub>(tpa-κ<sup>3</sup>N)]<sup>+</sup>. The free pendant 2-pyridylmethyl is positioned to cap the metal after CO release which occurs after UV illumination.

Given the obvious concerns about the potential damage caused by the metal fragment left after CO dissociation and difficulties in even identifying the chemical

nature of the CO inactive or inactivated CORMs ('iCORMs') formed after CO loss from first generation CORMs, Nagel *et al.* developed a new photoactivated Mn(I) CORM with a chelating ligand. The complex was designed to ensure that the iCORM formed after photolytic CO release would have a well-defined structure.<sup>94</sup> By using a tetradentate tris(2-pyridylmethyl)amine (tpa) ligand, the group was able to synthesise  $[\text{Mn}(\text{CO})_3(\text{tpa-}\kappa^3\text{N})]$ , an octahedral Mn(I) tricarbonyl complex where one of the 2-pyridylmethyl groups of the ligand was not coordinated to the metal. Upon CO loss, the intention was that the free group would swing into place and occupy the vacant coordination site left by the ejected CO ligand (Figure 3.3).<sup>94</sup> Since this is an intramolecular process, the coordination of the 2-pyridylmethyl group would be expected to occur more rapidly than attack by any ligands in solution, yielding a well-defined iCORM. Using quantum chemical modelling of the system (density functional theory using BP86 and B3LYP functionals) backed up by solution phase FTIR spectroscopy in DMSO, the group found that coordination of the free 2-pyridylmethyl is associated with a significant structural reorganisation barrier. In addition, in the case of water, calculations showed that the free 2-methylpyridyl group could form a stabilising hydrogen bond as one converged DFT structures showed partial proton transfer from coordinated water to the free 2-pyridylmethyl group (see Figure 3.4). Nagel *et al.* found that  $[\text{Mn}(\text{CO})_3(\text{tpa-}\kappa^3\text{N})]^+$  can potentially release all three CO ligands; two CO ligands are released through a fast photolytic process which requires UV illumination and the third through a slower dark process. This means that two vacant sites are generated which cannot be capped by the tpa ligand and are therefore free to bind biological ligands intracellularly.

Despite not meeting the original aim of the project, the complex did show interesting antimicrobial activity towards a laboratory strain of *E. coli*. Interestingly, this activity was only observed when the cells were incubated in the presence of  $[\text{Mn}(\text{CO})_3(\text{tpa-}\kappa^3\text{N})]^+$  during 365 nm illumination; the non-illuminated complex showed essentially no antimicrobial activity. This chapter describes work which formed part of a collaborative project carried out with the group of Prof. Robert K. Poole and Prof. Ulrich Schatzschneider on the mechanism(s) of antimicrobial activity and CO release by the complex with a particular focus on *E. coli* EC958, a multidrug resistant uropathogen which is sensitive towards  $[\text{Mn}(\text{CO})_3(\text{tpa-}\kappa^3\text{N})]\text{Br}$ .<sup>57</sup> As CO release and coordination to metalloproteins is at least one of the mechanisms which

contribute to the observed bactericidal action of CORMs, it is necessary to quantify CO release in the presence of cells.

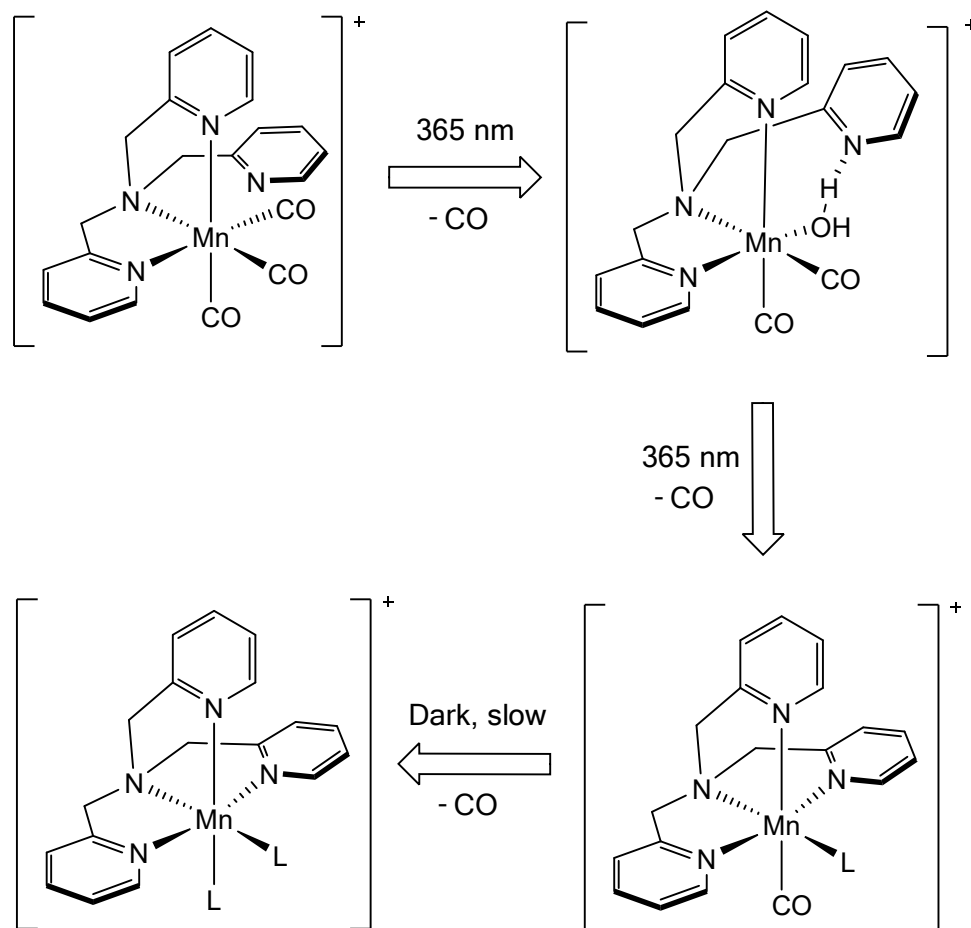


**Figure 3.4** – Possible CO release pathway based on DFT and solution FITR spectroscopy. In reality, coordination of the pendant 2-methylpyridyl is not as favourable as was originally predicted. Instead, solvent coordination (possibly involving a stabilising hydrogen bond between the coordinated water and pyridyl nitrogen) is more favourable. Coordination of the 2-methylpyridyl group appears to be more favourable after loss of a second CO moiety. Loss of the third CO is probably not photochemical and occurs comparatively slowly. L signifies a suitable Lewis basic donor (water or a suitable biological ligand).

### 3.1.4 Headspace FTIR Spectroscopy for Monitoring CO Release

FTIR spectroscopy is ideally suited to monitoring CO release from CORMs due to the distinct absorption profile and high absorption cross-section of CO gas. CO also has a very low solubility in water with a Henry constant of  $0.001 \text{ mol dm}^{-3} \text{ bar}^{-1}$ , comparable to  $\text{O}_2$  ( $0.0013 \text{ mol dm}^{-3} \text{ bar}^{-1}$ ) and  $\text{N}_2$  ( $0.0006 \text{ mol dm}^{-3} \text{ bar}^{-1}$ ), meaning that it tends to partition favourably into the gas phase. The use of gas phase FTIR to study CO release from several CORMs which release CO through photolysis, ligand substitution and pH shifts has been previously reported.<sup>95-98</sup> While FTIR spectroscopy in the solution phase is an extremely popular approach for studying metal carbonyls, providing data on both the number of CO moieties coordinated to the metal core and providing a means to distinguish different intermediates in the CO release process, the strong absorption of liquid water throughout the MIR region makes studying aqueous systems extremely difficult.<sup>99</sup> Most IR solution studies of CORMs are carried out in organic solvents precisely to avoid this problem, despite the fact that the behaviour of a CORM in an organic solvent may be considerably different to the behaviour in aqueous buffer. While gas phase FTIR is also sensitive to water vapour, the lack of large hydrogen bonded networks of water molecules in the gas phase means that the water absorption bands are relatively contained. In a high humidity environment (such as a culture headspace) certain spectral regions become completely unusable due to water absorptions but, unlike in solution, there remain a number of 'windows' which are relatively free of contamination by water vapour lines. The absorption band of CO gas happens to fall within one of these windows.

As a light, highly symmetric diatomic species, CO has a very distinct, line resolved absorption band which acts as a unique fingerprint for the molecule and allows conclusive identification without the need for a reporter group or chemical probe. The fundamental CO vibrational band is centred at  $2143 \text{ cm}^{-1}$ , although the lines which form the *P*- and *R*-branches are situated to lower and higher wavenumbers, respectively. CO has no *Q*-branch as the  $\Delta J = 0$  rovibrational transitions are forbidden (Figure 3.5).

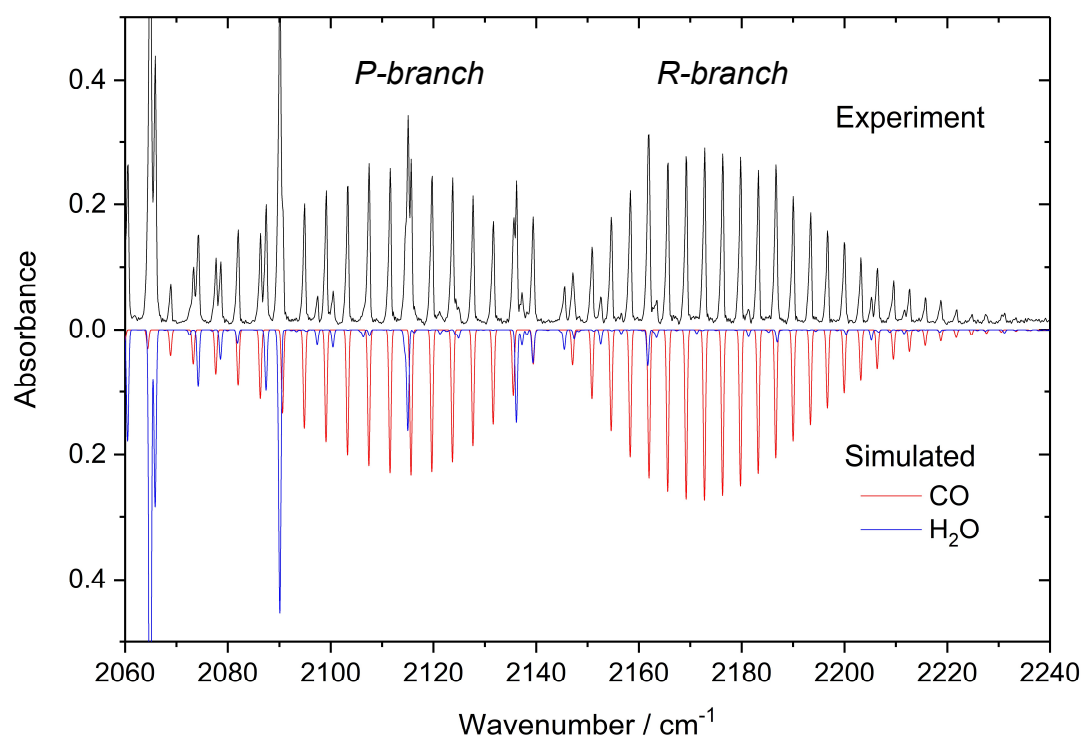


**Figure 3.5** – Comparison of an FTIR headspace spectrum and simulated absorption spectra for CO (red) and H<sub>2</sub>O (blue) based on data from the HITRAN 2012 database.<sup>1</sup> The lines resolved structure of CO is highly characteristic of this molecule, aiding identification even in complex gas mixtures.

### 3.1.5 Aims

This chapter describes the application of gas phase FTIR spectroscopy to the measurement of CO release from a photoCORM, [Mn(CO)<sub>3</sub>(tpa-κ<sup>3</sup>N)]Br, in the presence a clinically relevant multidrug resistant uropathogenic strain of *E. coli*, EC958. The CORM shows antimicrobial activity towards EC958, but only when illuminated with cells. Since release of CO and subsequent binding of the gas to terminal oxidases and other CO sensitive metalloenzymes is one of the proposed routes of CORM antimicrobial activity, it is necessary to determine if the compound can be efficiently photoactivated in strongly scattering cell suspensions. The excellent time resolution and selectivity of gas phase FTIR spectroscopy make it ideal for this application.

## 3.2 Experimental

### 3.2.1 CO Diffusion Calibration

In order to characterise the time response of the FTIR apparatus, CO saturated water was prepared by bubbling deionised water for 10 min with a continuous stream of CO gas. After bubbling, 10 mL of CO saturated water was transferred to a custom 50 mL three necked flask equipped with a 1 cm stirrer bar to ensure efficient mixing and release of CO to the vapour phase and immediately transferred to the FTIR apparatus. The flask was connected by two short transfer tubes to a 14 cm path length single pass gas absorption cell equipped with CaF<sub>2</sub> windows placed in the measurement compartment of the FTIR instrument (Matteson Research Series, DTGS detector). A peristaltic pump (nominal flow rate 7 L h<sup>-1</sup>) was placed along one of the transfer tubes to ensure efficient transfer of gases from the flask headspace to the absorption cell (Figure 3.5). After connection to the gas transfer tubes, single beam FTIR spectra were recorded every 2 min. After 5 min, the magnetic stirrer and peristaltic pump were switched on to simulate experimental conditions while spectra were recorded for a further 25 min to monitor CO accumulation in the headspace.

### 3.2.2 Growth of Dense *E. coli* EC958 Broth Cultures

Sterile LB-agar plates were streaked from a glycerol stock of *E. coli* strain EC958 using a sterile loop and incubated overnight at 37 °C until visible colonies could be identified. Plates were kept at 5 °C and were used for no more than six weeks before replacement. Before each measurement, 25 mL of LB supplemented with 10 µg mL<sup>-1</sup> Ampicillin was inoculated with a single colony isolated from the agar plate before being incubated aerobically on an orbital shaker (16 hours, 37 °C, 200 rpm). After 16 hours, the flask contents were added to 500 mL of fresh sterile LB and incubated aerobically for a further 90 min (37 °C, 200 rpm), reaching a final optical density at 600 nm (OD<sub>600</sub>) of between 1.3 – 1.5. The cell suspension was then centrifuged (Sigma 4K15, RCF 5650 g, 5500 rpm, 10 min, 4 °C) and resuspended in 10 mL sterile defined minimal medium supplemented with 20 mM glucose, giving an extremely thick suspension of OD<sub>600</sub> ~ 50.

### 3.2.3 FTIR Headspace Measurements of CO Release

To quantify CO release from the complex, 200  $\mu\text{M}$  of  $[\text{Mn}(\text{CO})_3(\text{tpa-}\kappa^3\text{N})]\text{Br}$  was added to either to 10 mL thick cell suspension or sterile glucose minimal media in a sterile 50 mL three necked flask equipped with a 1 cm stirrer bar. The same flow configuration was employed as in the control measurement described above. For cell suspensions, before addition of photoCORM, the entire system was purged with  $\text{N}_2$  for 10 min with continuous stirring to remove  $\text{O}_2$  from the system. To ensure that no CO was released during the purge or pre-illumination phase, IR spectra of the headspace were recorded at 2 minute intervals for 10 min before the sample was illuminated. After the pre-illumination phase, the sample was illuminated for 10 min at 365 nm with a 6 W transilluminator lamp (UVIlite LF-206LS, 6 W; UVItec Ltd.) placed 5 cm from the flask with IR spectra being recorded at 2 minute intervals to monitor CO release from the complex. After 10 min of illumination, the lamp was switched off and spectra were recorded for a further 40 min at 2 min intervals. To quantify CO present in the headspace, the *R*-branch of the CO fundamental band was integrated ( $2142.05$  to  $2235.1$   $\text{cm}^{-1}$ ) and compared with a 1 mbar CO spectrum stimulated using data from HITRAN 2012 and rotational lines broadened using in house software to simulate 1 bar  $\text{N}_2$  pressure broadening.<sup>1</sup>

### 3.2.4 Hemochrome Assay

Total intracellular heme concentration was determined by pyridine hemochrome assay. Dense cell suspensions prepared as described above were centrifuged (Sigma 4K15, RCF 5650 g, 5500 rpm, 10 min, 4 °C) to give cell pellets. After discarding the supernatant, the pellets were resuspended in 3 mL PBS. Two 1 mL aliquots of this suspension were added to separate 1 mL volumes of basic pyridine (1:1 v/v 1M NaOH / pyridine) in separate cuvettes. After shaking, the samples were treated with excess sodium dithionite (reduced sample) or a few grains of potassium ferricyanide (oxidised sample). After further shaking, absorption spectra of the oxidised and reduced samples were recorded between 500 – 600 nm. Total heme content was quantified from the  $\alpha$  hemochromogen band (centred at 557 nm) by plotting  $A_{\text{reduced}} - A_{\text{oxidised}}$  and using a value for the peak molar absorptivity of  $\epsilon = 19 \text{ mM}^{-1} \text{ cm}^{-1}$ .

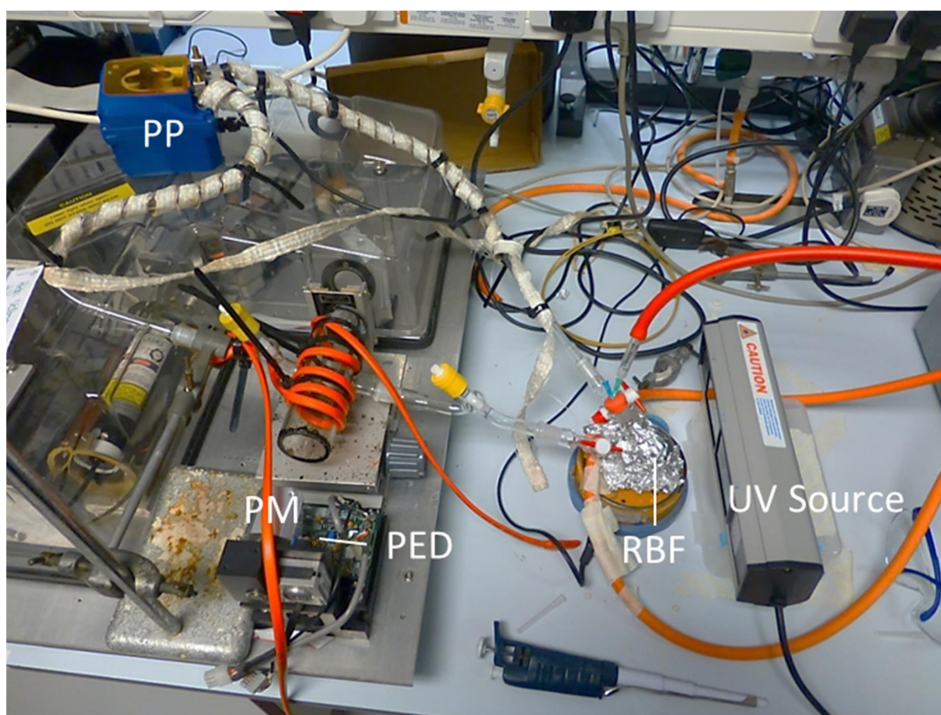
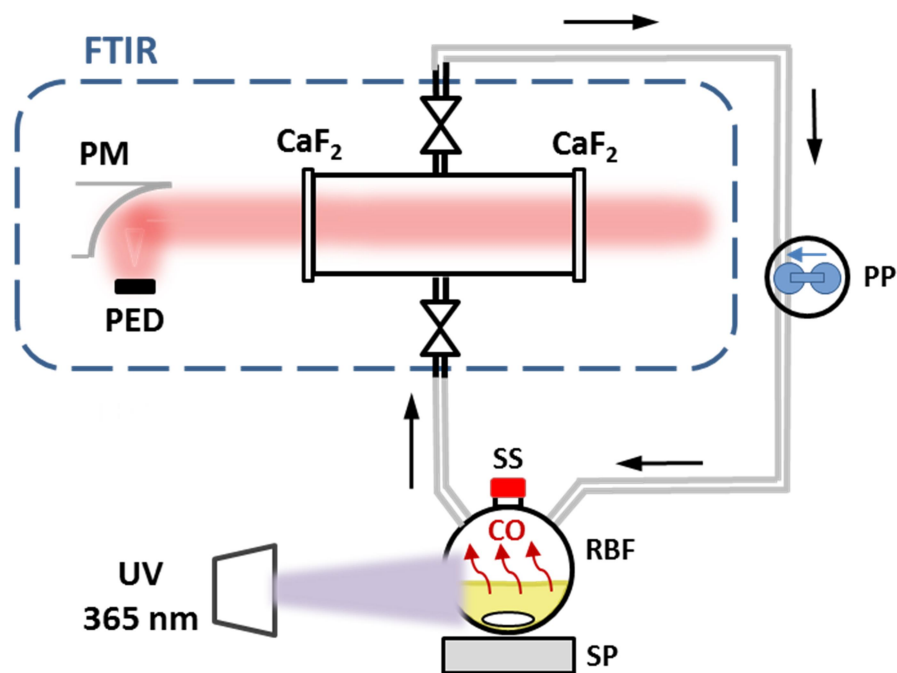


**Figure 3.6** – FTIR headspace apparatus used to measure photolytic CO release from solutions of  $[\text{Mn}(\text{CO})_3(\text{tpa-}\kappa^3\text{N})]\text{Br}$  in sterile media and in dense EC958 cell suspensions. Top: Schematic of the setup used for CO release measurements. The sterile media or cell suspensions are placed in a sterile flask **RBF** and made anaerobic by purging with  $\text{N}_2$  through a suba seal. CO generated by UV illumination of the complex is rapidly transferred to the headspace using a magnetic stirrer bar and stirrer plate **SP**. Gas flow is enforced by peristaltic pump **PP**, bringing the flask headspace into equilibrium with the rest of the system, including the single pass IR absorption cell. The IR cell is sealed with two  $\text{CaF}_2$  windows transparent above  $1000\text{ cm}^{-1}$ . After passing through the sample, parabolic mirror **PM** focuses the IR beam onto a pyroelectric detector **PED**. Bottom: Photo of setup during the  $\text{N}_2$  purge step.

### 3.3 Results & Discussion

#### 3.3.1 CO Diffusion & Short Pass Cell Characterisation

Although characterising the path length of a single pass system is trivial, it was deemed necessary to characterise the diffusion rate and flow behaviour of the system to ensure that the rate of appearance of CO signals in FTIR headspace spectra actually reflected CO release from the complex and not simply diffusion. This is particularly important given that CO observed using FTIR truly reflected the kinetics of CO release and were not simply due to diffusion effects. To test the time response of the system, CO saturated deionised water (which has a dissolved CO concentration of approximately 1 mM at room temperature) was placed into a three necked 50 mL flask, sealed and FTIR headspace spectra recorded while the solution was vigorously stirred and the headspace pumped through the system to mimic the conditions used for biological CO release measurements.

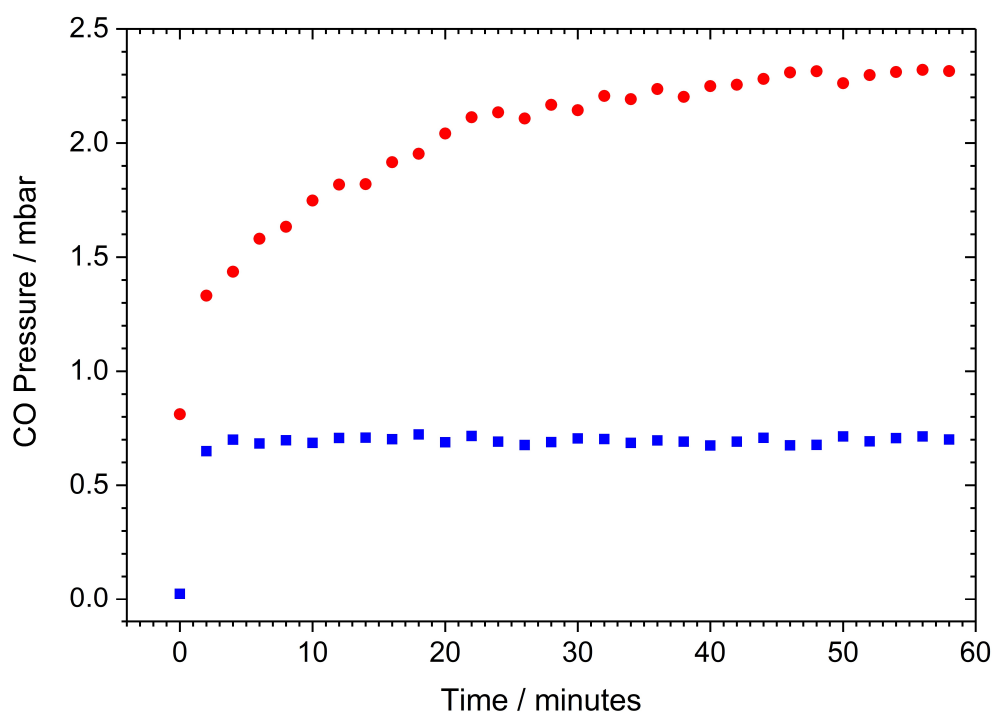


**Figure 3.7** – Characterisation of the single pass system’s time response using CO saturated water. Using a larger solution volume (25 mL) with insufficient stirring led to inefficient transfer to the gas phase (red circles). Using a smaller volume (10 mL) with a larger 1 cm stirrer bar with vigorous stirring led to efficient gas transfer (blue squares).

Relatively little CO was observed in the headspace when the pump remains off, despite CO having little tendency to remain dissolved in an aqueous environment. Upon switching the pump on, CO immediately reached its peak value within the time response of the FTIR instrument when a small volume of CO was employed with vigorous stirring (i.e. within 2 min, see Figure 3.7). Within the experimental scatter, no more CO was observed to accumulate in the headspace, indicating that the system's time response is limited by the scan rate of the instrument rather than CO equilibration. With 25 mL liquid volume and inefficient stirring with a 5 mm stirrer bar, it takes around an hour for CO levels in the gas phase to reach a plateau. This shows just how critical efficient stirring and pumping are in order to ensure rapidly equilibration of the headspace volume and solution phase, even for a relatively light gas with poor water solubility. The considerably higher CO yield in the experiment with 25 mL CO saturated water simply reflects that a larger amount of CO was added to the system.

### 3.3.2 Measuring CO Release from $[\text{Mn}(\text{CO})_3(\text{tpa-}\kappa^3\text{N})]\text{Br}$

A key criterion for developing a photoCORM for use in treating inflammation arising from deep tissue infections, such as urinary tract infections, is the ability to effectively activate the compound at the wound or infection site. In the work published together with the FTIR results described in this chapter, the photoactivated Mn(I) CORM  $[\text{Mn}(\text{CO})_3(\text{tpa-}\kappa^3\text{N})]\text{Br}$  was found to have antimicrobial activity towards a multidrug resistant uropathogenic *E. coli* (UPEC), EC958.<sup>57</sup> Similar antimicrobial activity was not found for either the non-illuminated compound or the same period of UV illumination without the compound, pointing towards either some intermediate or end product (either CO or some metal species) leading to the observed activity against EC958. If  $[\text{Mn}(\text{CO})_3(\text{tpa-}\kappa^3\text{N})]\text{Br}$  or related photoactivated CORMs are ever to be used to treat urinary tract or deep tissue infections, the feasibility of *in situ* illumination needs to be considered. Photolysis of  $[\text{Mn}(\text{CO})_3(\text{tpa-}\kappa^3\text{N})]\text{Br}$  occurs at 365 nm, which is not ideal for clinical applications due to the potential of UV radiation to cause serious tissue damage and also due to poor tissue penetration. The use of optical fibers or fluid light guides has been demonstrated for photodynamic therapy (PDT), where normally non-toxic transition metal complexes or organic chromophores are illuminated to generate reactive singlet oxygen ( $^1\text{O}_2$ ).<sup>100,101</sup> A

similar approach could be used to deliver light for photolytic CO release from photoCORMs.

Although use of some sort of light guide could potentially remove issues surrounding UV penetration through a large depth of tissue, the activation environment would still contain considerably more scattering or absorbing material than would be found under the highly controlled conditions of an *in vitro* assay such as the myoglobin (Mb) assay, commonly used to assess the CO releasing behaviour of CORMs. This means that photoCORM activation kinetics and yields determined with the Mb assay represent a ‘best case’ scenario where minimal absorption and scattering losses are occurring. As demonstrated in the previous chapter, by looking at the headspace rather than using a direct solution assay, gas phase FTIR spectroscopy can provide quantitative data regarding the formation of gaseous species even when the conditions in solution make direct detection in solution challenging or impossible.

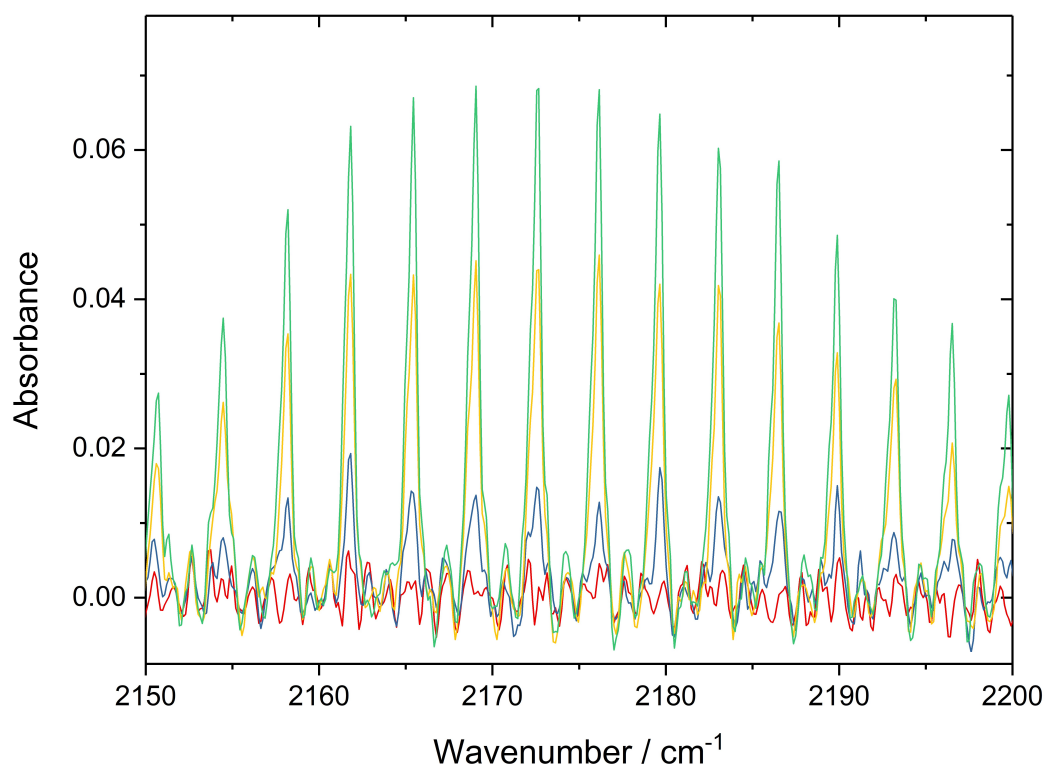


**Figure 3.8** – A portion of the *R*-branch of the CO fundamental band clearly showing the accumulation of CO gas in the headspace during illumination of photoCORM samples 1 (red), 3 (blue), 7 (gold) min after starting illumination and immediately after switching the UV lamp off (green).

In an attempt to simulate a severe infection, the CO release from UV activated  $[\text{Mn}(\text{CO})_3(\text{tpa-}\kappa^3\text{N})]\text{Br}$  was measured in dense cultures of a urinary tract pathogen, *E. coli* EC958. CO release from this CORM has previously been characterised using the Mb assay, although measurements had to be staggered with illumination to avoid interference of the lamp with the absorption measurements. In contrast, the interferometric nature of FTIR means that it is relatively insensitive to continuous sources of radiation such as the UV transilluminator lamp used for activation so illumination can be carried out simultaneously with headspace measurements. Figure 3.8 shows the appearance of CO in FTIR headspace spectra during UV illumination of  $[\text{Mn}(\text{CO})_3(\text{tpa-}\kappa^3\text{N})]\text{Br}$ . Upon illumination, CO started to accumulate in the headspace until the lamp was switched off (see Figure 3.9). When samples were kept initially kept in the dark or the UV lamp was switched off, no increase in the intensity of CO absorption features was observed, consistent with CO release from this CORM occurring through a photolytic pathway.

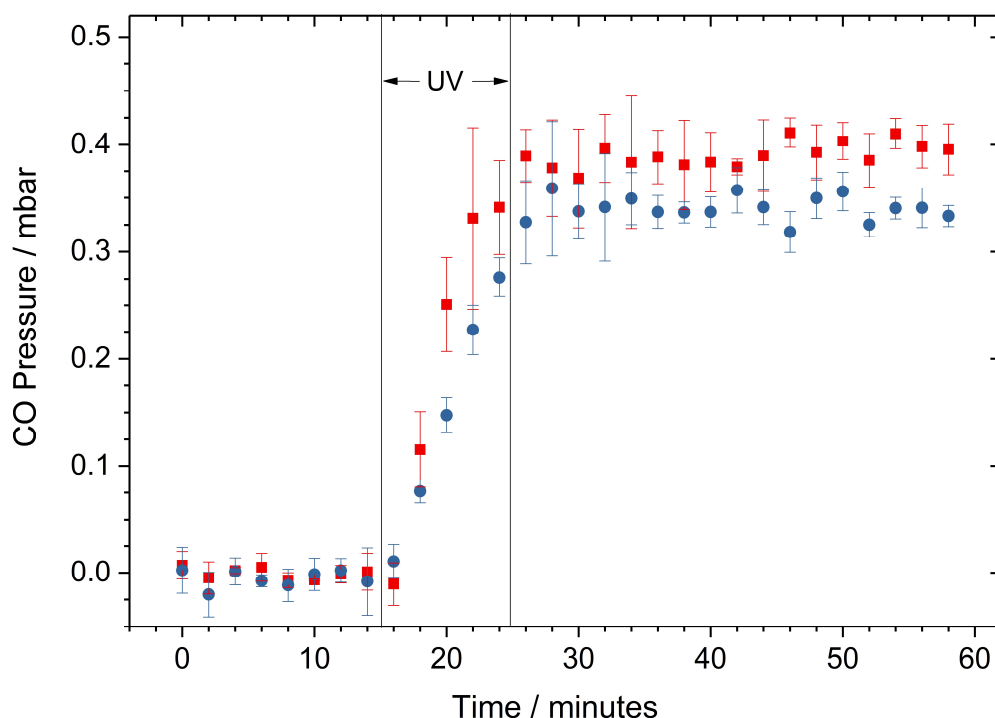


**Figure 3.9** – CO release by  $[\text{Mn}(\text{CO})_3(\text{tpa-}\kappa^3\text{N})]^+$  ( $200 \mu\text{M}$ ) as measured by headspace FTIR measurements in sterile growth media (red squares) and thick cell suspensions of EC 958 (blue circles). Samples were kept in the dark for 15 min before being exposed to a 6 W 365 nm transilluminator lamp for 10 min, as indicated on the figure. Error bars represent the standard deviation ( $1 \sigma$ ) of 3 biological repeats.

Upon illumination, CO started to accumulate in the headspace until the lamp was switched off after 10 min; this period was chosen as it had been previously determined as the longest continuous period for which EC958 could be illuminated without signs of cytotoxicity. After illumination, CO accumulation halted and no further accumulation was observed over the remaining 35 min for which spectra were recorded. A slight reduction in CO yield was observed in dense cell suspensions, with an average of 0.34 mbar CO (320 ppmv) being released to the headspace, compared to 0.39 mbar (390 ppmv) in sterile media controls. This corresponds to approximately 2.5 equivalents of CO being released from the complex, consistent with loss of two coordinated CO ligands and the partial loss of a third ligand. Illumination in dense cell suspensions led to only 2 equivalents being released. This result would appear to corroborate early studies; the slightly enhanced yield may be due to partial non-photolytic ligand displacement in due to the more complex nature of the medium.

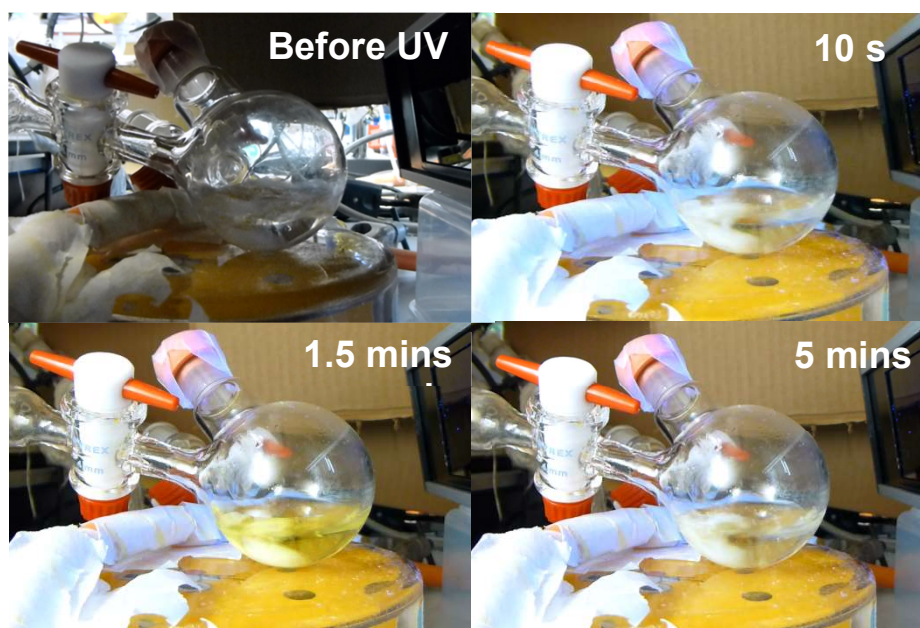


**Figure 3.10** – Colour changes exhibited by solution of  $[\text{Mn}(\text{CO})_3(\text{tpa-}\kappa^3\text{N})]\text{Br}$  ( $200\ \mu\text{M}$ ) in sterile media immediately before and after 10 s, 1.5 min and 5 min 365 nm illumination. A very intense golden yellow colour develops over the two min of illumination before completely disappearing after 5 min.

In sterile media, distinct colour changes were observed when the photoCORM was illuminated at 365 nm. Within the first two min of illumination, an intense yellow colouration was observed to appear which persisted for approximately 4 min before the solution became colourless (see Figure 3.10). This suggests the presence of at least one and possibly more intermediate species involved along the photolysis pathway. Unfortunately the extremely high density of the cell suspension measurements made it very difficult to assess any colour change in cell suspensions.

Another notable observation, possibly more relevant to the biological activity of the compound, is the appearance of a thin film of orange precipitate on the magnetic stirrer bars used in the sterile media control measurements. Mn(I) represents a particularly unusual oxidation state only commonly found amongst manganese carbonyl complexes. The significant backbonding contribution from the metal centre to coordinated CO ligands tends to stabilise lower oxidation states; loss of multiple CO ligands via a photolytic mechanism may well lead to an unstable site which becomes oxidised, forming insoluble mixed valence manganese oxides. If precipitation of end products is occurring within bacterial cells, this may well contribute to some of the observed cytotoxicity of the light activated complex.

### 3.4 Conclusions

Gas-phase FTIR spectroscopy provides a direct, *in situ* measurement of the headspace, without the need for sampling. While CO release from CORMs has been previously studied using a similar headspace FTIR approach, this chapter describes the first application to measurements above cell suspensions. By moving CO detection into the gas phase, the problems associated with specific and selective detection in a chemically complex and highly scattering cell suspension are avoided. Gas phase FTIR has been successfully employed to measure CO release from a novel photoCORM,  $[\text{Mn}(\text{CO})_3(\text{tpa-}\kappa^3\text{N})]\text{Br}$ , which shows antimicrobial activity towards and multidrug resistant uropathogenic *E. coli*. The particularly favourable partitioning of CO for the gas phase combined with the large absorption cross-section and distinctive line resolved IR spectrum of CO along makes gas-phase FTIR a particularly promising technique for further studies of CO release from CORMs in complex cellular environments.

The fact that the presence of very high cell densities appears to have a negligible impact on CO release indicates that UV illumination *via* some sort of light guide may well be a feasible approach for treatment of deep tissue infection. However, an increasingly large number of CORMs are being reported which can be photoactivated using visible or even NIR light which is obviously preferable to UV activated photoCORMs.<sup>65,67,102–104</sup> NIR activated photoCORMs with antimicrobial activity could be particularly useful for treatment of subdermal infections due to the relatively high tissue penetration of NIR radiation. In addition, while next generation CORMs such as appear to have much better properties for biological applications, clearly considerable structural refinement and careful molecular design is required to avoid or reduce issues such as precipitation which makes application in a biological setting difficult. Moving to larger, hydrophilic polydentate ligands or even CORM-protein adducts is a promising way to improve solubility and reduce issues associated with metal toxicity.<sup>92</sup> Ironically, this approach actually represents a move back towards some of the earliest studies where CO adducts of heme proteins were employed as convenient sources of CO.

## **Chapter 4 - CO Releasing Properties of the Water Soluble [Ru(CO)<sub>3</sub>Cl(glycinate)] (CORM-3) in Bacterial and Mammalian Media.**

### **Abstract**

The stability of [Ru(CO)<sub>3</sub>Cl(glycinate)] (CORM-3), one of the most commonly employed CO releasing agents in biological studies, was tested in a range of different biological media and with various additives using headspace FTIR to monitor CO release. CORM-3 was found to be highly unstable in phosphate buffer and chloride rich media, where CO releasing species have a half-life of less than 5 min in 30 mM KPi buffer. CORM-3 was somewhat more stable in complex mammalian media, but was still found to show a noticeable drop in CO yield with increasing incubation times. Despite evidence that amino acids can interact with CORM-3 *in vitro*, addition of CORM-3 to a number of amino acids does not trigger CO release. Illumination of CORM-3 with an intense 365 nm source led to slow but detectable CO release. Based on these findings, it is suggested that use of CORM-3 as a CO releasing agent in biological studies should be seriously questioned.

This work was part of a collaborative project with the group of Prof. Robert K. Poole and forms part of a manuscript currently under preparation for submission;

***CORM-2 and CORM-3 interact with amino acids – implications for toxicity to bacteria and mammalian cells, and new insights into their CO release under experimental conditions***

Hannah Southam, Thomas W. Smith, Mike Williamson, Chunyan Liao, Laurence Middlemiss, Sherif El-Khamisy, Michael Hippler, Brian Mann, Peter Henderson and Robert K Poole, *in preparation*.

A number of preliminary measurements and all of the saline CORM-3 deactivation measurements were carried out by Laurence Middlemiss.

## 4.1 Introduction

### 4.1.1 Ruthenium (II) CO Releasing Molecules CORM-2 and CORM-3

As explained in Chapter 3, CO gas has a number of potentially beneficial therapeutic effects at low doses. As CO gas itself is less than ideal for use in medicine, extensive research has been carried out into CO releasing agents (CORMs) which can be more easily administered to patients (e.g. orally or intravenously) and release CO in the body. The Ru(II) based  $[\text{Ru}(\text{CO})_3\text{Cl}_2]_2$  (CORM-2) and  $[\text{Ru}(\text{CO})_3\text{Cl}(\text{glycinate})]$  (CORM-3) represent by far the most widely used CO releasing agents for both *in vitro* and *in vivo* studies. As with many of the early CORMs,  $[\text{Ru}(\text{CO})_3\text{Cl}_2]_2$  was known well before its use as a CO donor, in this case as a precursor in the synthesis of other ruthenium carbonyls and as a model for certain catalytic systems. The dimeric complex is generated by heating  $\text{RuCl}_3 \cdot 3\text{H}_2\text{O}$  under a CO atmosphere in a non-coordinating solvent such as ethanol (Figure 4.1). Further incubation under more forcing conditions generates a ‘yellow solution’ which contains the dimeric complex.

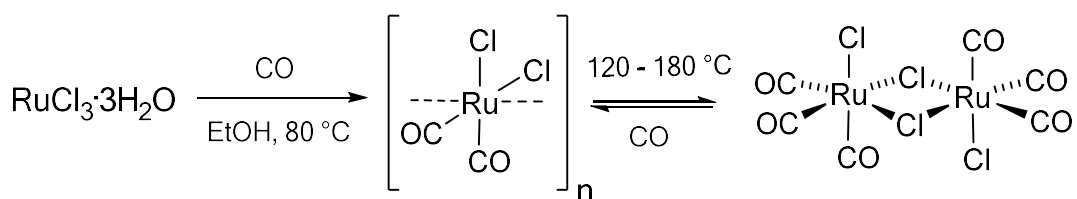


**Figure 4.1** – Synthesis of CORM-2 from  $\text{RuCl}_3 \cdot 3\text{H}_2\text{O}$  proceeds via a polymeric intermediate.

CORM-2 has been reported to release between 0.7 and 1 equivalents of CO using the Mb assay despite possessing six CO moieties coordinated to the two metal centres. As mentioned in the previous chapter, CORM-2 requires solubilisation in DMSO before it can be used in an aqueous environment. While this is not unusual amongst more hydrophobic organic drugs, DMSO solubilisation of CORM-2 actually leads to the generation of an equilibrium mixture of several monomeric complexes with different chemical structures to the Ru carbonyl dimer (see Figure 4.2). This solubilisation occurs with loss of CO, as demonstrated by previous FTIR studies which show the formation of dicarbonyl species in DMSO solution (implying CO loss) and that solid CORM-2 treated with DMSO released CO gas into the headspace of a sealed IR cell.<sup>96</sup> Unfortunately, this basic chemistry of CORM-2 is often neglected in the CORM literature.

CORM-3 is a water soluble derivative of CORM-2 synthesised by treating the dimeric complex with glycine in the presence of sodium ethoxide.<sup>105</sup> Like CORM-2, CORM-3 is a Ru(II) complex which has been reported to release a maximum of 1 equivalent of CO per molecule under conditions of the myoglobin assay, meaning that CORM-3 delivers the same amount of CO as CORM-2 but only contains half as much Ru. While a direct comparison with cytotoxicity is difficult as the complexes are structurally distinct, CORM-2 is noticeably more toxic towards cells than CORM-3. In addition to the lower Ru(II) content, the water solubility of CORM-3 is a clear advantage over CORM-2 and dissolution in water does not occur with release of CO, meaning that the compound's CO release profile is much cleaner.

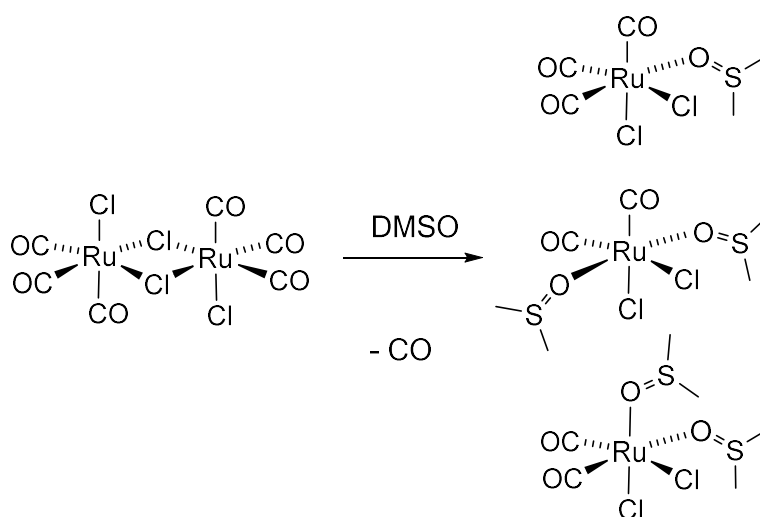


**Figure 4.2** – Solubilisation of CORM-2 in DMSO leads to at least three distinct DMSO substituted complexes.

Given the importance of developing new classes of antibiotics and the apparent low toxicity of both CORM-2 and 3 towards cultured mammalian cells, both compounds have been explored as potential new antimicrobial agents.<sup>82,83</sup> Both Ru(II) agents have been shown to have antimicrobial activity towards both Gram negative and Gram positive organisms including *E. coli*, *S. aureus*, *C. jejuni* and *P. aeruginosa*. CORM-3 is able to penetrate (or is inadvertently transported) into Gram negative cells where it is accumulated. CORM-2 was able to rescue mice infected with *P. aeruginosa*, indicating that the compound shows at least some degree of selectivity for bacterial killing.<sup>89</sup>

The antimicrobial activity of both complexes appears to be multifaceted and occurs through multiple mechanisms; CO ligation by respiratory oxidases probably represents only one of the pathways by which CORM-2/3 are antimicrobial and probably a minor pathway except in strict aerobes such as *P. aeruginosa*.<sup>87</sup> Intracellular ROS generation has been detected in the presence of both CORM-2 and 3, as might be expected for a transition metal with multiple accessible oxidation states. Interestingly, transcriptomic studies have shown that addition of CORM-2 to *E. coli* leads to significant upregulation of genes associated with methionine biosynthesis along with a massive upregulation in the expression of two genes, *ibpA* and *ibpB*, coding for heat-shock proteins along with numerous other genes associated with metal metabolism and oxidative stress.<sup>106</sup> It perhaps is not entirely surprising that CORM-2 would disrupt metal metabolism, possibly binding to siderophores. The upregulation in genes associated with methionine biosynthesis metabolism is perhaps somewhat harder to explain, however it should be noted that Ru(II) is also a relatively ‘soft’ metal centre, meaning that it shows a tendency to bind to softer Lewis acids, such as thiols, thioethers and phosphines. The upregulation of genes associated with methionine biosynthesis could reflect Ru(II) centres becoming bound to intracellular sulfur species.

#### 4.1.2 CORM-3 – A Molecule with Extensive Aqueous Chemistry

While it initially appeared that CORM-2 and 3 simply released CO in any media or buffer, McClean *et al.* showed that the CO release observed in the commonly employed Mb assay is actually triggered by sodium dithionite, the reducing agent employed to ensure that Mb is kept in the reduced, Fe(II) form which can bind CO.<sup>107</sup> By careful exclusion of oxygen and use of hemeoglobin (Hb) rather than Mb, the group showed that little or no CO release occurs when dithionite is absent. CO release was also triggered by sulfite ( $\text{SO}_3^{2-}$ ) and metabisulfite ( $\text{S}_2\text{O}_5^{2-}$ ) were also able to trigger CO release although no CO release was observed from treatment with sulfide ( $\text{S}^{2-}$ ) or N-acetylcysteine.<sup>107</sup> This finding is also in agreement with a study from Santos-Silva *et al.* where no CO release from CORM-3 could be detected above solutions of CORM-3 in phosphate buffer measured using gas chromatography; since the group were not using the conventional Mb assay, no dithionite was added to the media.<sup>90</sup> In addition to the requirement for sulfite or dithionite to trigger CO release

from the complex, the work by McClean *et al.* also showed that the yield of CO recovered when dithionite was added to a solution of CORM-3 preincubated in potassium phosphate buffer (KPi) for 10 min was reduced by half, suggesting that some deactivation of CORM-3 was occurring in buffer or alternatively that gaseous CO was rapidly lost from solution when reduced Mb was not present to sequester CO released by CORM-3.<sup>107</sup>

Like GC methods, FTIR spectroscopy of the headspace allows direct detection of CO release from metal carbonyls without the need for intermediate reagents. However, unlike GC, FTIR can be used for direct, online measurements without the need for sampling, giving excellent time resolution and removing any problems associated with sampling errors or sample loss if the experiment is conducted in a sealed system. This chapter describes the first detailed gas-phase FTIR study on CORM-3 CO release.

## 4.2 Experimental

### 4.2.1 General Procedure for FTIR Measurements of CO Release

CO release from solutions of [Ru(CO)<sub>3</sub>Cl(glycinate)] (CORM-3) in buffer, buffer components, minimal or complex bacterial or mammalian media was measured by gas phase FTIR spectroscopy (Matteson Research Series FTIR, 0.4 cm<sup>-1</sup> resolution; see Figure 4.3). Measurements on saline inactivation of CORM-3 were carried using the 14.5 cm cell described in the previous chapter and a working CORM-3 concentration of 500 μM. All other measurements were carried out using the 8 m path length White cell with a working CORM-3 concentration of 100 μM. For the single pass cell, the FTIR's pyroelectric DTGS detector was employed whereas the MCT detector was required for White cell measurements. To prevent saturation of the MCT detector, an additional sapphire window was employed to filter out frequencies lower than 2000 cm<sup>-1</sup>.

In a typical experiment, CORM-3 (100 or 500 μM final concentration) was incubated in 10 mL of the buffer or growth medium being tested. CO release upon addition of sodium dithionite, sodium sulfite, amino acids or other media components was tested for by recording spectra of the headspace at 1 minute intervals. For

overnight incubations, spectra were taken at 1 hour intervals. All experiments were carried out at 25 °C while the IR absorption cells were heated to around 40 °C to prevent condensation on the optics. The flask and gas cell were connected in series with a peristaltic pump providing a nominal flow rate of 7 L h<sup>-1</sup>. Vigorous stirring of the solution was employed to ensure efficient gas transfer. CO was quantified by comparing experimental absorption band cross-sections of CO with a simulated 1 mbar CO spectrum generated using absorption cross-sections from HITRAN 2012.<sup>1</sup>

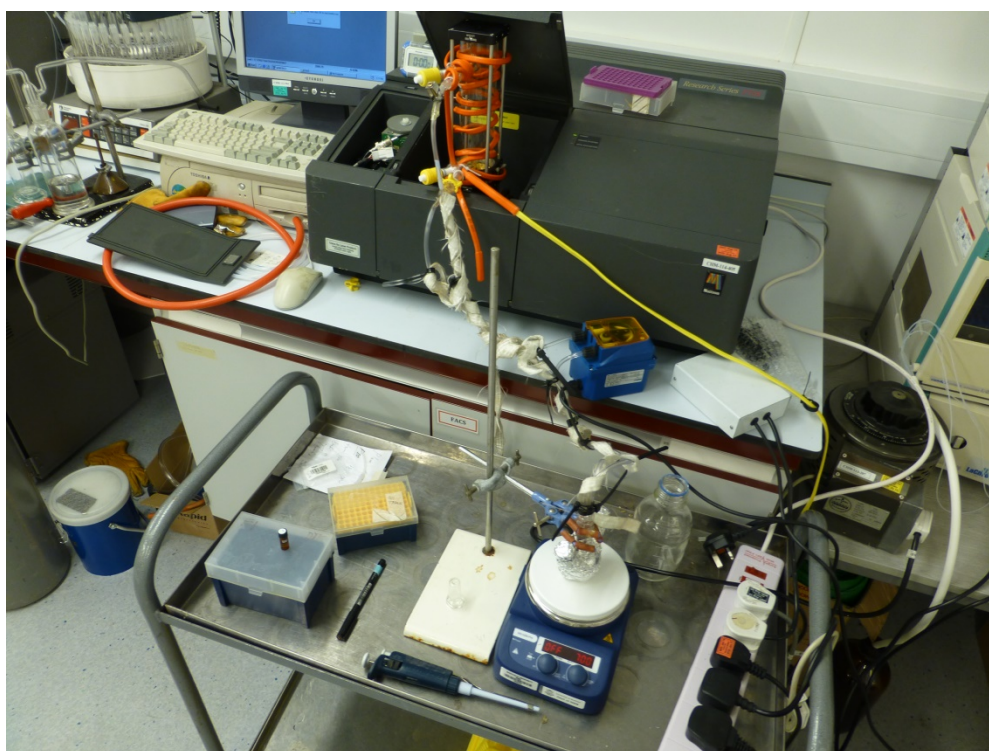


**Figure 4.3** – FTIR apparatus employed for measuring CO release from CORM-3 in various media and buffers.

#### **4.2.2 Media and Buffers**

Potassium phosphate (KPi) buffer was prepared at 30 mM concentrated, pH adjusted and sterilised by filtration through 0.22 µm filter. Roswell Park Memorial Institute 1640 (RPMI-1640) and Dulbecco's Modified Eagle's medium (DMEM) were purchased presterilised from Sigma Aldrich. All other reagents were purchased from Sigma Aldrich. CORM-3 was kindly prepared by Mr. Keith Owen (Department of Chemistry, University of Sheffield).

## 4.3 Results & Discussion

### 4.3.1 CORM-3 CO Release is triggered by Sulfite and Dithionite

The findings of McClean *et al.* strongly suggest that dithionite, sulfite and metabisulfite salts enhance the rate of CO release from both CORM-2 and CORM-3.<sup>107</sup> To confirm these findings, CORM-3 (500  $\mu\text{M}$  final concentration) was added to deionised water (10 mL) and immediately sealed to prevent CO escape. In the absence of dithionite, no CO release was observed whereas approximately 1 equivalent of CO was rapidly evolved upon addition of two equivalents of either sodium dithionite or sodium sulfite to the solution. Similar observations were made in potassium phosphate (KPi) buffer, where no meaningful CO release was observed except with addition of dithionite or sulfite. This observation is in agreement with both McClean *et al.* and Santos-Silva *et al.* as both groups observed no CO release from CORM-3 in the absence of dithionite.<sup>90,107</sup>

### 4.3.2 CORM-3 CO Release is not triggered by Amino Acids

Recent unpublished work carried out by collaborators in the Poole group suggests that glutamic acid, histidine, methionine and particularly cysteine are able to bind to CORM-3 and that binding to media components in complex media rescues laboratory strains of *E. coli* from CORM-3 toxicity. While the N-acetyl derivative of cysteine has already been tested with respect to its ability to release CO from CORM-3, none of the other amino acids have been tested for their ability to displace CO from the CORM-3 coordination sphere. To test the ability of amino acids to displace CO from CORM-3's coordination sphere, CORM-3 (100  $\mu\text{M}$ ) was added to solutions of L-histidine, L-methionine, (reduced) L-cysteine and L-glutamic acid (200  $\mu\text{M}$ ) in 30 mM pH 7.4 KPi buffer in the sealed FTIR apparatus while the headspace was monitored for 30 min for CO accumulation. Addition of CORM-3 to L-alanine (200  $\mu\text{M}$ ), which shows negligible affinity to metals, was employed as a negative control while addition of CORM-3 to sodium dithionite (200  $\mu\text{M}$ ) was employed as a positive control.

Figure 4.4 shows the CO release properties of CORM-3 when incubated in the presence of various relevant amino acids. Except in the case of cysteine, where traces of CO are observed in some experiments, all other amino acids are entirely inert

towards CO displacement, suggesting that observed amino acid binding, while relevant to CORM-3 biochemistry, is not associated with CO release.

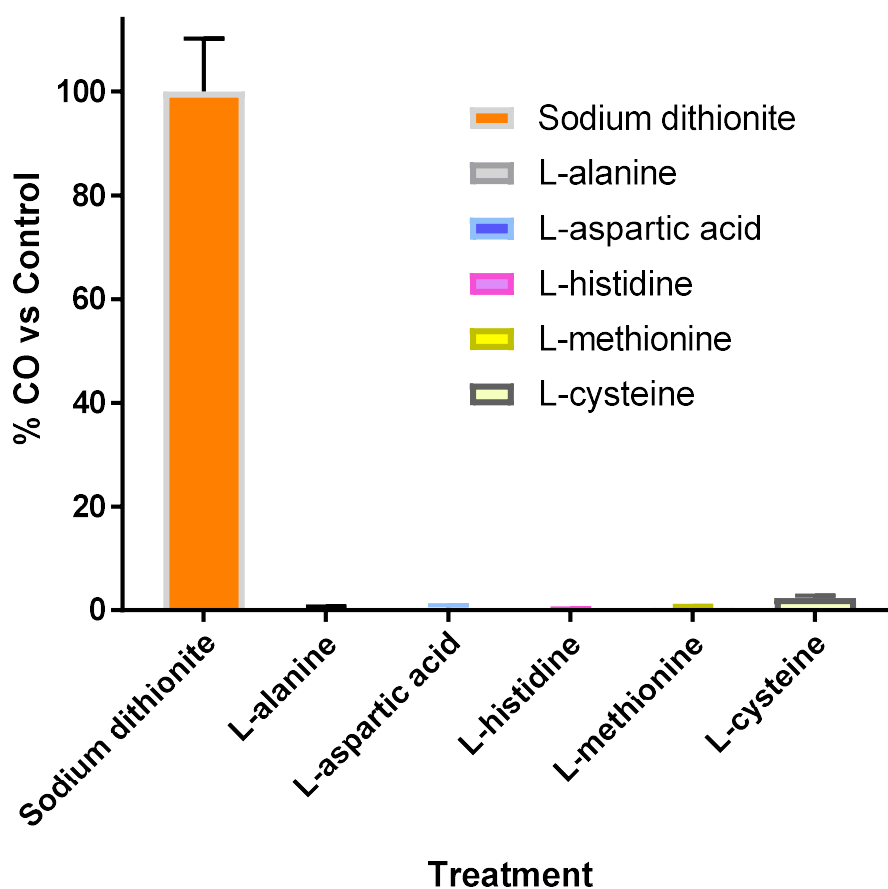


**Figure 4.4** – CO release properties of CORM-3 in the presence of various amino acids and sodium dithionite. Each bar represents the average of at least two replicates. Error bars represent the standard deviation ( $1 \sigma$ ) of experimental replicates.

### 4.3.3 CORM-3 is rapidly deactivated in Phosphate Buffers

Another interesting avenue raised by McClean *et al.* is the observation of a reduced yield of CO released from CORM-3 when dithionite was added a few min after adding CORM-3 to the other components of the Mb assay.<sup>107</sup> Their paper suggested this might be due to inactivation of the CORM-3 due to the formation of inactive species in buffer which do not release CO upon subsequent dithionite addition. However, they could not directly rule out gaseous losses to the atmosphere. As the FTIR apparatus remains sealed throughout the experiment, any CO lost before dithionite addition would be detected. To test the hypothesis put forward by McClean *et al.*, CORM-3

(100  $\mu\text{M}$ ) was pre-incubated in 30 mM pH 7.4 KPi buffer and ‘triggered’ with two equivalents of sodium dithionite after various incubation times. As a control experiment, CORM-3 was added to KPi buffer which had already been supplemented with two equivalents of dithionite.

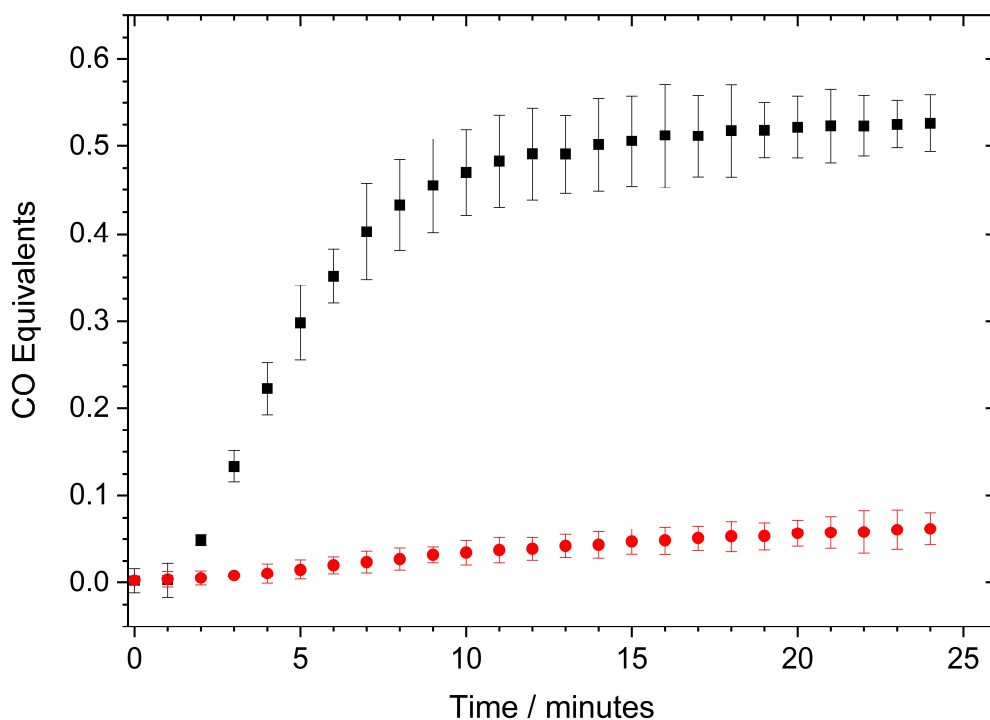


**Figure 4.5** – CO release from CORM-3 (100  $\mu\text{M}$ ) in KPi buffer (30 mM). Two equivalents of  $\text{Na}_2\text{S}_2\text{O}_2$  were added either immediately before CORM-3 addition (■) or after CORM-3 had been incubated for 5 min in buffer while connected to the FTIR apparatus (●). Error bars represent standard deviation ( $1 \sigma$ ) of two experimental replicates.

Figure 4.5 shows the impact of incubating CORM-3 in KPi buffer over 5 min before addition of dithionite compared to the control. Whereas the control experiment, where dithionite was already present in the buffer, released approximately 0.5 equivalents of CO to the headspace, incubation over 5 min led to a reduction in CO released to around 0.07 equivalents. The batch of CORM-3 employed in this series of experiments consistently released 0.5 equivalents using both gas phase FTIR spectroscopy and the Mb assay, indicating that the lower yield is not an artefact of the FTIR measurements but in fact represents some breakdown in the CORM-3 batch, despite storing the compound in a  $-18^\circ\text{C}$  freezer.

As the FTIR apparatus remained sealed throughout the entire 5 minute pre-incubation period, the lack of CO release indicates that the decrease in CO yield as a function of time must reflect some aqueous chemistry of CORM-3 which rapidly deactivates the complex towards dithionite / sulfite triggered CO release. Although FTIR headspace measurements provide no direct information on the underlying chemistry, previous solution phase  $^1\text{H}$  and  $^{13}\text{C}$  NMR and solution phase FTIR experiments have shown that CORM-3 has extensive aqueous chemistry.<sup>108</sup> Johnson *et al.* showed that in aqueous solution, CORM-3 acts as a weak acid; with increasing pH, it was proposed that one of the coordinated CO ligands undergoes attack by hydroxide to form a metalcarboxylic acid (Figure 4.6).<sup>108</sup> Addition of more base led to the formation of other ruthenium species which could not be conclusively identified, although solution phase IR measurements carried out in methanol showed that the dicarbonyl moiety remained intact throughout the base titration.

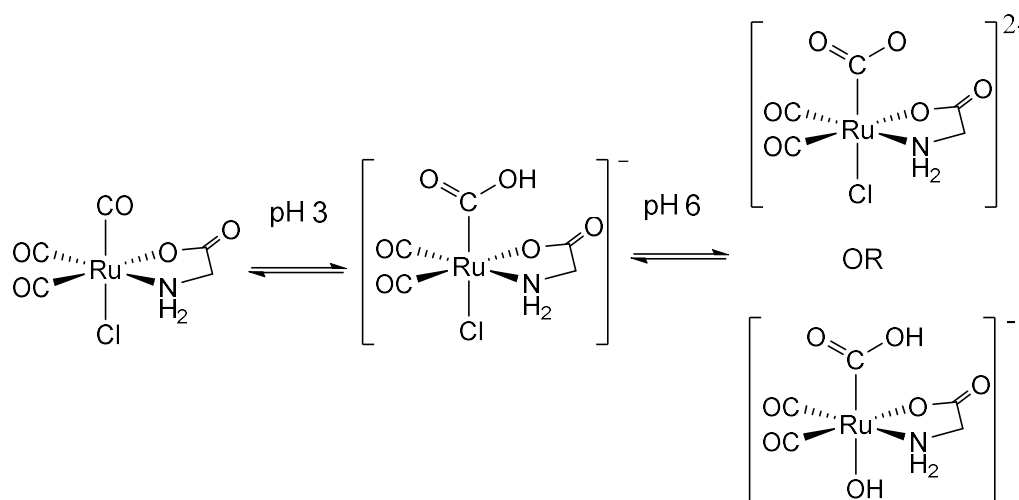


**Figure 4.6** – Changes in CORM-3 with pH changes as described by Johnson *et al.* Near neutral pH, CORM-3 actually exists as a mixture of anionic Ru complexes. Since they have considerably more electron density to back donate to the remaining two carbonyl ligands, the formation of these species may be responsible for the rapid deactivation of CORM-3 in buffer.

Since the majority of *in vitro* work is typically carried out in pH buffered systems at the rapid formation of anionic metalcarboxylate species. While the previous solution phase study suggests that only one CO is converted to carboxylate, leaving two CO ligands potentially free to dissociate, it should be remembered that even under ideal conditions only one of the coordinated CO ligands is ever observed to dissociate. The relative tendency of CO to dissociate from a metal site is strongly influenced by

the electron density on the metal (i.e. by its oxidation state and the nature of the other ligands) due to the importance of the  $\pi$  backbonding interaction to CO coordination to transition metals. The formally anionic ruthenium metalcarboxylate which dominates at pH 7 will have considerably more electron density to donate to the coordinating CO ligands, meaning that dissociation is less likely to occur. While not conclusive, the solution phase FTIR measurements (carried out in methanol) show that the carbonyl stretching frequencies of the coordinated CO ligands become increasingly more redshifted in the ruthenium species formed at higher pH.<sup>108</sup> This is consistent with a strengthening of the metal-CO bonds and a lower propensity for the remaining CO ligands to dissociate from the metal.

#### 4.3.4 CORM-3 is deactivated in Non-Buffered Saline

In addition to the pH-dependent chemistry occurring at the coordinated CO sites, Johnson *et al.* found convincing evidence that the coordinated glycine is particularly labile at the carboxylate oxygen, with the carboxylate being rapidly replaced by chloride upon addition of dilute HCl or isotonic saline to give a monodenate glycine complex which slowly converts to  $[\text{Ru}(\text{CO})_3\text{Cl}_3]^-$ .<sup>108</sup> The lability of the glycine ligand has been confirmed by a number of crystallographic studies of CORM-3 protein adducts where the glycine and chloride ligands are readily displaced by histidine and aspartic acid residues, leaving Ru carbonyl fragments.<sup>90</sup> In an attempt to identify if the presence of chloride leads to deactivation, CORM-3 (500  $\mu\text{M}$ ) was incubated in 25, 50, 100, 150 and 200 mM saline for 30 min before dithionite was added to trigger CO release which was monitored using headspace FTIR spectroscopy with a short path length cell ( $l = 14.5$  cm). As a control experiment, CORM-3 was incubated in Milli-Q<sup>®</sup> purified water. While the control released only slightly less than one equivalent of CO, decreasing yields of CO were observed with increasing concentrations of saline (Figure 4.7). Again, no CO release was observed before addition of a sulfite source, indicating that the pathway of CORM-3 deactivation is not loss of CO but instead occurs through conversion of CORM-3 to one or more species which are unable to release CO through the sulfite-triggered mechanism. The observed reduction in CO yield is consistent with the formation of deactivated chloro-substituted species which are unable to release CO upon treatment with a sulfite source.

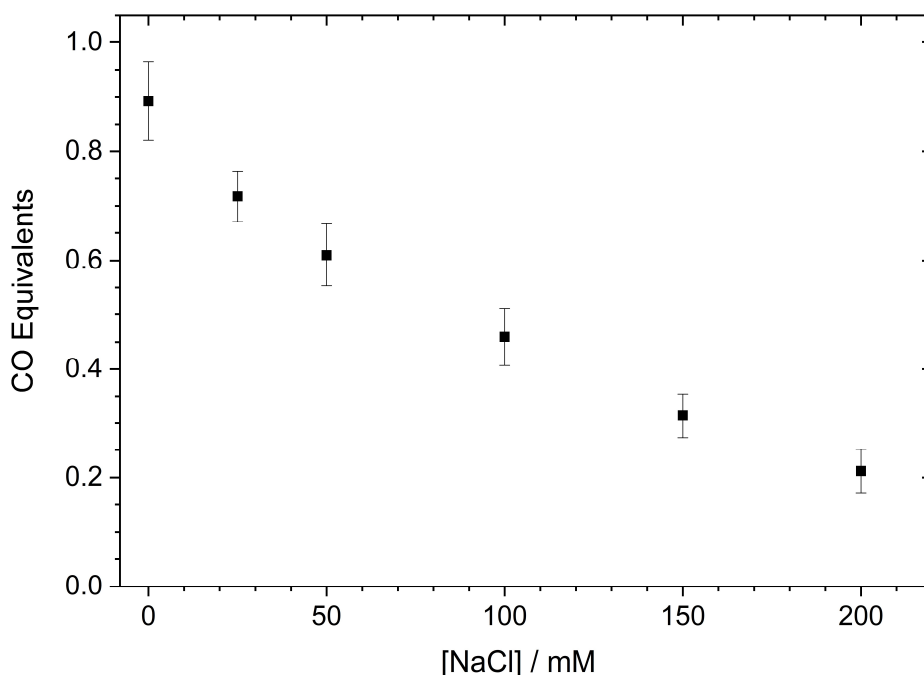


**Figure 4.7** – CO release from dithionite treated CORM-3 (500  $\mu$ M) after 30 minute preincubation in various concentrations of non-buffered saline (25 – 200 mM) and deionised water. Error bars represent standard deviation of CO levels from individual spectra collected after CO levels had peaked.

While CORM-3 is clearly not stable in saline, it appears to be considerably more stable than in phosphate buffered systems; CORM-3 incubated in isotonic saline solution (150 mM) was still able to release around 30 % of the maximum yield of CO after 30 min incubation. In contrast, in 30 mM KPi buffer the yield of CO obtained from CORM-3 after 5 min incubation decreases by almost 90% with respect to the control. This clearly points to either substitution by phosphate or pH effects as the most important pathway of CORM-3 deactivation in biological media.

#### 4.3.5 Does CORM-3 Release CO in Bacterial and Mammalian Media?

While the Ru(II) based CORM-2 and CORM-3 have demonstrable antimicrobial activity, these complexes have been far more extensively employed for *in vitro* mammalian studies where complex media are commonly employed.<sup>105,109–114</sup> Given the worrying instability of CORM-3 towards CO release in a comparatively simple buffer system and saline, it seemed pertinent to test the stability of CORM-3 towards

CO release in the types of media used for mammalian studies. RPMI-1640 and DMEM were used as typical mammalian cell culturing media. These complex media contain a large number of amino acids with R groups which can potential bind to the Ru CORM, displacing other ligands. Since our collaborators were also interested in the impact on bacterial growth medium composition on antimicrobial activity, CO release from CORM-3 in two complex bacterial media, MH2 and LB, and a defined minimal salts medium was also explored. All four types of complex media tested are strongly coloured, making colourimetric and fluorescence-based assays of CO release difficult.

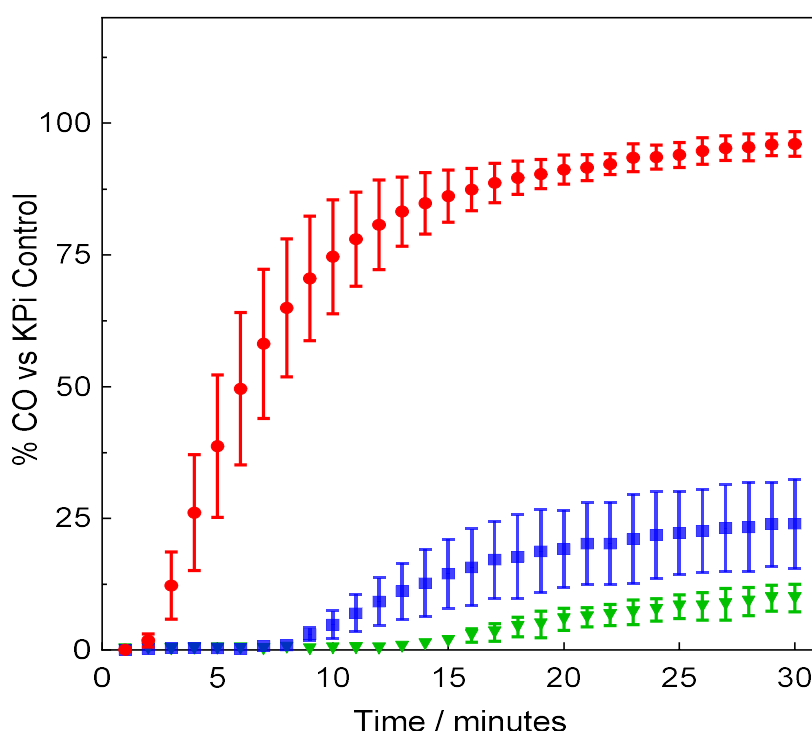


**Figure 4.8** – CO release from dithionite treated CORM-3 (100  $\mu$ M) in defined minimal salts medium with no preincubation (red circles) and after 5 (blue squares) and 10 minute (green triangles) preincubation in media. Error bars represent standard deviation (1  $\sigma$ ) of two replicates.

To test how effective a CO releasing agent is in media, 100  $\mu$ M CORM-3 was incubated in each of the five media types for 0, 5 and 10 min before addition of two equivalents of dithionite to trigger CO release while the accumulation of CO in the headspace was monitored by FTIR spectroscopy. Figure 4.8 shows the CO release behaviour of CORM-3 in glucose supplemented defined minimal salts medium. As with KPi buffer, CORM-3 is rapidly deactivated towards dithionite triggered CO

release during incubation in buffer. Complex bacterial media showed a similar trend (Figures 4.9 and 4.10) with CORM-3 becoming rapidly deactivated towards dithionite triggered CO release with an increasingly lower yield of CO with longer incubation times. However, unlike defined media and KPi, CO levels generated from dithionite-treated CORM-3 in complex media do not actually plateau within the 30 minute timeframe of the experiment.

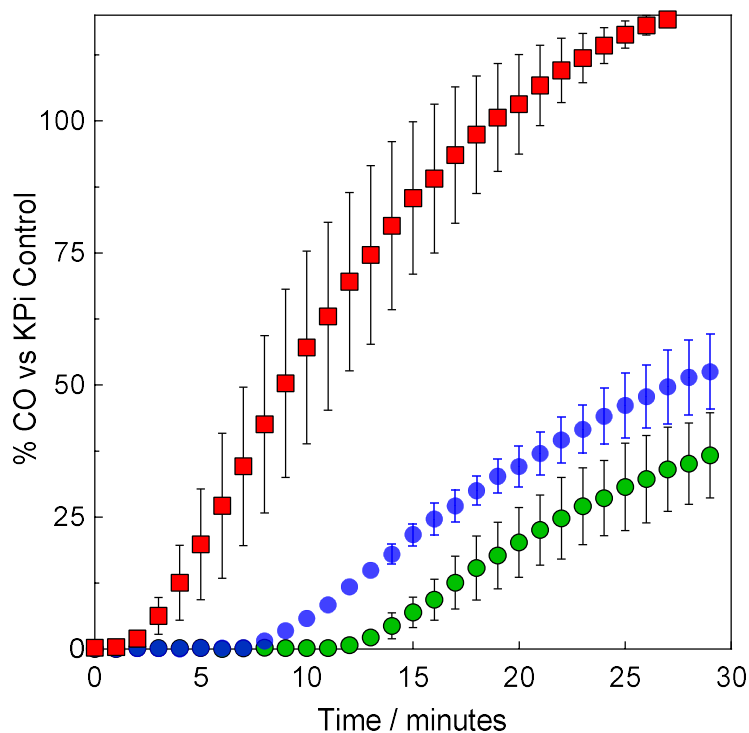


**Figure 4.9** – CO release from dithionite treated CORM-3 (100  $\mu$ M) in LB medium with no preincubation (red squares) and after 5 (blue circles) and 10 minute (green circles) preincubation in media. Error bars represent standard deviation ( $1 \sigma$ ) of two replicates.

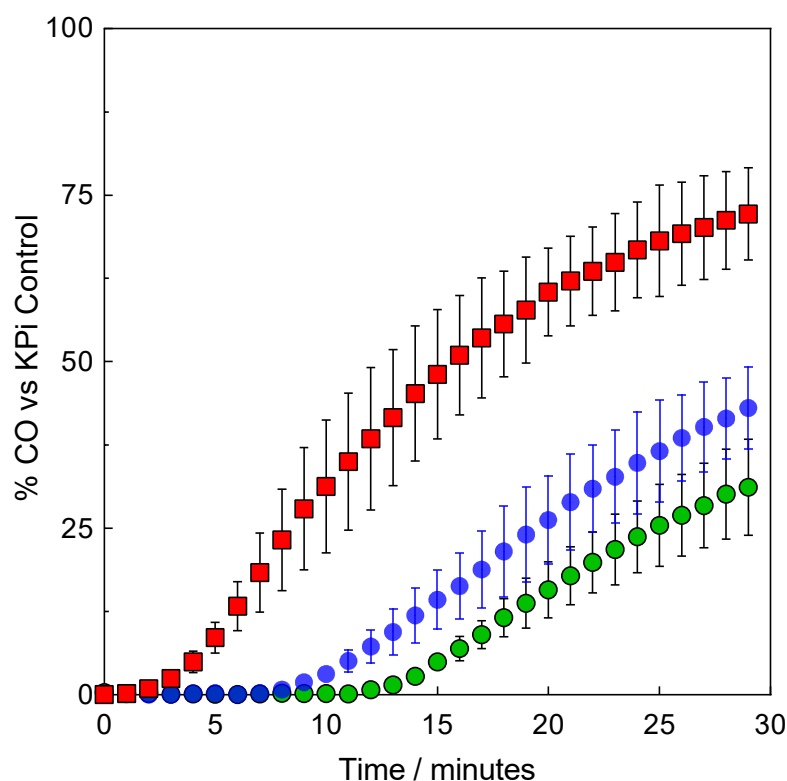


**Figure 4.10** – CO release from dithionite treated CORM-3 (100  $\mu\text{M}$ ) in MH2 medium with no preincubation (red squares) and after 5 (blue circles) and 10 minute (green circles) preincubation in media. Error bars represent standard deviation ( $1 \sigma$ ) of two replicates.

Again, a similar deactivation was observed in both complex mammalian media tested (Figures 4.11), although the deactivation effect was somewhat less pronounced. In DMEM, the baseline CO yield from CORM-3 with no incubation is considerably lower (around 50 %) than the other media types tested here, although the reduction in CO yield with extend incubation was not as pronounced as with other media. In all media tested, no CO release was observed before dithionite addition, indicating that there are no species present in solution which can elicit rapid CO release. Another feature which is noticeable is the delay between addition of dithionite and the appearance of CO. While this may simply reflect mixing and diffusion in the solution phase, it should be noted that dithionite itself slowly decomposes in aqueous solution to give various species such as sulfite ( $\text{SO}_3^{2-}$ ) and  $\text{SO}_2^{\bullet-}$ .<sup>115</sup> While sodium dithionite was employed in this study to better simulate the conditions of the Mb assay, use of a better defined triggering agent such as sodium sulfite may be more appropriate for future work on this compound.

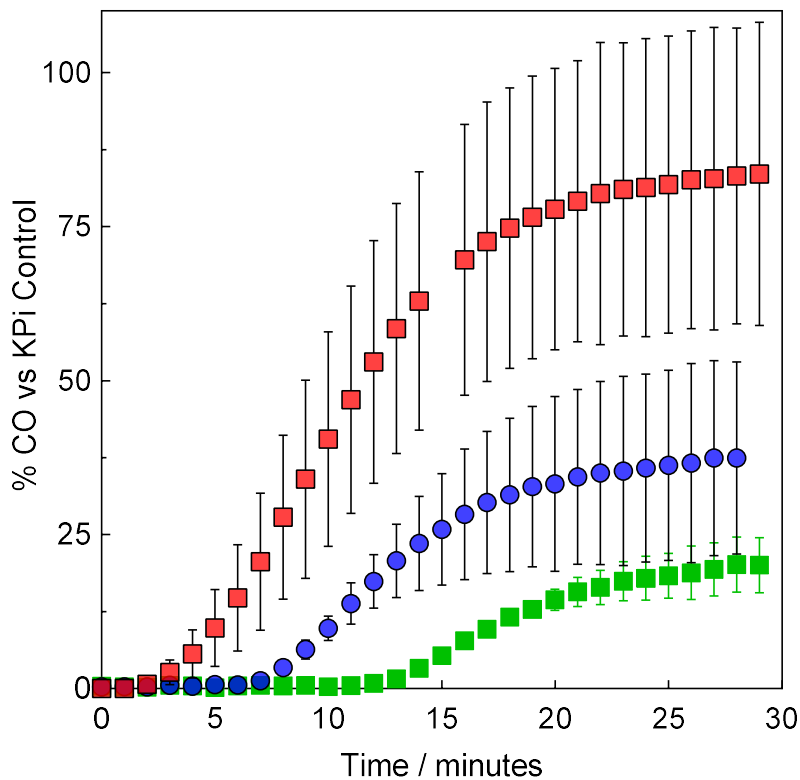
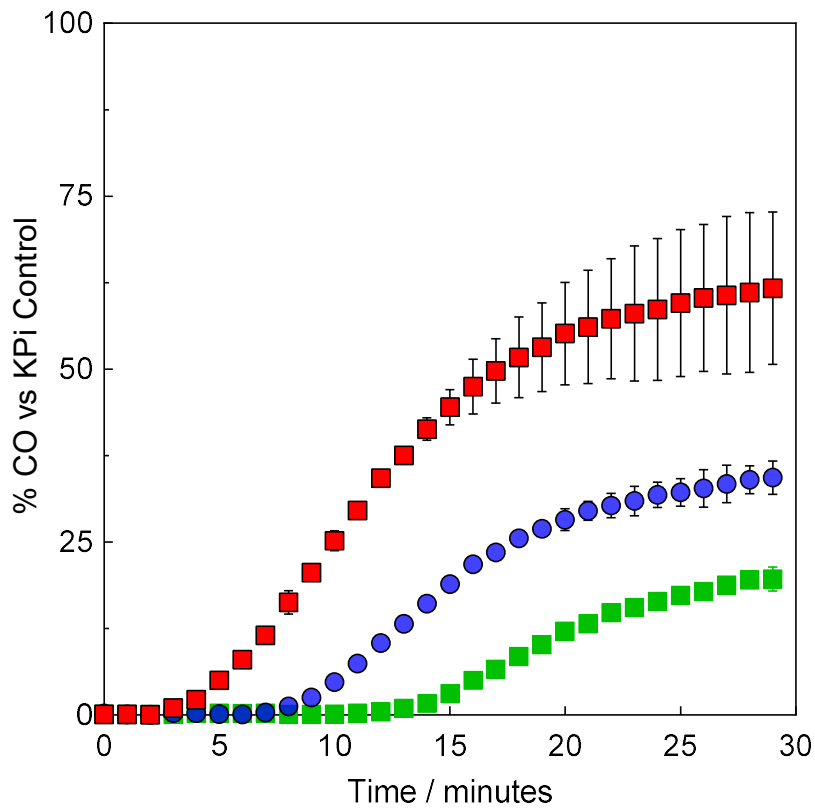


**Figure 4.11** – CO release from dithionite treated CORM-3 (100  $\mu$ M) in DMEM (top) and RPMI-1640 (bottom) medium with no preincubation (red squares) and after 5 (blue circles) and 10 minute (green squares) preincubation in media. Error bars represent standard deviation ( $1 \sigma$ ) of two replicates.

#### 4.3.6 CORM-3 is a PhotoCORM

Users of the CORM-2 and 3 typically try to minimise exposure of stock solutions to light and the synthesis of CORM-3 calls for the exclusion of light by wrapping the reaction vessel in foil, suggesting these molecules have at least some photochemistry. The appearance of a paper describing the release of more than one equivalent of CO from CORM-2 using 254 nm illumination prompted an investigation into the response of CORM-3 to UV light.<sup>116</sup>

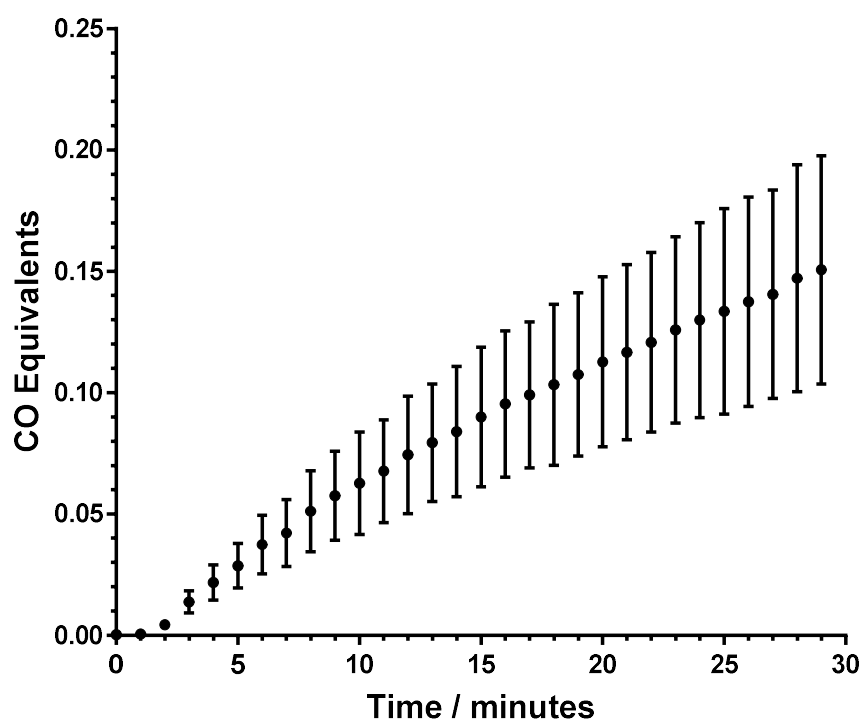


**Figure 4.12** – Kinetic plot showing photolytic CO release from CORM-3 (100  $\mu\text{M}$ ) in 30 mM KPi buffer upon illumination at 365 nm with a 6 W transilluminator lamp. Points represent average of two experimental replicates. Error bars represent standard deviation ( $1 \sigma$ ) of two replicates.

To test this hypothesis that CORM-3 may in fact release CO upon illumination, samples of CORM-3 (100  $\mu\text{M}$ ) were prepared as before and placed in KPi buffer before being illuminated at 365 nm using a 6 W transilluminator lamp while FTIR spectra were recorded at 1 minute intervals. Within 3 min of switching the lamp on, CO gas was observed in the IR spectra, clearing indicating that CO can be liberated from CORM-3 via a photochemical mechanism in a similar manner to CORM-2. CO accumulation continued throughout the 30 minute period for which the lamp remained on, yielding around 0.15 equivalents of CO to the headspace. Although the rate of

photolytic CO liberation is much lower than when CO release is triggered by addition of dithionite or sulfite, the fact that CO was still being liberated even after 30 min suggests that the mechanism by which photochemical CO release occurs may not be inhibited by the mechanisms which inhibit sulfite-triggered CO release.

#### 4.4 Conclusions & Future Work

Headspace FTIR spectroscopy has proven to be a valuable tool for measuring CO release from CORM-3 in a manner which is free from interference from media components. Unlike solution phase FTIR studies, which are plagued by the strong and broad absorption bands of water, in the gas phase CO and water lines remain reasonably well separated and allow for conclusive identification of CO even in the presence of large quantities of water vapour. The results reported here are consistent with the conclusions of McClean *et al.*, namely that CO release from CORM-3 is triggered by sodium dithionite and other sulfite species but not by cysteine (and presumably other related thiols), despite considerable evidence that cysteine residues may be a target for CORM-3 complexation *in vivo*.<sup>107</sup>

CORM-3 is rapidly deactivated in phosphate buffered systems to give an inactive complex which is unable to release CO upon addition of a sulfite source. While chloride alone leads to deactivation of the complex, deactivation occurs more slowly than in phosphate buffered systems, indicating that pH effects or phosphate coordination to the complex dominate. The loss of CO releasing ability is not due to loss of CO to the environment; instead it occurs either through the formation of a stable tricarbonyl complex by coordination of phosphate or other ligands and / or through the conversion of one or more coordinated CO ligands to metalcarboxylic acid groups. This may or may not undergo further decomposition via water-gas shift chemistry to release CO<sub>2</sub>. Attempts to detect CO<sub>2</sub> in the headspace of solutions of CORM-3 in phosphate buffer proved inconclusive due to the very strong background levels of CO<sub>2</sub> in the environment and the unfavourable pH equilibrium in solution which favours bicarbonate rather than CO<sub>2</sub> close to neutral pH. In future work, <sup>13</sup>CO labelled CORM-3 could be used as the IR absorption bands of <sup>13</sup>CO<sub>2</sub> are slightly redshifted from the major isotopomer, making identification of CO<sub>2</sub> arising from water-gas shift chemistry considerably easier.

On complex bacterial and mammalian media, CORM-3 was found to quickly lose its ability to release CO, although this occurred much less rapidly than in phosphate buffer. No CO release was observed from CORM-3 incubated in complex media. Intense UV illumination of the complex was found to release CO, indicating that an additional photolytic mechanism for CO release is also present. Taken together, these results strongly suggest that suitability of CORM-3 for biological studies should be seriously reassessed as the Mb assay is in no way indicative of the true CO releasing behaviour of this compound.

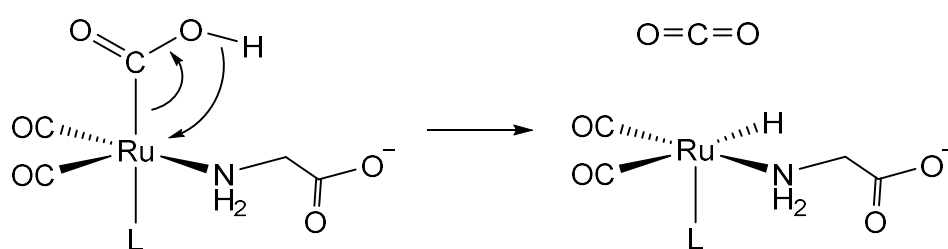


**Figure 4.13** – Reverse water-gas shift reaction (RWGS) may be one route of CORM-3 deactivation close to neutral pH. A vacant coordination site is required for formation of concerted formation of a metal hydride and ejection of CO<sub>2</sub>. Since dissociation of the glycine carboxylate is reported to be facile, this may be a possible site of hydride attack.

Disentangling the relative importance of phosphate coordination and pH effects could prove to be challenging, but moving to another buffer system could allow the effects of pH to be treated independently of phosphate. While Good's buffers might give a better system for exploring the aqueous chemistry of CORM-3, careful selection would be required to avoid using a buffer with good cation coordinating abilities (e.g. tris(hydroxymethyl)aminomethane, Tris) as this would almost certainly lead to additional unwanted chemistry. As the complex mammalian media tested are carbonate / bicarbonate buffered, it might also be pertinent to test the stability of CORM-3 in a simple carbonate / bicarbonate buffered system, particularly since CORM-3 appears to be deactivated less rapidly in such systems.



# Chapter 5 - Application of Cavity Enhanced Raman Spectroscopy to Biohydrogen Detection

## Abstract

This chapter details the demonstration of a novel gas-phase Raman technique, Cavity Enhanced Raman Spectroscopy (CERS), and its application to the detection of hydrogen generated by a model 'biohydrogen' generating processes utilising the mixed acid fermentation pathways of *E. coli*. No H<sub>2</sub> was generated when O<sub>2</sub> was not removed from the system or when cells were incubated on rich media alone. Thorough removal of air and addition of a suitable carbon source (either glucose or glycerol), *E. coli* could be suitably stimulated to generate large quantities of H<sub>2</sub> and CO<sub>2</sub>, with both glucose and glycerol giving similar yields of H<sub>2</sub> weighted by number of formate equivalents per molecule. After reaching a plateau, H<sub>2</sub> was observed to decrease faster than the leak out rate, consistent with H<sub>2</sub> consumption by the cells. Addition of D<sub>2</sub> allowed the consumption / isotope exchange process to be followed simultaneously with H<sub>2</sub> production. Under D<sub>2</sub> / N<sub>2</sub>, H<sub>2</sub> yields were observed to increase significantly reflecting either direct isotope exchange of H<sub>2</sub> to D<sub>2</sub> or D<sub>2</sub> competition with H<sub>2</sub> for hydrogen consuming processes. Under CO / D<sub>2</sub> / N<sub>2</sub>, production of H<sub>2</sub> was completely inhibited while D<sub>2</sub> consumption was significantly reduced, indicating that *E. coli* Hydrogenase 1 (Hyd-1) plays only a minor role in isotope exchange / hydrogen uptake under fermentative conditions

The work described in this chapter forms part of a scientific publication (ref. <sup>117</sup>);

*Cavity-Enhanced Raman Spectroscopy in the Biosciences: In Situ, Multicomponent, and Isotope Selective Gas Measurements to Study Hydrogen Production and Consumption by Escherichia coli*

Thomas W. Smith and Michael Hippler, Analytical Chemistry, 2017, **89**, 2147 - 2154.

DOI:10.1021/acs.analchem.6b04924

## 5.1 Introduction

### 5.1.1 Hydrogenases and Biological Hydrogen Metabolism

There is currently a great deal of concern about dwindling reserves of fossil fuels and the impact of their use on the climate. Considerable amounts of funding are being channelled into research into how to best protect these reserves and the development of new, sustainable technologies. The use of molecular hydrogen ( $H_2$ ) as a fuel gas for use in electrochemical cells is being seriously considered as a replacement power source for vehicles.<sup>118</sup> While efficient  $H_2$  storage remains a considerable technological problem, the sustainable production of hydrogen must also be addressed.<sup>119–122</sup> Currently, the major commercial source of  $H_2$  supplies is reforming of natural gas, an energy intensive endothermic process which requires high temperatures and pressures and releases considerable quantities of  $CO_2$ .

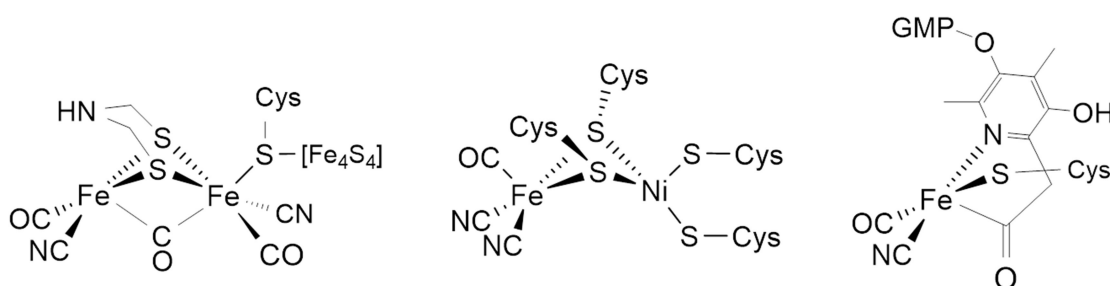


**Figure 5.1** – Active site structures of the three classes of hydrogenase (from left to right) [FeFe], [NiFe] and mononuclear Fe hydrogenases. All three forms feature CO and CN directly bound to a Fe centre. GMP – guanosine monophosphate, Cys – cysteine residue.

Biologically derived  $H_2$  or “biohydrogen” is a particularly promising future source of the gas.<sup>123–125</sup> Microorganisms have already developed the tools necessary to generate and consume  $H_2$  at ambient temperatures and pressures in an aqueous environment using a class of metalloenzymes known as hydrogenases.<sup>126</sup> Hydrogenases are widespread through several kingdoms of life, including bacteria, fungi and unicellular algae, possibly reflecting the importance of  $H_2$  early in the history of life on the planet and its continuing importance in many anaerobic and microaerobic environments. Hydrogenases broadly fall into three classes based on their catalytic site, bimetallic [FeFe] and [NiFe] hydrogenases and a mononuclear Fe hydrogenase which appears to be unique to algae (see Figure 5.1). All three classes

show differing degrees of O<sub>2</sub> sensitivity and activity, with members of the [FeFe] class showing some of the highest turnover rates but also the highest O<sub>2</sub> sensitivities. [NiFe] hydrogenases are typically somewhat more resistant to O<sub>2</sub> but with lower activities. All three classes share the Fe(CO)(CN)<sub>n</sub> chemical motif in their active site, making hydrogenases one of the few examples of a naturally occurring organometallic active site in biology. The ability of these enzymes to access H<sub>2</sub> oxidation / H<sup>+</sup> reduction without the need for expensive noble metals or extreme conditions makes them interesting to study, both for designing new biomimetic catalysts based on cheaper first row transition metals and as novel catalysts in their own right.

Many microorganisms, when cultured under the correct conditions, can be net producers of H<sub>2</sub>. While efficient photosynthetic H<sub>2</sub> production from water by green algae has been the goal of a great deal of research, there still exist numerous engineering and (bio)chemical challenges which need to be overcome. Photosynthetic algae such as *Chlamydomonas reinhardtii*, the best studied organism in terms of photosynthetic biohydrogen production, can generate H<sub>2</sub> under certain circumstances.<sup>127,128</sup> A major challenge is ensuring that O<sub>2</sub>, usually the major product of photosynthesis, is reduced to levels which do not inactivate the hydrogenases associated with photosynthetic H<sub>2</sub> production. A number of genetic and chemical methods have been demonstrated which can remove or reduce O<sub>2</sub> formation, but this often comes at the cost of sustainable growth.<sup>127,129</sup> Photofermentative H<sub>2</sub> production from organic acids by purple non-sulfur (PNS) bacteria is another pathway which is easier to achieve without sacrificing growth.<sup>130</sup> Both light driven pathways to biohydrogen require illumination for efficient H<sub>2</sub> production, a condition which becomes increasingly challenging upon scaling up to the large industrial fermenters which would be required for large scale biohydrogen production. Apart from the light dependent pathways, many non-photosynthetic strict and facultative anaerobic bacteria generate H<sub>2</sub> as a by-product of dark fermentation on organic substrates.<sup>131</sup> While not as efficient at generating H<sub>2</sub> as many strict anaerobes, *E. coli* is able to generate H<sub>2</sub> and CO<sub>2</sub> from formate during anaerobic mixed acid fermentation. The ease of genetic modification and extensive understanding of its biochemistry and physiology make *E. coli* a particularly attractive organism for studying H<sub>2</sub> metabolism and as a basis for construction of H<sub>2</sub> overproducing strains through genetic modification.

*E. coli* has four native hydrogenases, all of the [NiFe] class, termed Hyd-1, Hyd-2, Hyd-3 and Hyd-4.<sup>132</sup> Expression of *E. coli* hydrogenases is repressed by both O<sub>2</sub> and nitrate. While all four hydrogenases are membrane-bound multisubunit metalloenzymes which share a common active site, there is considerable variation in subunit composition, oxygen sensitivity, localisation (either on the inner or outer face of the inner membrane) and the typical direction of catalysis *in vivo* (either for proton reduction or H<sub>2</sub> oxidation). All four hydrogenases share a large subunit which houses the bimetallic [NiFe] cluster and a small subunit containing redox active [Fe<sub>4</sub>S<sub>4</sub>] clusters which mediate electron transfer to and / or from the active site. Each hydrogenase also has at least one additional subunit which binds directly to the membrane. Hyd-1 and 2 appear to primarily act as H<sub>2</sub> oxidising enzymes and are situated on the outer face of the cytoplasmic membrane while Hyd-3 and Hyd-4 are situated on the inner cytoplasmic face of the membrane and primarily catalyse the reduction of protons to H<sub>2</sub>. Hyd-1 (encoded for by the *hya* operon) is structurally the simplest of the four hydrogenases and the only one for which a crystal structure of the complete enzyme has ever been obtained. *In vivo*, the enzyme is composed of a two HyaAHyaB heterodimers (a ‘dimer or dimers’) and a third membrane-associated HyaC subunit. HyaC contains a cytochrome binding pocket which may play a role in electron transfer. While Hyd-1 is only expressed under fermentative conditions, it is highly resistant to O<sub>2</sub> inhibition. Indeed, expression of Hyd-1 is linked to a high affinity cytochrome *bd* oxidase which has been suggested to play a role in the transition from anaerobic to aerobic conditions. Hyd-1 may play a similar role by utilising H<sub>2</sub> generated during fermentation to reduce O<sub>2</sub> (the Knallgas reaction), helping to cushion the cells against a sudden transition from aerobic to anaerobic conditions.

Hyd-2 (encoded by the *hyb* operon) is far more O<sub>2</sub> sensitive than Hyd-1 and appears to function primarily as a H<sub>2</sub> oxidising enzyme under fermentative conditions. While energy recovery during fermentation is normally thought of as occurring only through substrate level phosphorylation and not through respiratory chains and generation of a proton gradient, Hyd-2 appears to actively pump protons across the membrane and forms a respiratory chain with fumarate reductase which can utilise both exogenous and endogenous fumarate (generated during mixed acid fermentation) as a terminal electron acceptor. When *E. coli* is grown anaerobically on glycerol / LB rather than a glucose / fumarate mixture, Hyd-2 appears to switch activities, acting as

a H<sub>2</sub> producing enzyme. This activity requires a proton gradient across the inner membrane; Pinske *et al.* showed that addition of carbonyl cyanide chlorophenyl hydrazine (CCCP), a protonophore which dissipates the proton gradient by shuttling protons across the inner membrane, immediately stopped H<sub>2</sub> production from an *E. coli* mutant lacking all other hydrogenases.<sup>133</sup> This H<sub>2</sub> production activity has been suggested to act as a sort of 'relief valve', removing excess reducing equivalents from the quinone pool during growth on glycerol, a highly reduced carbon source.

Hyd-3 is a very large multisubunit enzyme which, together with formate dehydrogenase H (FDH-H), forms the formate hydrogenlyase complex (FHL). FHL is situated on the cytoplasmic side of the inner membrane and is the primary source of H<sub>2</sub> and CO<sub>2</sub> during *E. coli* mixed acid fermentation. FDH-H catalyses the oxidation of formate, generated from pyruvate by pyruvate formate-lyase (PFL), to CO<sub>2</sub> when the pH drops below a critical threshold. Initially, formate generated by PFL activity is exported from the cytoplasm by formate channel FocA to prevent accumulation. During anaerobic respiration, Formate dehydrogenase N (FDH-N) can catalyse oxidation to CO<sub>2</sub> and transfer electrons via the quinone pool to a suitable terminal reductase (e.g. nitrate reductase when nitrate is present). In the absence of suitable endogenous electron acceptor, however, formate simply accumulates in the periplasm and extracellular space leading to a considerable drop in pH. At a critical pH value, the directionality of FocA shifts and the channel begins to reimport formate into the cytoplasm where it can be oxidised by FHL with concurrent proton reduction. In this way, FHL acts to counteract acidification of the intra- and extracellular environment. Despite FHL activity being known since *E. coli* fermentation was first studied over 100 years ago, the complex has remained difficult to study outside of intact cells until relatively recently due to the ease with which the complex can break apart. McDowall *et al.* reported the first isolation of intact FHL allowing for direct characterisation of the subunit structure of the complex and electrochemical measurements.<sup>134</sup>

The *E. coli* genome encodes a fourth hydrogenase, Hyd-4 (encoded by the *hyf* operon), which shows considerable sequence similarity with Hyd-3.<sup>135</sup> Early studies based on sensitive immunoassays only detected Hyd-1, 2 and 3, leading to the suggestion that Hyd-4 might only be expressed under certain conditions or that the operon may in fact be completely silent. Hyd-4 is believed to form a complex

analogous to FHL with a formate dehydrogenase. This complex is often referred to as FHL-2. The precise physiological role (if any) of Hyd-4 remains obscure.

### **5.1.2 Aims**

This chapter describes the application a novel form of Raman spectroscopy, Cavity Enhanced Raman Spectroscopy (CERS), to the detection of H<sub>2</sub> generated by *E. coli*. Using D<sub>2</sub> labelling of the headspace in protonated media, hydrogen uptake and hydrogen production by the bacteria can be distinguished. In addition, the impact of additional CO, a competitive inhibitor of a number of hydrogenases, is explored.

## **5.2 Experimental**

### **5.2.1 Cavity Enhanced Raman Spectroscopy with Optical Feedback**

The original CW-CERS-OF setup is described in greater detail in the group's previous publications.<sup>30,136</sup> A schematic overview of the setup used for the work described in this chapter is shown in Figure 5.2 and described below. The system is based on optical locking of a low power diode laser (Hitachi HL6322G, 15 mW, 636 nm, **LD**) to an optical cavity formed from two high performance concave mirrors (**SM & PSM**, Newport SuperMirrors<sup>TM</sup>, 583 – 633 nm, R > 0.9998, 1 m radius of curvature, 1 inch diameter,  $l = 35$  cm mirror separation) which also acts as a power build-up cavity for enhanced Raman scattering from gaseous samples between the mirrors.

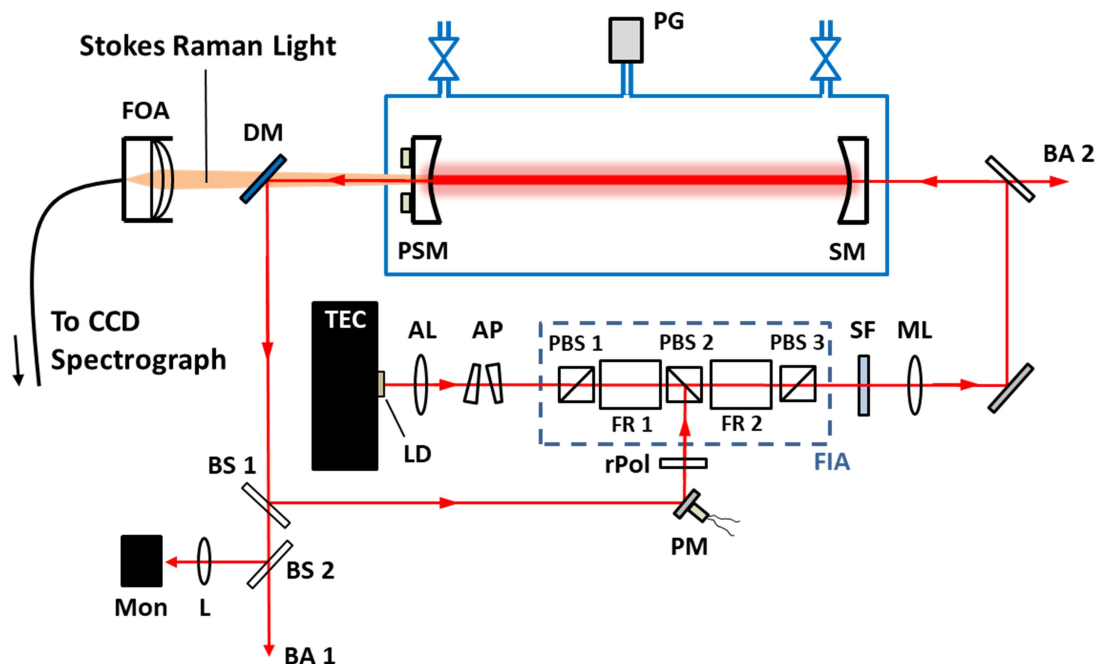


**Figure 5.2** – CERS experimental setup used for the majority of experiments described in this chapter. **TEC** – thermoelectric cooled mount, **LD** – laser diode, **AL** – aspheric lens, **AP** – anamorphic prism pair, **FIA** – Faraday isolator assembly, **PBS** – polarising beam splitter, **FR** – Faraday rotator, **SF** – short-pass filter, **ML** – mode matching lens, **BA** – beam alignment points, **SM** – super-mirror, **PSM** – piezo-mounted super-mirror, **DM** – dichroic mirror, **FOA** – fiber optic assembly, **BS** – glass wedge beam splitter, **L** – lens, **Mon** – monitor photodiode, **PM** – piezo-mounted mirror, **rPol** – rotating polarizer, **PG** – pressure monitor. Briefly, laser emission from **LD** is coupled into a high finesse optical cavity composed of two high reflectivity mirrors. Power build up within the cavity is sufficient to generate detectable Raman signals with samples held at ambient pressures down to mixing ratios of ca. 1 %. Exiting Raman (Stokes) light is separated from Rayleigh light by a sharp cut-off dichroic mirror **DM**. Optical isolators (**FIA**) prevent the direct back reflection from the cavity damaging or destabilising the emission wavelength and enable light exiting the cavity through the rear mirror (**PSM**) to be fed back to **LD** in a controlled manner, locking the emission wavelength to the cavity.

To ensure stable operation, the diode package is mounted on a temperature stabilised mount (Thorlabs TCLDM9; controlled by Thorlabs ITC102) rotated to match the linearly polarised laser emission to the Faraday isolator assembly **FIA** (see below). The diode laser emission is collimated by aspheric lens **AL** (Thorlabs C140TME-B, 600 – 1050 nm AR coating,  $f = 1.45$  mm, 0.55 NA) and circularised by anamorphic prism pair **AP** (Thorlabs PS870) to ensure that the laser emission is efficiently coupled into a single Gaussian spatial mode ( $TEM_{00}$ ) of the cavity (Figure 5.3).

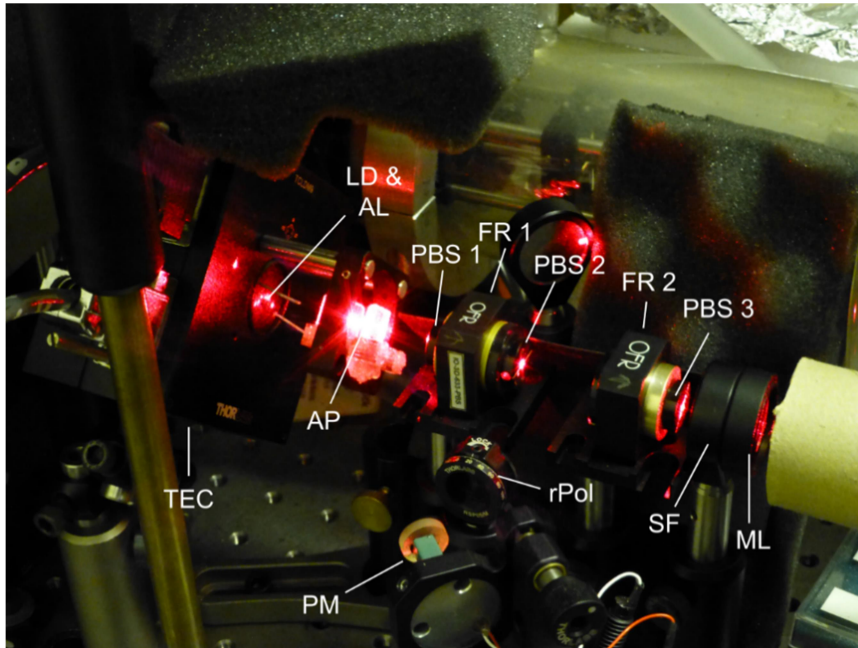


**Figure 5.3** – Laser diode head and front end optics of the CERS setup. **TEC** – thermoelectric cooled mount, **LD** – laser diode, **AL** – aspheric lens, **AP** – anamorphic prism pair, **PBS** – polarising beam splitter, **FR** – Faraday rotator, **SF** – short-pass filter, **ML** – mode matching lens, **PM** – piezo-mounted mirror, **rPol** – rotating polarizer.

The linear design of the cavity necessitates that the ingoing beam must strike normal to the rear face of **SM**, leading to a direct back reflection which returns along the incoming beam path, which could severely destabilise the laser emission or even damage the laser diode. Faraday isolator assembly **FIA**, located after the initial focusing optics, prevents this potentially damaging feedback from returning to the laser diode. **FIA** consists of two separate Faraday isolators arranged in series (OFR, IO-3D-633-PBS, 30–36 dB isolation each at 633 nm), each of which consists of a Faraday rotator (**FR**) and polarising beam splitters (**PBS**) which transmit the outgoing light but reject the direct back reflected light.

After exiting the **FIA**, the laser output passes through two more transmissive optics; a mode matching lens (**ML**,  $f = 100$  mm), which is used to focus the beam to ensure efficient coupling into the cavity, and a shortpass filter (**SF**, Thorlabs FES0650, 650 nm cut-off) which acts as a clean-up filter for the laser, removing spurious weak emission bands to longer wavelengths which would otherwise contaminate the redshifted (Stokes) Raman bands. A pair of 1 inch mirrors are used to couple the incoming laser light into the optical cavity (Figure 5.4). The second mirror is a dielectric mirror which is not perfectly reflective; part of the returning laser light

from the cavity can pass through the mirror and is projected onto an alignment card approximately 1.5 m away (**BA 2**) for coarse alignment and visual inspection of the laser beam profile.

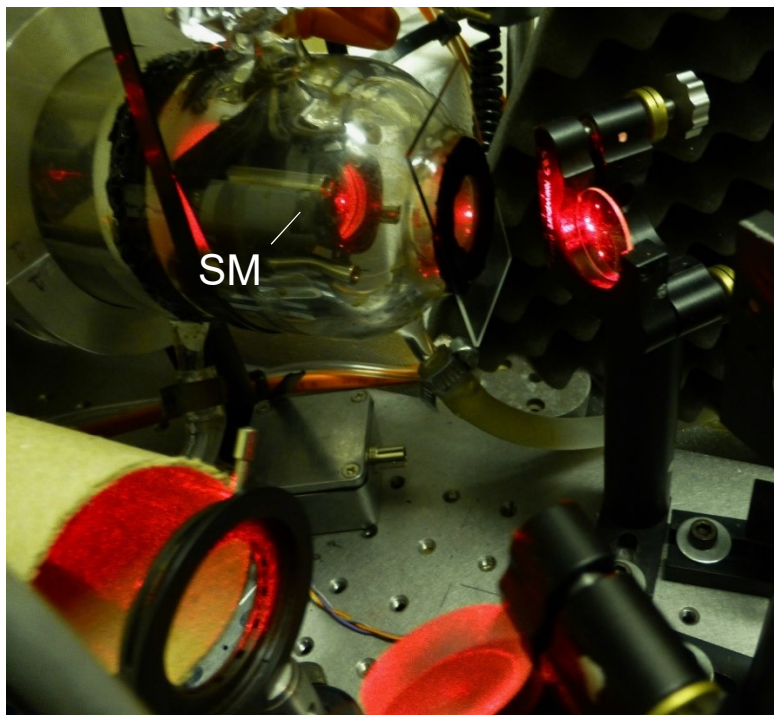


**Figure 5.4** – Laser emission being injected into the CERS enclosure. Scattered light from optical power build up within the cavity can be clearly seen through SuperMirror™ **SM** and scattering off the Teflon retaining ring inside the glass enclosure.

The optical cavity is enclosed within a custom gas tight glass enclosure (Figure 5.4) equipped with a 1000 mbar diaphragm gauge (**PG**, Edwards model D35735000), several ground glass Quickfit® connectors and Youngs-style taps which allow controlled filling of the enclosure with defined gas mixtures. The cell is connected to a rotary vacuum pump for operation at reduced pressure or to remove air or other gases from samples *in situ*. A built-in water jacket allows the system to be heated in order to prevent condensation on the windows and internal optics. Optical grade glass windows (BK7, 0.5 mm thickness, 20 mm clear aperture) are used for the entrance and exit beam paths. **SM** and **PSM** are held in place using a rigid optical cage system (Thorlabs) which is mounted onto the glass surface through custom Teflon mounting rings which sit securely in the glass enclosure. **PSM** is mounted on piezo actuators to allow active mode matching of the cavity to the laser wavelength, although this

function was not used in the measurements described in this chapter. When the laser wavelength matches the resonance conditions of the cavity, optical power build up by around 800 times occurs within the cavity, sufficient to generate detectable levels of Raman scattered light from dilute gaseous samples down to mixing ratios of a few ppmv.<sup>30</sup>

Raman scattered light is collected in the 0° linear scattering geometry (i.e. from the rear face of **PSM**). Light exiting from mirror **PSM** includes both non-scattered excitation light, elastically scattered Rayleigh light and inelastically scattered Raman light. A sharp cut-off dichroic beamsplitter **DB** (Semrock RazorEdge LPD01-633RS-25) is used to separate the red-shifted Stokes Raman light from the excitation and Rayleigh scattered light. Remaining excitation light exiting the cavity is rerouted by **DB** to the laser diode via a glass wedge beam splitter **BS 1**, piezo mounted mirror **PM** for injection locking of the diode via **PBS 2**. Rotating polariser **rPol** placed between **PM** and **PBS 2** can be used to reduce or even completely block feedback to the laser diode to prevent damage or overdriving the laser, although this particular laser diode was found to operate well with full feedback (i.e. with the polariser removed). **BS 2** splits the light between monitor photodiode **Mon** (Thorlabs PDA015A), which allow quantitative measurements of the strength and stability of cavity resonances, and a second beam alignment point (**BA 2**) necessary for alignment of the feedback beam. Stokes shifted Raman light passing through dichroic mirror **DM** is coupled by optical assembly **FOA** (convex 1 inch diameter,  $f = 25.4$  mm lens) into a multimode optical fiber (Ocean Optics QP-200-2-UV/BX, 200  $\mu\text{m}$  core,  $l = 2$  m). The fiber output is transmitted to a CCD-equipped spectrograph via two achromatic doublets (**AD 1** and **AD 2**). A long pass filter **LF** (Semrock) is placed between the two achromatic lenses to block the majority of any remaining excitation and Rayleigh scattered light transmitted by the fiber. The spectrograph (Shamrock 750-A Czerny-Turner spectrograph,  $f = 750$  mm, 120  $\mu\text{m}$  slit width; Andor iVac DR324B-FI CCD camera cooled to  $-60$  °C) is equipped with a high (1200 lines / mm blazed at 750 nm), medium (600 lines / mm blazed at 500 nm) and low resolution grating (150 lines / mm blazed at 750 nm) mounted on a rotating turret. The majority of the measurements described in this chapter were measured using the lowest resolution grating which, when combined with the CCD camera, covers Raman shifts of between approximately 500  $\text{cm}^{-1}$  and 4500  $\text{cm}^{-1}$  for 636 nm excitation, sufficient to capture the fundamental Raman transitions of most small gaseous molecules in a single acquisition.

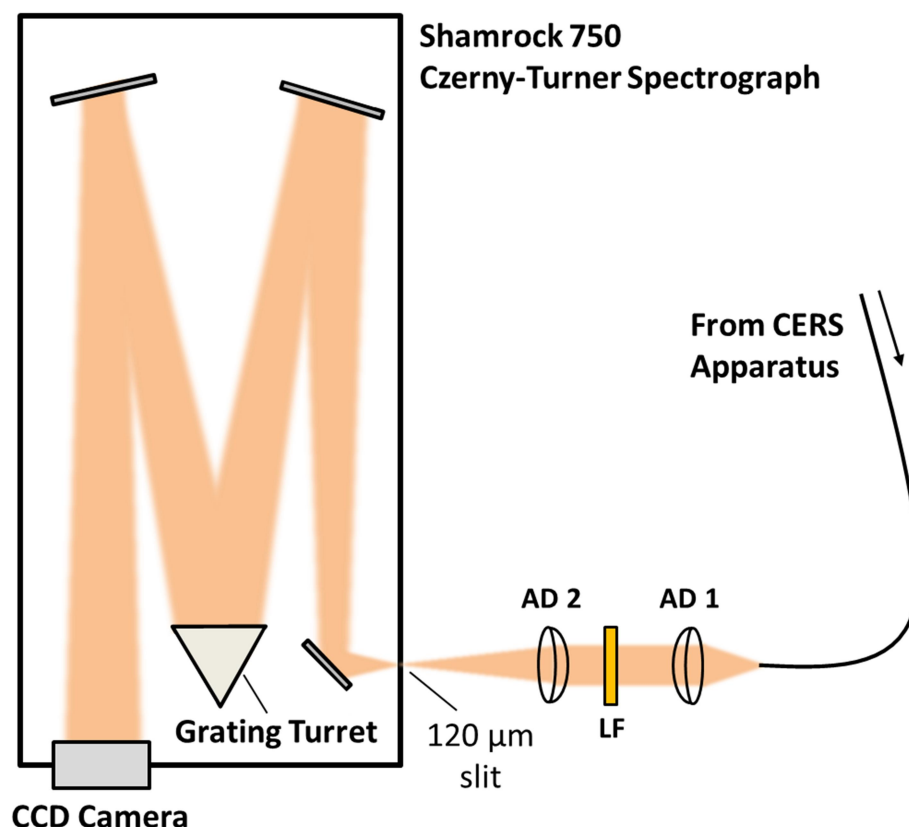


**Figure 5.5** – Shamrock 750 Czerny-Turner spectrograph used for CERS measurements. Two coupling achromatic doublets (**AD 1** and **AD 2**) are used to match the output of the multimode fiber to the slit of the spectrograph. Long-pass filter **LF** is used to clean up the input light, removing any residual laser light which might overwhelm the sensitive camera.

It was found that this particular laser diode effectively self-locks when provided with sufficient optical feedback from the cavity (i.e. when the polariser rPol was completely removed from the feedback path), meaning that electronic mode tracking was no longer required to maintain stable resonances. Although cavity resonances are considerably less regular, the resulting fluctuations in Raman intensity affect all bands equally so that signals can be normalised through use of a suitable internal standard. In this case, signals were effectively normalised using the  $\text{N}_2$   $Q$ -branch ( $2329\text{ cm}^{-1}$ ) assuming that the amount of  $\text{N}_2$  present in the system remains constant. In addition to  $\text{N}_2$ , other relevant gaseous analytes which have been observed include  $\text{O}_2$  ( $1556\text{ cm}^{-1}$ ),  $\text{CO}_2$  ( $1285\text{ cm}^{-1}$  and  $1388\text{ cm}^{-1}$ ), water ( $3653\text{ cm}^{-1}$ ),  $\text{D}_2$  ( $2987\text{ cm}^{-1}$ ),  $\text{H}_2$  ( $4155\text{ cm}^{-1}$ ),  $\text{HD}$  ( $3628\text{ cm}^{-1}$ ) and  $\text{CO}$  ( $2142\text{ cm}^{-1}$ ). At a 30 s exposure time, a noise-equivalent detection limit of around 1 mbar  $\text{H}_2$  can be achieved using the low-resolution grating.

### 5.2.2 Media and Conditions for Routine Growth of Bacteria

LB broth, LB agar, nutrient agar (Oxoid), glycerol (Fisher) and glassware were sterilised by autoclaving at 121 °C prior to use. Glucose (Sigma-Aldrich) solutions were sterilised by vacuum filtration in a 0.22 µm Stericup<sup>®</sup> (Millipore). LB agar or nutrient agar plates were streaked with material from a 50:50 LB / glycerol stock of *E. coli* K-12 MG1655 and incubated overnight at 37 °C. After the appearance of isolated colonies, the plates were wrapped in Parafilm and placed in the fridge at 5 °C. Plates were kept for no more than six weeks before being replaced.

The day before a planned experiment, a 50 mL capacity centrifuge tube was completely filled with sterile LB and inoculated with a single isolated colony from the agar plate. The tube was then sealed and placed in an orbital incubator (200 rpm, 37 °C, 16 hours). Overnight growth of the cells was confirmed by the appearance of a highly turbid suspension after the overnight growth giving an OD<sub>600</sub> ~ 1 on the instrument employed (Jenway 7310 spectrophotometer, 1 cm path length, 5 fold dilution in sterile LB).

## 5.2.4 CERS Hydrogen Metabolism Measurements

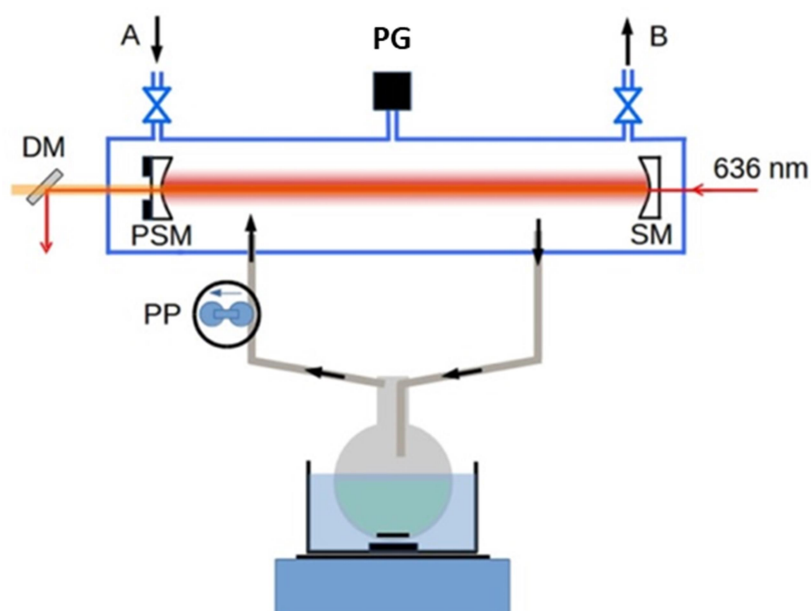


**Figure 5.6** – Schematic of the experimental setup employed for CERS biohydrogen measurements. Figure taken from Smith *et al.*<sup>117</sup>

For biological CERS measurements, the overnight suspension was added to 200 mL of sterile LB supplemented with either D-glucose (40, 80 or 100 mM) or glycerol (80 or 200 mM) in a sterilised 250 mL long neck flask round bottom flask equipped with a 3 cm magnetic stirrer. The flask was finally sealed to prevent contamination and reduce aeration before being placed in ice and transported to the CERS apparatus. After transport, the 500 mL flask containing the cell suspension was removed from ice and placed in a 37 °C water bath. The flask was connected to the CERS enclosure by means of a custom made Quickfit<sup>®</sup> adaptor with two capillaries designed to fit 3 mm internal diameter tubing. Two lengths of tubing (polyethylene, 3 mm internal diameter) fitted to these capillaries were used to form a circuit between the CERS enclosure and the flask. A peristaltic pump (nominal flow rate 7 L h<sup>-1</sup>) was used to enforce gas circulation through the system while vigorous stirring was employed to keep the solution and headspace at equilibrium. After connecting the flask to the CERS enclosure, the system was repeatedly evacuated and flushed with N<sub>2</sub> until O<sub>2</sub> could no longer be detected in CERS spectra of the headspace. The system was then filled to just below 1 bar total pressure with N<sub>2</sub> or a mixture of N<sub>2</sub> / D<sub>2</sub> or N<sub>2</sub> / D<sub>2</sub> / CO using Tedlar<sup>®</sup> sample bags. The total filling pressure was checked using the

diaphragm pressure monitor **PG**. After the purge step, the gas composition of the headspace was monitored for up to 2 weeks by CERS. Throughout the measurement, the CERS enclosure was maintained at 40 – 45 °C to prevent condensation on the windows and high performance mirrors. Throughout each CERS experiment, vigorous stirring of the medium and continual cycling of the headspace was used to keep the entire system at equilibrium. CERS spectra were recorded at approximately 1 hour intervals for the first six hours and then at least twice a day for the remaining for the measurement period.

## 5.3 Results & Discussion

### 5.3.1 H<sub>2</sub> Production from Anaerobic Batch Cultures with Glucose

In the absence of external electron acceptors, *E. coli* uses mixed acid fermentation to derive energy from organic substrates; the precise distribution of end products is governed by the cell's need to generate ATP and recycle NAD<sup>+</sup>.<sup>137</sup> Most reports on dark fermentation as a route for H<sub>2</sub> production focus on the use of pure saccharides as substrates, particularly glucose. As the initial aim of this work was simply to characterise CERS as a tool to study hydrogen metabolism, it seemed sensible to start with glucose as the carbon source. Although *E. coli* is not a fastidious organism with respect to its growth requirements, growth is much faster on complex media such as LB. Given that a complex medium would probably be the only economical medium in a large scale process, LB supplemented with glucose (40 or 100 mM) was employed for preliminary measurements. During the preparation and transport of the biohydrogen broth culture to the CERS apparatus, there was necessarily some exposure to air, meaning that it was necessary to purge the system through repeated evacuation and N<sub>2</sub> flushing steps. Since CERS is sensitive to all molecular gases, the system can be easily checked for traces of O<sub>2</sub>. Typically, between three and five purge / N<sub>2</sub> flush cycles were employed to remove any dissolved O<sub>2</sub>.

Figure 5.7 shows kinetic traces for CO<sub>2</sub> and H<sub>2</sub> in a culture supplemented with 40 mM glucose; this behaviour is typical of glucose supplemented cultures. As expected, under anaerobic conditions and in the absence of any terminal electron acceptors which might support anaerobic respiratory chains, *E. coli* generates H<sub>2</sub> and CO<sub>2</sub> from formate degradation by FHL. Initially, the appearance of H<sub>2</sub> is rather slow, but it is

distinguishable in Raman spectra even within the first hour. After the first few hours, the rate of  $H_2$  production increases sharply with  $pH_2$  peaking at around 140 mbar (7.1 mmol in solution and headspace). Since each molecule of glucose can potentially be converted into two molecules of formate and therefore two molecules of  $H_2$ , the maximum theoretical yield of  $H_2$  would be 20 mmol, giving this process a yield of 36 %. It should be remembered that in wild type bacteria, other competing pathways are present which funnel the carbon into other fermentation products such as lactic acid. The  $pCO_2$  mirrors  $pH_2$ , peaking at around 120 mbar which corresponds to around 6.9 mmol assuming that low pH ( $< 5$ ) is achieved by the end of the fermentation. The ratio of  $CO_2/H_2$  at its peak is 97 %, which is consistent with the vast majority of  $H_2$  and  $CO_2$  originating from FHL activity.

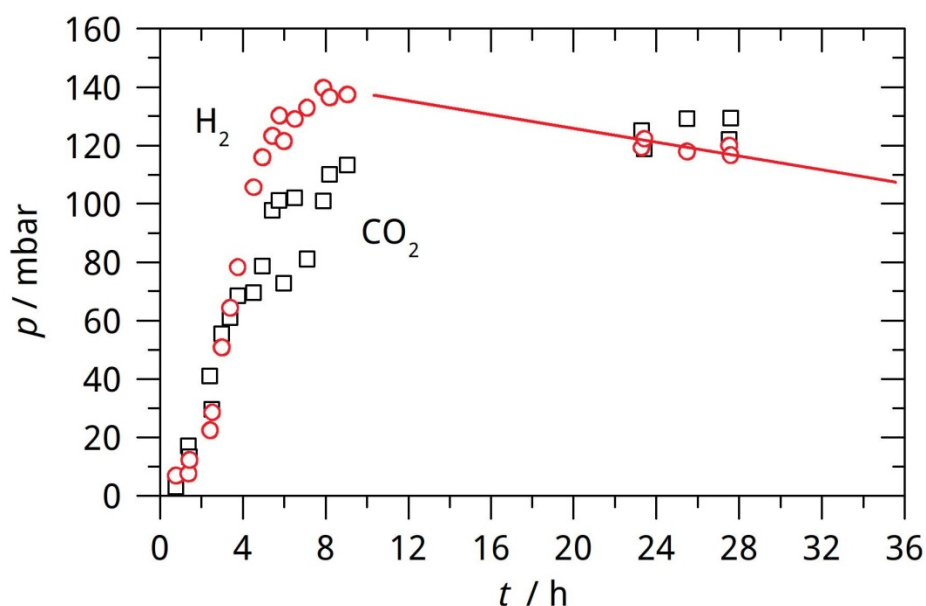


**Figure 5.7** - Kinetic plot showing the variation in partial pressures of  $CO_2$  (black squares) and  $H_2$  (blue circles) as a function of time after purge step as measured by CERS in a typical anaerobic experiment (40 mM glucose / LB). Data points depict a single representative measurement.<sup>117</sup>

Unlike  $CO_2$  which appears to reach a plateau,  $H_2$  begins to decay immediately after reaching the peak value with an extrapolated half-life of 3 - 4 days. Similar behaviour was observed when cultures were supplemented with 100 mM glucose, although  $CO_2$  formed a slightly lower proportion of the evolved gas with a lower  $CO_2 / H_2$  ratio (see Figure 5.8). If the directionality of Hyd-2 is purely governed by the

redox state of the quinone pool, then employing very high glucose concentrations may force Hyd-2 to run in reverse. As Hyd-2 H<sub>2</sub> production does not require simultaneous oxidation of formate, this activity might explain the somewhat lower CO<sub>2</sub> yield observed in these experiments. For both glucose concentrations, after peaking, H<sub>2</sub> was observed to decay while CO<sub>2</sub> remained essentially constant, indicating that H<sub>2</sub> oxidation by Hyd-1 / Hyd-2 occurs simultaneously with formate-coupled proton reduction by the FHL complex. As might be expected, mutant strains of *E. coli* lacking these uptake hydrogenases generate considerably more H<sub>2</sub>.<sup>138,139</sup> While Hyd-3 has also been reported to operate in reverse, coupling H<sub>2</sub> oxidation to CO<sub>2</sub> reduction to formate, recent work has shown that this behaviour is probably not relevant under physiological conditions (although reverse Hyd-3 activity may have applications in CO<sub>2</sub> fixation technology).<sup>140,141</sup> In addition, the absence of any observable CO<sub>2</sub> uptake in the CERS measurements indicates that the H<sub>2</sub> uptake activity observed in these measurements is due to hydrogenases which are not directly coupled to formate dehydrogenase.

Feedstock	H <sub>2</sub> peak		H <sub>2</sub> yield	H <sub>2</sub> peak at	H <sub>2</sub> t <sub>1/2</sub> growth	H <sub>2</sub> t <sub>1/2</sub> decay	CO <sub>2</sub> peak	
	mbar	mmol					mbar	mmol
40 mM D-glucose	140 mbar	7.1 mmol	0.71	0.3 d	1 h	3.4 d	120 mbar	6.9 mmol
100 mM D-glucose	363 mbar	18.5 mmol	0.74	1.2 d	2.9 h	-	200 mbar	11.5 mmol
100 mM D-glucose	330 mbar	16.8 mmol	0.67	1 d	3.1 h	7.5 d	150 mbar	8.6 mmol

**Figure 5.8** – Partial pressures of CO<sub>2</sub> and H<sub>2</sub> generated from anaerobic glucose / LB fermentation broth. Note the yields are expressed as mol H<sub>2</sub> / mol glucose, meaning that 100 % conversion to H<sub>2</sub> would be equivalent to a yield of 2.

### 5.3.2 H<sub>2</sub> Production from Anaerobic Batch Cultures with Glycerol

The transesterification stage of biodiesel production generates considerable quantities of glycerol-contaminated aqueous waste.<sup>142</sup> This waste could be a convenient, sustainable substrate for organisms such as *E. coli* which can utilize glycerol for fermentation under certain conditions.<sup>143,144</sup> Due to its higher degree of reduction, glycerol fermentation typically gives increased yields of more reduced products which

are typically more valuable for the chemical industry.<sup>145</sup> To investigate H<sub>2</sub> production from glycerol, anaerobic *E. coli* LB broth cultures supplemented with glycerol (80 or 200 mM) were prepared. As with glucose supplemented cultures, *E. coli* grown anaerobically on glycerol / LB generate H<sub>2</sub>, although considerably slower than for glucose supplemented cultures.

Figure 5.9 shows a typical example of the evolution of CO<sub>2</sub> and H<sub>2</sub> from a culture supplemented with 200 mM glycerol over 5 days. The appearance of H<sub>2</sub> is described by exponential growth with half time  $t_{1/2} = 23$  h and an apparent delay of around 6 hours (red curve in Figure 5.8). After reaching its peak at 360 mbar, the H<sub>2</sub> partial pressure shows a slow exponential decay with half time  $t_{1/2} = 6.8$  d (green curve in Fig. 4). The CO<sub>2</sub> pressure broadly mirrors H<sub>2</sub> production, but at 155 mbar, it peaks at a considerably lower value. The lower CO<sub>2</sub>/H<sub>2</sub> ratio probably reflects the fact that significant amounts of H<sub>2</sub> are produced by Hyd-2 which is not coupled to formate oxidation by FDH-H. This is in agreement with previous work which has shown that Hyd-2 plays also a role in H<sub>2</sub> production during glycerol fermentation where it acts as a ‘relief valve’ to prevent over-reduction of the quinone pool.<sup>138</sup> After day 4, a noticeable decrease in H<sub>2</sub> is observed, presumably reflecting H<sub>2</sub> uptake by the bacteria.

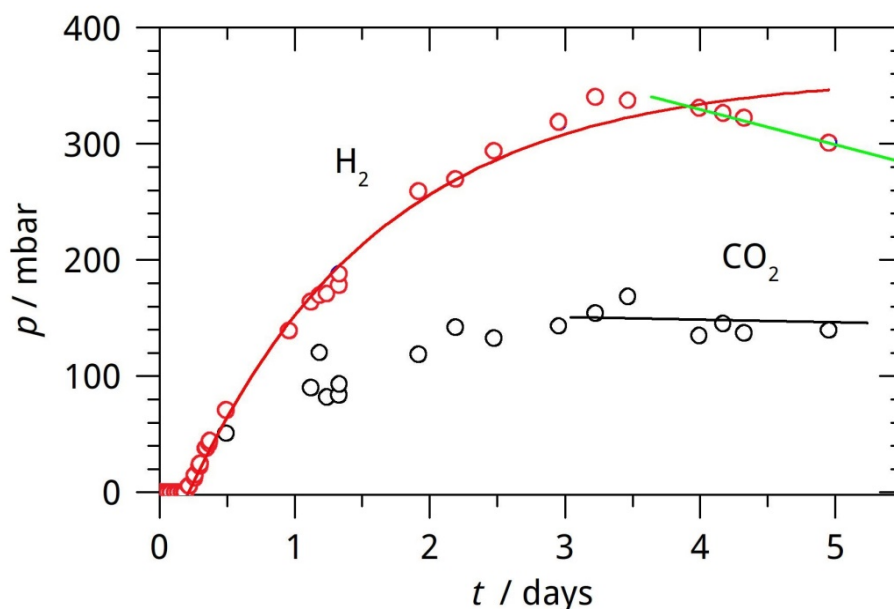


**Figure 5.9** – Partial pressures of CO<sub>2</sub> (black circles) and H<sub>2</sub> (blue circles) as a function of time as observed by CERS the anaerobic fermentation of 200 mM glycerol by *E. coli*. Data points depict a single representative measurement. Data points depict a single representative measurement.<sup>117</sup>

Different kinetic behavior is observed for H<sub>2</sub> production depending on the carbon source and its concentration; with 40 mM *D*-glucose it has a half time of 1 hours, tripling to 3 hours for 100 mM. H<sub>2</sub> production from glycerol is much slower, with a half time of 8 hours for 80 mM glycerol, increasing to 23 h for 200 mM. For glucose, the theoretical maximum fermentation yield (mol H<sub>2</sub> / mol glucose) is 2, since up to two formate molecules can be generated from each molecule of glucose. For glycerol, the corresponding maximum yield is 1. Taking this into account, the observed H<sub>2</sub> yields (expressed as a percentage of the theoretical yield) are within 27-37% of the theoretical maximum yield from each carbon source, regardless of the carbon source. This yield could be improved by continually extraction of H<sub>2</sub>, preventing accumulation and uptake of H<sub>2</sub>. Previous work has shown that allowing H<sub>2</sub> build up above glycerol supplemented cultures is detrimental to growth, which would suggest that constantly siphoning off H<sub>2</sub> as it is generated could be critical for efficient biohydrogen production.<sup>146</sup>

Feedstock	H <sub>2</sub> peak		H <sub>2</sub> yield	H <sub>2</sub> peak at	H <sub>2</sub> t <sub>1/2</sub> growth	H <sub>2</sub> t <sub>1/2</sub> decay	CO <sub>2</sub> peak	
	Pressure (mbar)	Yield (mmol)					Pressure (mbar)	Yield (mmol)
80 mM glycerol	105 mbar	5.4 mmol	0.27	1.5 d	8 h	1.4 d	40 mbar	2.3 mmol
200 mM glycerol	360 mbar	18.4 mmol	0.37	3.3 d	23 h	6.8 d	155 mbar	8.9 mmol

**Figure 5.10** – Partial pressures of CO<sub>2</sub> and H<sub>2</sub> generated from anaerobic glucose / LB fermentation broth. Note the yields are expressed as mol H<sub>2</sub> / mol glycerol, meaning that 100 % conversion to H<sub>2</sub> would be equivalent to a yield of 1.

### 5.3.3 Mixed Acid Fermentation under a D<sub>2</sub> / N<sub>2</sub> Atmosphere

To separate hydrogen generation and consumption, isotopic labelling with of the headspace with deuterium can be employed (see Figure 5.11). D<sub>2</sub> labelling has previously been employed in combination with membrane inlet mass spectrometry to investigate hydrogenases, but an additional correction function is required to account for the constant siphoning off of D<sub>2</sub>.<sup>147</sup> Raman spectroscopic techniques have isotopomer selectivity but does not consume any gas. In order to follow hydrogen uptake by *E. coli*, a large excess of D<sub>2</sub> was introduced at the beginning of the measurement. Batch cultures of *E. coli* were prepared and purged as before to remove

any dissolved O<sub>2</sub>. A defined mixture of N<sub>2</sub>/D<sub>2</sub> was then introduced into the system to a total pressure of 1 bar (typically 600 mbar D<sub>2</sub>, 400 mbar N<sub>2</sub>). Figure 5.11 shows a typical Raman spectrum acquired 5 days into an experiment above a glycerol / LB culture.

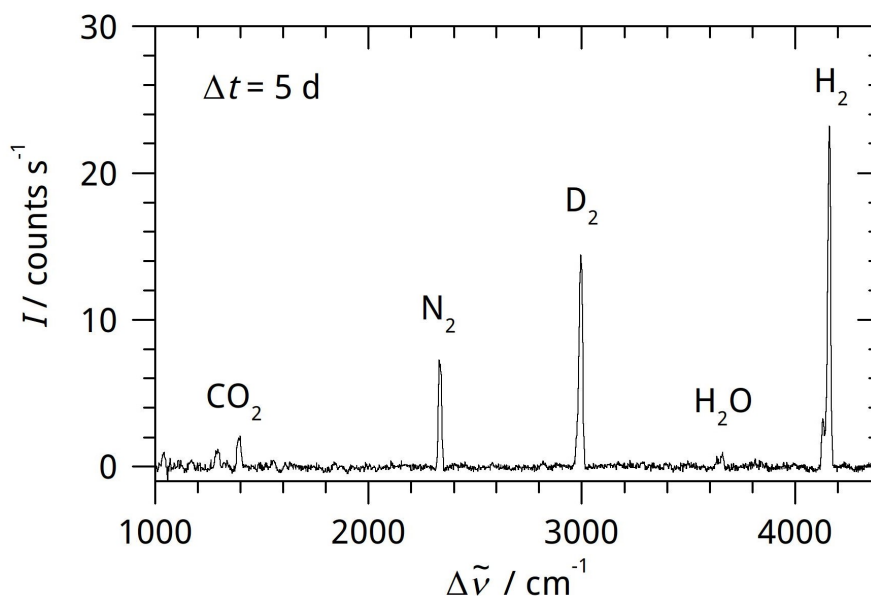


**Figure 5.11** - CERS Raman spectrum of the culture headspace after 5 days in a typical anaerobic experiment with 98 mM glycerol under D<sub>2</sub>/N<sub>2</sub>.<sup>117</sup>

Figure 5.12 shows the kinetic traces of H<sub>2</sub>, D<sub>2</sub> and CO<sub>2</sub> in a typical experiment with 40 mM glucose. Hydrogen is known to inhibit certain classes of hydrogenase, there appears to be no delay in the appearance or reduction in the rate of H<sub>2</sub> formation. In addition, no lag in D<sub>2</sub> consumption is observed, indicating that the hydrogenase(s) associated with D<sub>2</sub> consumption are already present at the beginning of the measurement. With 40 mM glucose (10 mmol), there are two distinct phases of D<sub>2</sub> consumption which both adopt first-order behaviour. Phase a), which lasts between 0 to 0.5 days ( $t_{1/2} = 1.4$  d) and phase b) which continues for the rest of the measurement ( $t_{1/2} = 5.0 - 5.5$  d). No distinct transition in either H<sub>2</sub> or CO<sub>2</sub> is observed at the transition between phases a) and b) in D<sub>2</sub> uptake.

After 7 days, about 350 mbar (17.9 mmol) D<sub>2</sub> has been consumed and an additional 10 mmol more H<sub>2</sub> generated than would be expected from fermentation alone based on the CO<sub>2</sub> yield. This excess corresponds to around 56 % of the consumed D<sub>2</sub>, which is likely converted to H<sub>2</sub> through isotope exchange with solvent. D<sub>2</sub> appears to be

coupled either directly (through H/D exchange at a hydrogenase active site) or indirectly (perhaps *via* intermediate electron donation back into the quinone pool) to proton reduction. Such D/H isotope exchange has been well reported in the literature but, rather unusually for such experiments, there is relatively little of the mixed isotopomer HD (typically final  $p_{HD} < 15$  mbar).<sup>147</sup> A similar absence of HD has previously been observed for purified hydrogenases obtained from *Azotobacter vinelandii* and *Ralstonia eutropha* (now *Cupriavidus necator*) when incubated under  $D_2$  in protonated buffer.<sup>148,149</sup>

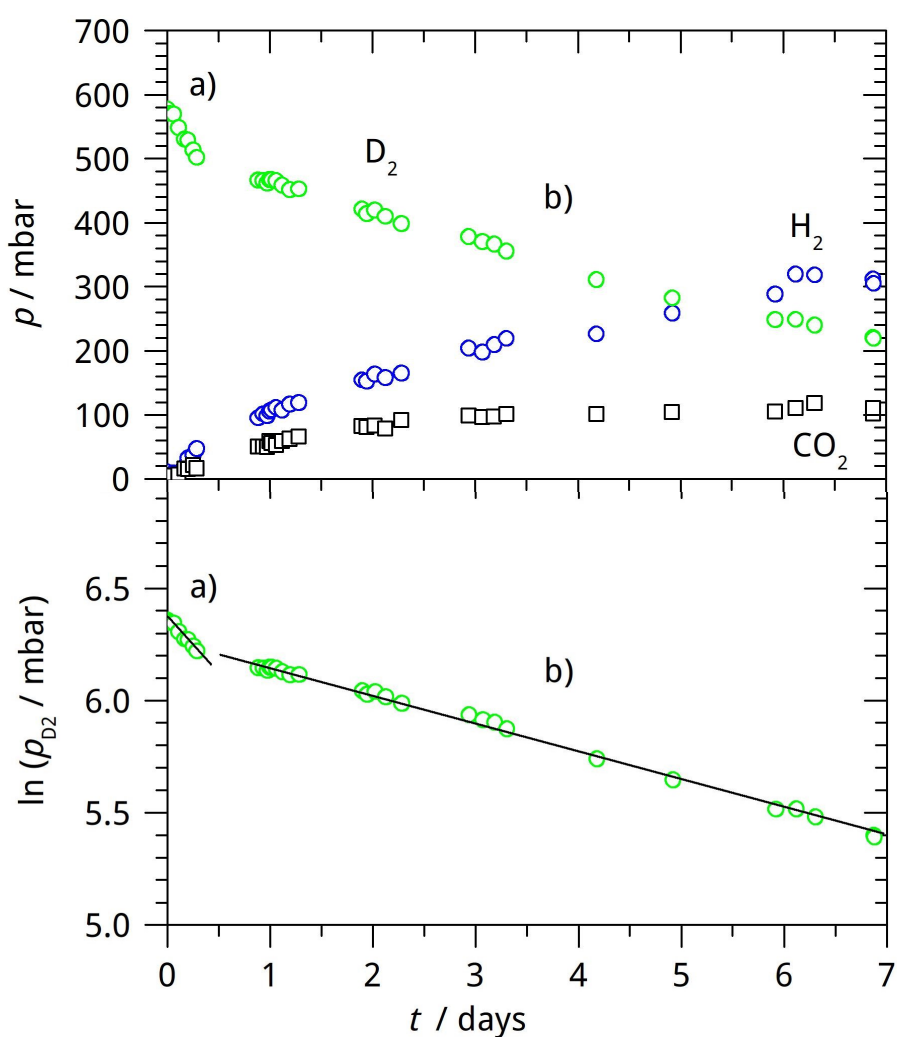


**Figure 5.12** - Kinetic plot showing the variation in partial pressures of  $H_2$ ,  $D_2$  and  $CO_2$  in a typical  $D_2$  labelling experiment (in this case 40 mM glucose under  $D_2 / N_2$ ). The lower plot displays the decay of  $D_2$  on a logarithmic scale, showing two distinct pseudo-first order kinetic regimes. Data points depict a single representative measurement.

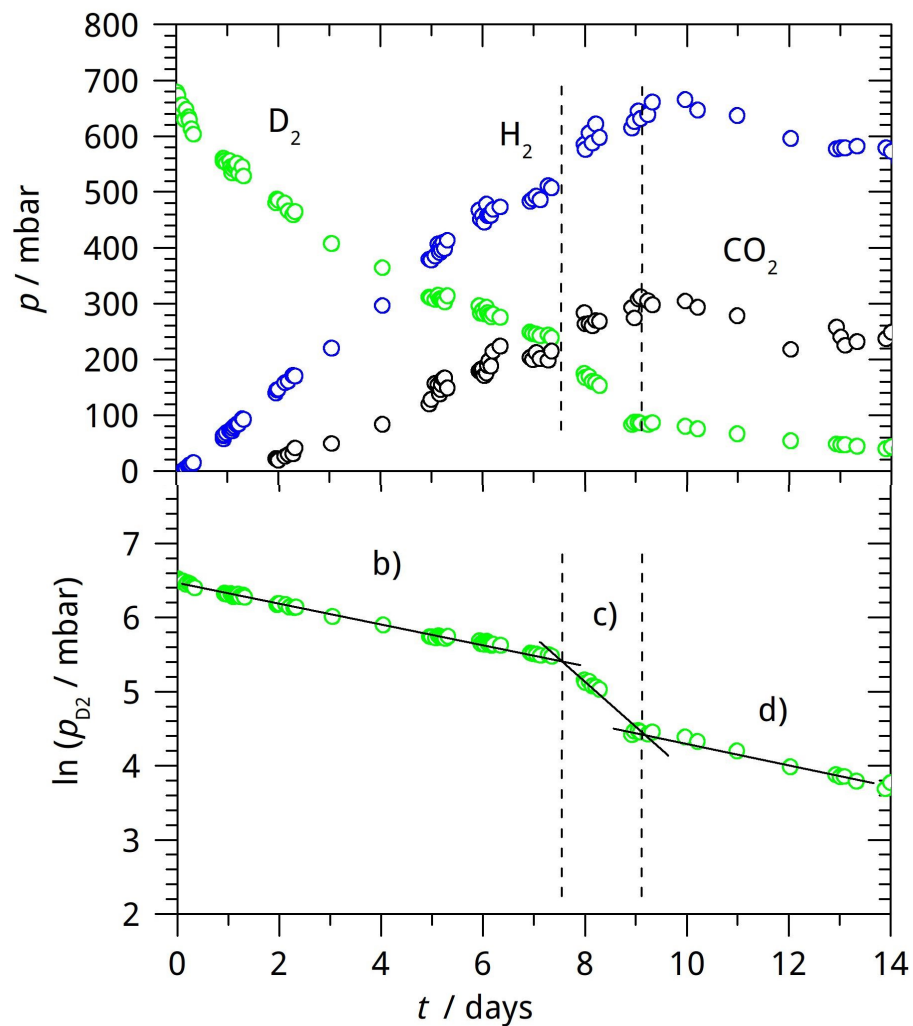


**Figure 5.13** - Kinetic plot showing the variation in partial pressures of  $H_2$ ,  $D_2$  and  $CO_2$  in a typical  $D_2$  labelling experiment (in this case 98 mM glycerol under  $D_2 / N_2$ ). The lower plot displays the decay of  $D_2$  on a logarithmic scale, showing three pseudo-first order kinetic regimes. Data points depict a single representative measurement. In all three replicate experiments, phase c) was observed between 7 and 10 days.

Figure 5.13 shows a typical  $D_2$  labelling experiment above glycerol. Samples showed only one phase of  $D_2$  decay up until day 7-8 characterized by a decay with  $t_{1/2} = 5.0 - 5.7$  days, which is very similar to phase b) in glucose supplemented samples. Half way through the experiment, a sudden surge in  $D_2$  uptake is observed, with an exponential decay with  $t_{1/2} = 0.8 - 1.5$  d. This surge is accompanied by a significant jump in both  $CO_2$  and  $H_2$ . After this event,  $D_2$  decay resumes at close to the original rate of consumption. The precise cause of this even remains unclear and clearly requires further investigation, although it could coincide with a large influx of formate

into the cytoplasm. While all effort was made to exclude external contamination, sudden growth of another hydrogen metabolising organism could also explain the rapid CO<sub>2</sub> production and rapid D<sub>2</sub> / H<sub>2</sub> turnover.

### 5.3.3 CO Inhibition of *E. coli* Hydrogenases

CO is a potent inhibitor of many hydrogenases. *E. coli* Hyd-1 is comparatively resistant to CO inhibition whereas the O<sub>2</sub> sensitive *E. coli* Hyd-2 and 3 are strongly inhibited by CO.<sup>134,150–152</sup> In an attempt to tie down the source of D<sub>2</sub> isotope exchange / uptake, CO was introduced into the headspace along with N<sub>2</sub> and D<sub>2</sub> during the purge step (20 % CO, 40 % D<sub>2</sub>, 40 % N<sub>2</sub>, see Figure 5.14). After leaving the culture under the same CO/D<sub>2</sub>/N<sub>2</sub> atmosphere for a day, the system was purged with N<sub>2</sub> and an N<sub>2</sub>/D<sub>2</sub> atmosphere was re-introduced into the system. The headspace composition was then monitored by CERS for an additional nine days.

As shown in Figure 5.14, the presence of CO in the headspace completely inhibited formation of H<sub>2</sub> and CO<sub>2</sub> and largely inhibited D<sub>2</sub> uptake. Since Hyd-1 is the only hydrogenase in *E. coli* known to have some level of CO tolerance, the minimal D<sub>2</sub> uptake activity and negligible CO<sub>2</sub> and H<sub>2</sub> formation suggests that Hyd-1 does not play a major role in the isotope exchange / hydrogen uptake observed in earlier experiments. The half-life for D<sub>2</sub> of 13.6 days during when CO is present is considerably longer than in the measurements where CO was not introduced into the headspace. This supports the hypothesis that Hyd-2 and Hyd-3, which are strongly inhibited under a CO atmosphere, are more important than Hyd-1 under fermentative conditions.

A partial recovery of H<sub>2</sub> production and D<sub>2</sub> isotope exchange / consumption activity is observed when CO is removed. Recovery is not instantaneous, with a delay of around 0.5 days before the onset of D<sub>2</sub> oxidation and 1 day before H<sub>2</sub> production. This may reflect growth of new cells rather than recovery of cells present during the CO inhibition phase. Again, HD is only formed to a minor extent. This is the first demonstration of selective CO inhibition of hydrogenases in *E. coli* whole cells.

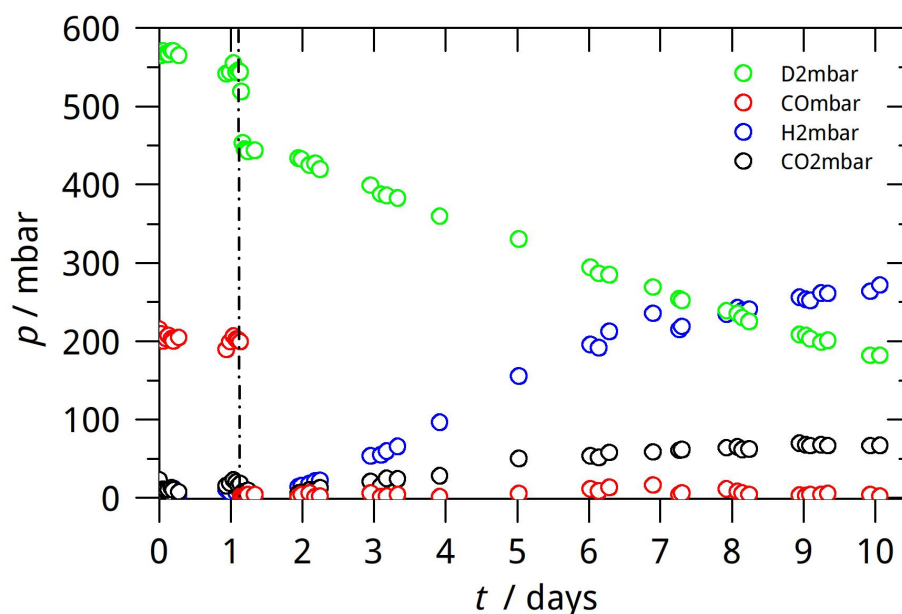


**Figure 5.14** – Kinetic plot showing the variation in partial pressures of H<sub>2</sub>, D<sub>2</sub>, CO<sub>2</sub> and CO above an *E. coli* culture supplemented with 98 mM glycerol which was grown in the presence of CO gas (20 %) in order to determine the impact of this competitive hydrogenase inhibitor on D<sub>2</sub> uptake and H<sub>2</sub> production. The first phase extends from 0-1 days with CO present. The second phase extends from 1-10 days where CO has been removed. In the presence of CO, no H<sub>2</sub> accumulation and only a very small reduction in D<sub>2</sub> is observed. Upon removal of CO, D<sub>2</sub> consumption along with CO<sub>2</sub> and H<sub>2</sub> production occurs after a recovery period of approximately 1 day. Data points depict a single representative measurement.<sup>117</sup>

## 5.4 Conclusions

Cavity-Enhanced Raman Spectroscopy (CERS) with optical feedback CW-diode lasers is a sensitive and selective analytical tool for *in situ*, multicomponent and isotope selective gas measurements. CERS setup has been employed to study hydrogen production and consumption by *E. coli*; under anaerobic conditions, cultures grown on either glucose or glycerol supplemented LB generate H<sub>2</sub> and CO<sub>2</sub> while simultaneously consuming some of the H<sub>2</sub> generated. By introducing D<sub>2</sub>, the hydrogen production and consumption processes can be separated due to the distinct spectroscopic signatures of each isotopomer. These experiments show that some of the D<sub>2</sub> consumed is converted back to H<sub>2</sub>, although HD is only formed as a minor component.

Although the measurements described here deal with a pure culture, mixed consortia of microorganisms, such as those obtained from biogas slurry, could prove

to be a more economical inoculant.<sup>153</sup> In these systems, heat treatment is required in order to remove methanogens which consume H<sub>2</sub> and generate methane (CH<sub>4</sub>). As previously demonstrated by our group,<sup>136</sup> CERS is able to distinguish H<sub>2</sub> and CH<sub>4</sub>, so a similar CERS-based approach could be useful for developing and optimizing these systems, confirming the absence of methanogenic organisms by checking the headspace for methane. Due to its unique analytical capabilities, CERS can supplement existing techniques to obtain relevant insights into the biochemistry of the uptake and production of gases and volatile species.

## Chapter 6 - Conclusions and Outlook

Existing and novel vibrational spectroscopic techniques (FTIR and CERS) have been applied to *in situ* headspace measurements of gases generated and consumed by *E. coli* as well as biologically relevant CO releasing agents.

A new, in house constructed 8 m path length White cell was designed, aligned and calibrated. The system was applied to the direct detection of N<sub>2</sub>O generated by *E. coli* during nitrate and nitrite respiration. Addition of nitrate led to a delayed response before the appearance of N<sub>2</sub>O, whereas addition of nitrite led to N<sub>2</sub>O appearing almost immediately in the headspace, reflecting the fact that nitrite and not nitrate is the source of NO *in vivo*. CO<sub>2</sub> production was also followed, although simultaneous pH measurements would be required to accurately calculate how the gas is partitioning between CO<sub>2</sub> and bicarbonate / carbonate in the solution phase. While the work by Wang *et al.* identifies Hcp as the major NO reductase at low NO concentrations (identifying the missing reductase activity was originally one of the main aims of the project) there is still considerable interest from our collaborators in following N<sub>2</sub>O production as part of a whole system metabolomics approach to studying the shift from mixed acid fermentation to nitrate respiration.<sup>50</sup> While the White cell was originally designed with H<sub>2</sub>S measurements in mind, work carried out in the group since the White cell construction was finished has suggested that more sensitive IR absorption techniques such as Herriot Enhanced Resonant Photoacoustic Spectroscopy (HERPAS) using NIR telecom laser diodes would be more suited to detection of this weakly absorbing analyte.

The high sensitivity of FTIR spectroscopy towards CO gas made the technique an obvious choice for studying CO release from antimicrobial CORMs. Measurements of CO release from [Mn(CO)<sub>3</sub>(tpa-κ<sup>3</sup>N)]<sup>+</sup> in thick cell suspensions showed that UV illumination even in deep, highly infected tissue would still be effective for CO release from this compound. Many synthetic groups are turning towards compounds which can be activated by visible or even NIR light to avoid many of the problems associated with UV light. In the case of CORM-3, the results reported agree with many of the findings previously reported in the literature regarding the importance of dithionite in triggering CO release from the complex. Despite evidence indicating that various amino acid residues may readily bind to the metal site, no significant CO

release was detected when these agents were incubated with CORM-3. Rather worryingly, CORM-3 is rapidly deactivated towards dithionite-triggered CO release in a variety of complex and defined media, phosphate buffer and even in non-buffered saline. No CO was observed in the headspace during incubation, indicating that the inactivation process is not due to loss of CO but either represents loss of CO as CO<sub>2</sub> or bicarbonate or the formation of a species where the CO ligands are no longer labile (e.g. [Ru(CO)<sub>3</sub>Cl<sub>3</sub>]<sup>-</sup>). Since incubation of the compound in both saline alone and phosphate buffer leads to the formation of non-CO releasing species, it seems likely that several deactivation pathways operate simultaneously in biological media.

While gas phase FTIR spectroscopy has proved to be extremely useful as an online CO release assay which can be utilised in a wider range of environments than standard biochemical assays, including non-aqueous solvents, water, buffer, complex media and cell suspensions, it provides little direct information about the fate of metal carbonyl itself. While solution phase FTIR spectroscopy is ideally suited to the study of metal carbonyls, particularly for rapid processes which appear to be occurring over the course of a few minutes, working in aqueous environments with dilute solutions is challenging. Possible solutions to this problem include moving to mixed alcohol / aqueous solvent systems (e.g. 50:50 methanol / water), using D<sub>2</sub>O rather than H<sub>2</sub>O to shift the solvent bands away from the carbonyl region and employing much higher concentrations of CORM-3 (10 mM rather than 500 or 100 μM). Electrospray MS could prove essential in identifying the final compounds generated from CORM-3 in buffer or from reaction with various biological ligands; in this case, the distinctive isotope pattern associated with Ru should aid in identifying different molecular ions generated during incubation in buffer.

This thesis presents the first conclusive report of photolytic CO release from CORM-3. Slow but definite photolytic CO release occurs upon illumination at 365 nm. This process does not appear to be deactivated in the same way as dithionite-triggered CO release as samples stored overnight in phosphate buffer were still able to release CO upon illumination. Further work would be required to identify the best wavelength for efficient photoactivation of the complex and to determine if more than one CO can be liberated using this approach (as is the case with CORM-2). While further work is required to explore the precise mechanisms of photolytic CO release from Ru(II) CORMs such as CORM-2 and 3, this result may indicate that a photolytic

pathway is the dominant route of CO release from CORM-3 *in vivo*. Taken together, these data show that the suitability of CORM-3 as a CO releasing agent for biological studies should be seriously reconsidered. While understanding the underlying deactivation process is an interesting chemical problem which is not addressed here, the findings reported in this thesis are sufficient to recommend that CORM-3 is no longer considered as a reliable CO releasing agent and that future biological studies should use alternative CORMs with cleaner CO releasing properties.

CERS has been successfully used for the first time to monitor H<sub>2</sub> metabolism by anaerobic cultures of *E. coli*. Analytical techniques based around Raman scattering, such as CERS, are much less sensitive to water vapour, a considerable advantage for biological measurements. Unlike many IR laser absorption techniques, and in common with broadband techniques such as FTIR spectroscopy, CERS can address all gaseous components in a simultaneously. Using N<sub>2</sub> as an internal standard, CERS can be run with passive optical locking, greatly simplifying the setup compared to previous iterations. *E. coli* grown anaerobically on glucose or glycerol supplemented LB generated H<sub>2</sub> and CO<sub>2</sub>, with some H<sub>2</sub> being consumed. Addition of D<sub>2</sub> to the headspace allowed the uptake / isotope exchange to be monitored as a function of time, with noticeable differences between the D<sub>2</sub> uptake behaviour observed in glycerol and glucose supplemented cultures. Addition of CO to the headspace entirely inhibited H<sub>2</sub> production and inhibited the vast majority of D<sub>2</sub> uptake activity consumption, indicating that Hyd-1 plays only a relatively minor role in hydrogen uptake under these conditions.

CERS schemes such as the one described here are widely applicable to a variety of systems ranging from could have a wide range of applications in from monitoring heterogeneous catalysis to gas adsorption. In a microbial setting, other areas which might potentially be of interest include the study of hydrogenotrophic methaogenesis, where H<sub>2</sub> and CO<sub>2</sub> are utilised to generate CH<sub>4</sub>, a molecule with a particularly large Raman cross-section. The ability of CERS to quantitatively detect N<sub>2</sub> with excellent time resolution makes is ideally equipped to study N<sub>2</sub> biochemistry. Two preliminary studies have already been published demonstrating that a CERS approach can be used to follow N<sub>2</sub> production by denitrifying bacteria and N<sub>2</sub> fixation by symbiotic diazotrophs from *Medicago sativa* root nodules.<sup>52,154</sup> The Hippler group is looking to expand this work further using a better defined system, namely the free-living

diazotrophic bacterium *Azotobacter vinelandii*. This organism can be relatively easily cultured on a defined nitrogen free medium under aerobic conditions. When grown in media lacking a suitable nitrogen source, *A. vinelandii* expresses nitrogenase, an enzyme which catalyses  $N_2$  reduction to ammonia (see Figure 6.1).<sup>155</sup> Nitrogenase is also able to reduce a number of other unsaturated molecules; the acetylene assay utilises the ability of nitrogenase to reduce acetylene ( $C_2H_2$ ) to ethylene ( $C_2H_4$ ) to quantify nitrogenase activity.<sup>156</sup> There is very little data concerning how the rate of acetylene reduction compares to the rate of reduction of the natural substrate. Since  $N_2$ ,  $C_2H_2$  and  $C_2H_4$  all have Raman active vibrational modes and partition reasonably favourably into the gas phase, a sensitive CERS setup could be used to directly compare the kinetics of  $N_2$  and  $C_2H_2$  reduction by live cultures or disrupted cells. In addition, *A. vinelandii* also possess interesting aerobic metabolism, with one of the fastest rates of  $O_2$  consumption which is believed to be necessary to protect the air sensitive nitrogenase cluster.<sup>157</sup>

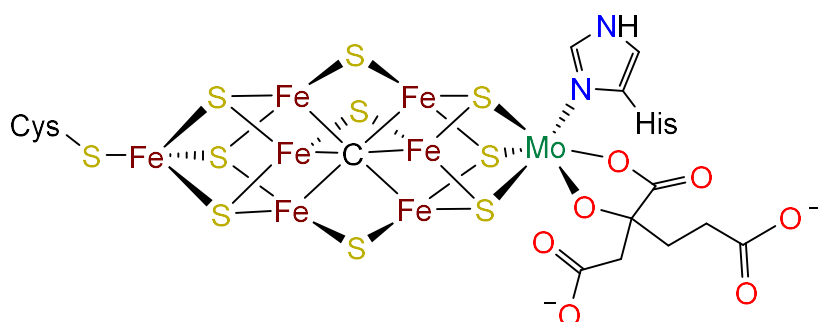


**Figure 6.1** – Active site structure of Mo nitrogenase consists of a unique iron sulfide cluster which is believed to coordinate  $N_2$  and reduce the molecule to two equivalents of  $NH_3$  in a stepwise manner.

The process of biological nitrogen fixation occurs with obligatory release of one molecule of  $H_2$  for every molecule of  $N_2$  fixed. While *A. vinelandii* expresses an  $O_2$  tolerant hydrogenase analogous to *E. coli* Hyd-1 which is believed to recover reducing equivalents by oxidising this  $H_2$ , it may be possible to measure  $H_2$  accumulation above a mutant strain lacking this hydrogenase using CERS, providing another direct measure of nitrogenase turnover.

Although CERS has proven to be a very useful technique for selective, online measurements of gases which are otherwise difficult to detect, the inherent weakness of spontaneous Raman scattering means that techniques such as CERS will never be able to compete with sensitive laser absorption experiments such as CRDS. Nevertheless, there are several improvements which could be made to improve sensitivity of the current system further. As Raman scales linearly with optical power, one relatively simple approach would be to use a more powerful diode laser as the excitation source for the experiment. While diode lasers with power outputs of 1 W or more exist, high power diode lasers are typically highly multimode in their emission, making them unsuitable for coupling into a high finesse optical cavity. Despite this, some of the diode lasers with slightly weaker outputs (< 200 mW optical output) may be forced to lase in a single mode when provided sufficient optical feedback; such an approach has been used successfully in amateur holography to obtain high power, stable single mode sources. The Hippler group is currently exploring the use of an external diffraction grating to stabilise a 150 mW 635 nm laser and force it to emit in a single longitudinal mode; early results are promising, although the laser has yet to be coupled into an optical cavity. In theory, this should lead to an order of magnitude increase in power build up within the optical cavity and a corresponding increase in the amount of Raman scattered light from the cavity.

While the Raman shift of a given transition is independent of the excitation wavelength, the strength of a transition is proportional to  $\lambda^{-4}$ . This means that moving towards short excitation wavelengths should lead to noticeable increases in the amount of Raman scattered light. In condensed phase Raman, short wavelength visible light is usually avoided due to enhanced fluorescence which drowns out the much weaker Raman light. For gas phase Raman, this is somewhat less of a concern as most small molecules electronic transitions are in the UV, meaning that shorter wavelength green or blue excitation could be used without significant sample fluorescence. Green, blue and violet laser diodes are becoming increasingly available due to their use in Blue-Ray<sup>TM</sup> optical disk technology, for laser cutting applications, for metrology and as excitation sources for flow cytometry. Clearly there is considerable scope for improvement of CERS in particular and numerous biological problems to which the technique could be applied

## References

- 1 L. S. Rothman, I. E. Gordon, Y. Babikov, A. Barbe, D. Chris Benner, P. F. Bernath, M. Birk, L. Bizzocchi, V. Boudon, L. R. Brown, A. Campargue, K. Chance, E. A. Cohen, L. H. Coudert, V. M. Devi, B. J. Drouin, A. Fayt, J. M. Flaud, R. R. Gamache, J. J. Harrison, J. M. Hartmann, C. Hill, J. T. Hodges, D. Jacquemart, A. Jolly, J. Lamouroux, R. J. Le Roy, G. Li, D. A. Long, O. M. Lyulin, C. J. Mackie, S. T. Massie, S. Mikhailenko, H. S. P. Müller, O. V Naumenko, A. V Nikitin, J. Orphal, V. Perevalov, A. Perrin, E. R. Polovtseva, C. Richard, M. A. H. Smith, E. Starikova, K. Sung, S. Tashkun, J. Tennyson, G. C. Toon, V. G. Tyuterev and G. Wagner, *J. Quant. Spectrosc. Radiat. Transf.*, 2013, **130**, 4–50.
- 2 B. Michielsen, J. J. J. Dom, B. J. van der Veken, S. Hesse, Z. Xue, M. A. Suhm and W. A. Herrebout, *Phys. Chem. Chem. Phys.*, 2010, **12**, 14034–14044.
- 3 S. Chung and M. Hippler, *J. Chem. Phys.*, 2006, **124**, 214316.
- 4 J. U. White, *J. Opt. Soc. Am.*, 1942, **32**, 285–288.
- 5 J.-F. Doussin, R. Dominique and C. Patrick, *Appl. Opt.*, 1999, **38**, 4145–4150.
- 6 D. R. Herriott and H. J. Schulte, *Appl. Opt.*, 1965, **4**, 883–889.
- 7 J. M. Herbelin, J. A. McKay, M. A. Kwok, R. H. Ueunten, D. S. Urevig, D. J. Spencer and D. J. Benard, *Appl. Opt.*, 1980, **19**, 144–147.
- 8 D. Z. Anderson, J. C. Frisch and C. S. Masser, *Appl. Opt.*, 1984, **23**, 1238–1245.
- 9 T. M. Crawford, 1985, vol. 540, pp. 540–548.
- 10 A. O’Keefe and D. A. G. Deacon, *Rev. Sci. Instrum.*, 1988, **59**, 2544–2551.
- 11 J. J. Scherer, J. B. Paul, C. P. Collier and R. J. Saykally, *J. Chem. Phys.*, 1995, **102**, 5190–5199.
- 12 A. A. Lukashetskaya, O. V Naumenko, S. Kassi and A. Campargue, *J. Mol. Spectrosc.*, 2017, **338**, 91–96.
- 13 M. Hippler and M. Quack, *Chem. Phys. Lett.*, 1999, **314**, 273–281.
- 14 T.-K. Huang, B.-J. Chen, K.-C. Lin, L. Lin, B.-J. Sun and A. H. H. Chang, *J. Phys. Chem. A*, 2017, **121**, 2888–2895.
- 15 D. Wang, R. Hu, P. Xie, J. Liu, W. Liu, M. Qin, L. Ling, Y. Zeng, H. Chen, X. Xing, G. Zhu, J. Wu, J. Duan, X. Lu and L. Shen, *J. Quant. Spectrosc. Radiat. Transf.*, 2015, **166**, 23–29.
- 16 T. Yu and M. C. Lin, *J. Am. Chem. Soc.*, 1993, **115**, 4371–4372.
- 17 M. Gaj, M. Beyer, P. Koeniger, H. Wanke, J. Hamutoko and T. Himmelsbach, *Hydrol. Earth Syst. Sci.*, 2016, **20**, 715–731.
- 18 H. Lin, Z. D. D. Reed, V. T. T. Sironneau and J. T. T. Hodges, *J. Quant.*

- Spectrosc. Radiat. Transf.*, 2015, **161**, 11–20.
- 19 E. R. Crosson, *Appl. Phys. B*, 2008, **92**, 403–408.
- 20 A. D. McCartt, T. J. Ognibene, G. Bench and K. W. Turteltaub, *Anal. Chem.*, 2016, **88**, 8714–8719.
- 21 G. Neri, A. Lacquaniti, G. Rizzo, N. Donato, M. Latino and M. Buemi, *Nephrol. Dial. Transplant.*, 2012, **27**, 2945–2952.
- 22 C. Wang, A. Mbi and M. Shepherd, *IEEE Sens. J.*, 2010, **10**, 54–63.
- 23 K. Stamy, O. Vaittinen, J. Jaakola, J. Guss, M. Metsälä, G. Johanson and L. Halonen, *Biomarkers*, 2009, **14**, 285–291.
- 24 A. O’Keefe, J. J. Scherer and J. B. Paul, *Chem. Phys. Lett.*, 1999, **307**, 343–349.
- 25 A. Cygan, D. Lisak, P. Masłowski, K. Bielska, S. Wójtewicz, J. Domysławska, R. S. Trawiński, R. Ciuryło, H. Abe and J. T. Hodges, *Rev. Sci. Instrum.*, 2011, **82**, 63107.
- 26 B. A. Paldus, C. C. Harb, T. G. Spence, B. Wilke, J. Xie, J. S. Harris and R. N. Zare, *J. Appl. Phys.*, 1998, **83**, 3991–3997.
- 27 Y. A. Bakhirkin, A. A. Kosterev, C. Roller, R. F. Curl and F. K. Tittel, *Appl. Opt.*, 2004, **43**, 2257–2266.
- 28 M. Hippler, C. Mohr, K. A. Keen and E. D. McNaghten, *J. Chem. Phys.*, 2010, **133**, 44308.
- 29 A. Kachanov, S. Koulikov and F. K. Tittel, *Appl. Phys. B Lasers Opt.*, , DOI:10.1007/s00340-012-5250-z.
- 30 R. Salter, J. Chu and M. Hippler, *Analyst*, 2012, **137**, 4669–4676.
- 31 A. Smekal, *Naturwissenschaften*, 1923, **11**, 873–875.
- 32 C. V. Raman, *Indian J. Phys.*, 1928, **2**, 368–376.
- 33 G. Landsberg and L. Mandelstam, *Naturwissenschaften*, 1928, **16**, 557–558.
- 34 M. Moskovits, *J. Raman Spectrosc.*, 2005, **36**, 485–496.
- 35 P. L. Stiles, J. A. Dieringer, N. C. Shah and R. P. Van Duyne, *Annu. Rev. Anal. Chem.*, 2008, **1**, 601–626.
- 36 S. Hanf, T. Bögözi, R. Keiner, T. Frosch and J. Popp, *Anal. Chem.*, , DOI:10.1021/ac503450y.
- 37 S. Hanf, R. Keiner, D. Yan, J. Popp and T. Frosch, *Anal. Chem.*, 2014, **86**, 5278–5285.
- 38 J. Thorstensen, K. H. Haugholt, A. Ferber, K. A. H. Bakke and J. Tschudi, *J. Eur. Opt. Soc. - Rapid Publ.*
- 39 R. Keiner, T. Frosch, S. Hanf, A. Rusznyak, D. M. Akob, K. Küsel and J. Popp,

- Anal. Chem.*, 2013, **85**, 8708–8714.
- 40 S. ZAITSU and T. IMASAKA, *Anal. Sci.*, 2014, **30**, 75–79.
- 41 G. Uden and J. Bongaerts, *Biochim. Biophys. Acta*, 1997, **1320**, 217–234.
- 42 F. Sargent, *Microbiology*, 2007, **153**, 633–651.
- 43 A. Arkenberg, S. Runkel, D. J. Richardson and G. Rowley, *Biochem. Soc. Trans.*, 2011, **39**, 1876–1879.
- 44 M. Mukai, C. E. Mills, R. K. Poole and S.-R. Yeh, *J. Biol. Chem.*, 2001, **276**, 7272–7277.
- 45 A. Bonamore and A. Boffi, *IUBMB Life*, 2008, **60**, 19–28.
- 46 M. T. Forrester and M. W. Foster, *Free Radic. Biol. Med.*, 2012, **52**, 1620–1633.
- 47 H. Corker and R. K. Poole, *J. Biol. Chem.*, 2003, **278**, 31584–31592.
- 48 A. M. Gardner, R. A. Helmick and P. R. Gardner, *J. Biol. Chem.*, 2002, **277**, 8172–8177.
- 49 C. E. Vine and J. A. Cole, *Biochem. Soc. Trans.*, 2011, **39**, 213–215.
- 50 J. Wang, C. E. Vine, B. K. Balasiny, J. Rizk, C. L. Bradley, M. Tinajero-Trejo, R. K. Poole, L. L. Bergaust, L. R. Bakken and J. A. Cole, *Mol. Microbiol.*, 2016, **100**, 877–892.
- 51 C. E. Vine, S. K. Purewal and J. A. Cole, *FEMS Microbiol. Lett.*, 2011, **325**, 108–114.
- 52 R. Keiner, M. Herrmann, K. Küsel, J. Popp and T. Frosch, *Anal. Chim. Acta*, 2015, **864**, 39–47.
- 53 M. D. Rolfe, A. Ter Beek, A. I. Graham, E. W. Trotter, H. M. S. Asif, G. Sanguinetti, J. T. de Mattos, R. K. Poole and J. Green, *J. Biol. Chem.*, 2011, **286**, 10147–10154.
- 54 W. C. Trogler, *Coord. Chem. Rev.*, 1999, **187**, 303–327.
- 55 J. T. Drummond and R. G. Matthews, *Biochemistry*, 1994, **33**, 3732–3741.
- 56 J. T. Drummond and R. G. Matthews, *Biochemistry*, 1994, **33**, 3742–3750.
- 57 M. Tinajero-Trejo, N. Rana, C. Nagel, H. E. Jesse, T. W. Smith, L. K. Wareham, M. Hippler, U. Schatzschneider and R. K. Poole, *Antioxid. Redox Signal.*, 2016, **24**, 765–780.
- 58 S. W. Ryter, J. Alam and A. M. K. Choi, *Physiol. Rev.*, 2006, **86**, 583 LP-650.
- 59 L. E. Otterbein, F. H. Bach, J. Alam, M. Soares, H. Tao Lu, M. Wysk, R. J. Davis, R. A. Flavell and A. M. K. Choi, *Nat Med*, 2000, **6**, 422–428.
- 60 L. E. Otterbein, L. L. Mantell and A. M. K. Choi, *Am. J. Physiol. - Lung Cell. Mol. Physiol.*, 1999, **276**, L688 LP-L694.

- 61 T. Fujita, K. Toda, A. Karimova, S.-F. Yan, Y. Naka, S.-F. Yet and D. J. Pinsky, *Nat Med*, 2001, **7**, 598–604.
- 62 A. Yachie, Y. Niida, T. Wada, N. Igarashi, H. Kaneda, T. Toma, K. Ohta, Y. Kasahara and S. Koizumi, *J. Clin. Invest.*, 1999, **103**, 129–135.
- 63 R. Stocker, Y. Yamamoto, A. F. McDonagh, A. N. Glazer and B. N. Ames, *Science (80-. )*, 1987, **235**, 1043 LP-1046.
- 64 B. E. Mann, *Organometallics*, 2012, **31**, 5728–5735.
- 65 E. Palao, T. Slanina, L. Muchová, T. Šolomek, L. Vitek and P. Klán, *J. Am. Chem. Soc.*, 2016, **138**, 126–133.
- 66 X. Ji, L. K. C. De La Cruz, Z. Pan, V. Chittavong and B. Wang, *Chem. Commun.*, 2017, **53**, 9628–9631.
- 67 L. A. P. Antony, T. Slanina, P. Šebej, T. Šolomek and P. Klán, *Org. Lett.*, 2013, **15**, 4552–4555.
- 68 F. Zobi, O. Blacque, R. A. Jacobs, M. C. Schaub and A. Y. Bogdanova, *Dalt. Trans.*, 2012, **41**, 370–378.
- 69 R. Motterlini, P. Sawle, J. Hammad, S. Bains, R. Alberto, R. Foresti and C. J. Green, *FASEB J.*, 2005, **19**, 284–286.
- 70 E. Kianfar, C. Schäfer, M. R. Lornejad-Schäfer, E. Portenkirchner and G. Knör, *Inorganica Chim. Acta*, 2015, **435**, 174–177.
- 71 H. Pfeiffer, A. Rojas, J. Niesel and U. Schatzschneider, *Dalt. Trans.*, 2009, 4292–4298.
- 72 S. Romanski, H. Rücker, E. Stamellou, M. Guttentag, J.-M. J.-M. Neudörfl, R. Alberto, S. Amslinger, B. Yard and H.-G. H.-G. Schmalz, *Organometallics*, 2012, **31**, 5800–5809.
- 73 L. Mond, C. Langer and F. Quincke, *J. Chem. Soc. Trans.*, 1890, **57**, 749–753.
- 74 M. Beller, B. Cornils, C. D. Frohning and C. W. Kohlpaintner, *J. Mol. Catal. A Chem.*, 1995, **104**, 17–85.
- 75 P. M. Maitlis, A. Haynes, G. J. Sunley and M. J. Howard, *J. Chem. Soc. Dalt. Trans.*, 1996, 2187–2196.
- 76 J. H. Jones, *Platin. Met. Rev.*, 2000, **44**, 94–105.
- 77 C. M. Thomas and G. Süß-Fink, *Coord. Chem. Rev.*, 2003, **243**, 125–142.
- 78 R. Motterlini, J. E. Clark, R. Foresti, P. Sarathchandra, B. E. Mann and C. J. Green, *Circ. Res.*, 2002, **90**, e17 LP-e24.
- 79 L. K. Wareham, R. K. Poole and M. Tinajero-Trejo, *J. Biol. Chem.*, 2015, **290**, 18999–19007.
- 80 M. Desmard, K. S. Davidge, O. Bouvet, D. Morin, D. Roux, R. Foresti, J. D. Ricard, E. Denamur, R. K. Poole, P. Montravers, R. Motterlini and J.

- Boczkowski, *FASEB J.*, 2009, **23**, 1023–1031.
- 81 H. Smith, B. E. Mann, R. Motterlini and R. K. Poole, *IUBMB Life*, , DOI:10.1002/iub.476.
- 82 A. F. N. Tavares, M. Teixeira, C. C. Romão, J. D. Seixas, L. S. Nobre and L. M. Saraiva, *J. Biol. Chem.* , 2011, **286**, 26708–26717.
- 83 J. L. Wilson, H. E. Jesse, B. Hughes, V. Lund, K. Naylor, K. S. Davidge, G. M. Cook, B. E. Mann and R. K. Poole, *Antioxid. Redox Signal.*, 2013, **19**, 497–509.
- 84 J. S. Ward, R. Morgan, J. M. Lynam, I. J. S. Fairlamb and J. W. B. Moir, *Medchemcomm*, 2017, **8**, 346–352.
- 85 J. S. Ward, J. M. Lynam, J. Moir and I. J. S. Fairlamb, *Chem. – A Eur. J.*, 2014, **20**, 15061–15068.
- 86 T. S. Murray, C. Okegbe, Y. Gao, B. I. Kazmierczak, R. Motterlini, L. E. P. Dietrich and E. M. Bruscia, *PLoS One*, 2012, **7**, e35499.
- 87 A. F. N. Tavares, L. S. Nobre and L. M. Saraiva, *FEMS Microbiol. Lett.*, 2012, **336**, 1–10.
- 88 L. S. Nobre, H. Jeremias, C. C. Romao and L. M. Saraiva, *Dalt. Trans.*, 2016, **45**, 1455–1466.
- 89 M. Desmard, R. Foresti, D. Morin, M. Dagouassat, A. Berdeaux, E. Denamur, S. H. Crook, B. E. Mann, D. Scapens, P. Montravers, J. Boczkowski and R. Motterlini, *Antioxid. Redox Signal.*, 2011, **16**, 153–163.
- 90 T. Santos-Silva, A. Mukhopadhyay, J. D. Seixas, G. J. L. Bernardes, C. C. Romão and M. J. Romão, *J. Am. Chem. Soc.*, 2011, **133**, 1192–1195.
- 91 M. F. A. Santos, J. D. Seixas, A. C. Coelho, A. Mukhopadhyay, P. M. Reis, M. J. Romão, C. C. Romão and T. Santos-Silva, *J. Inorg. Biochem.*, 2012, **117**, 285–291.
- 92 K. Fujita, Y. Tanaka, T. Sho, S. Ozeki, S. Abe, T. Hikage, T. Kuchimaru, S. Kizaka-Kondoh and T. Ueno, *J. Am. Chem. Soc.*, 2014, **136**, 16902–16908.
- 93 N. Pontillo, G. Ferraro, L. Messori, G. Tamasi and A. Merlino, *Dalt. Trans.*, 2017, **46**, 9621–9629.
- 94 C. Nagel, S. McLean, R. K. Poole, H. Braunschweig, T. Kramer and U. Schatzschneider, *Dalt. Trans.*, 2014, **43**, 9986–9997.
- 95 M. Klein, U. Neugebauer, M. Schmitt and J. Popp, *ChemPhysChem*, 2016, **17**, 985–993.
- 96 M. Klein, U. Neugebauer, A. Gheisari, A. Malassa, T. M. A. Jazzazi, F. Froehlich, M. Westerhausen, M. Schmitt and J. Popp, *J. Phys. Chem. A*, 2014, **118**, 5381–5390.
- 97 H. T. Poh, B. T. Sim, T. S. Chwee, W. K. Leong and W. Y. Fan, *Organometallics*, 2014, **33**, 959–963.

- 98 R. D. Rimmer, H. Richter and P. C. Ford, *Inorg. Chem.*, 2010, **49**, 1180–1185.
- 99 K. Nakamoto, in *Infrared and Raman Spectra of Inorganic and Coordination Compounds*, John Wiley & Sons, Inc., 2008, pp. 275–331.
- 100 G. Succo, S. Rosso, G. L. Fadda, M. Fantini and E. Crosetti, *Photodiagnosis Photodyn. Ther.*, 2014, **11**, 63–70.
- 101 S. Bonnet, *Comments Inorg. Chem.*, 2015, **35**, 179–213.
- 102 I. Chakraborty, S. J. Carrington and P. K. Mascharak, *ChemMedChem*, 2014, **9**, 1266–1274.
- 103 S. J. Carrington, I. Chakraborty, J. M. L. Bernard and P. K. Mascharak, *ACS Med. Chem. Lett.*, 2014, **5**, 1324–1328.
- 104 A. E. Pierri, P.-J. Huang, J. V Garcia, J. G. Stanfill, M. Chui, G. Wu, N. Zheng and P. C. Ford, *Chem. Commun.*, 2015, **51**, 2072–2075.
- 105 J. E. Clark, P. Naughton, S. Shurey, C. J. Green, T. R. Johnson, B. E. Mann, R. Foresti and R. Motterlini, *Circ. Res.*, 2003, **93**, e2–e8.
- 106 L. S. Nobre, F. Al-Shahrour, J. Dopazo and L. M. Saraiva, *Microbiology*, 2009, **155**, 813–824.
- 107 S. McLean, B. E. Mann and R. K. Poole, *Anal. Biochem.*, 2012, **427**, 36–40.
- 108 T. R. Johnson, B. E. Mann, I. P. Teasdale, H. Adams, R. Foresti, C. J. Green and R. Motterlini, *Dalt. Trans.*, 2007, 1500–1508.
- 109 K. Tsoyi, Y. M. Ha, Y. M. Kim, Y. S. Lee, H. J. Kim, H. J. Kim, H. G. Seo, J. H. Lee and K. C. Chang, *Inflammation*, 2009, **32**, 364.
- 110 C. I. Schwer, P. Stoll, S. Rospert, E. Fitzke, N. Schallner, H. Bürkle, R. Schmidt and M. Humar, *Int. J. Biochem. Cell Biol.*, 2013, **45**, 201–212.
- 111 H. Soni, P. Patel, A. C. Rath, M. Jain and A. A. Mehta, *Vascul. Pharmacol.*, 2010, **53**, 68–76.
- 112 W. J. Wilkinson and P. J. Kemp, *Purinergic Signal.*, 2011, **7**, 57–64.
- 113 L. Tong, K. N. Yu, L. Bao, W. Wu, H. Wang and W. Han, *Mutat. Res. Mol. Mech. Mutagen.*, 2014, **759**, 9–15.
- 114 M. Feger, A. Fajol, A. Lebedeva, A. Meissner, D. Michael, J. Voelkl, I. Alesutan, E. Schleicher, C. Reichetzeder, B. Hoher, S. M. Qadri and F. Lang, *Kidney Blood Press. Res.*, 2013, **37**, 496–505.
- 115 R. G. Rinker, T. P. Gordon, D. M. Mason and W. H. Corcoran, *J. Phys. Chem.*, 1959, **63**, 302.
- 116 J. P. Lomont, S. C. Nguyen and C. B. Harris, *Organometallics*, 2014, **33**, 6179–6185.
- 117 T. W. Smith and M. Hippler, *Anal. Chem.*, 2017, **89**, 2147–2154.
- 118 R. F. Service, *Science*, 2009, **324**, 1257–1259.

- 119 S. E. Hosseini and M. A. Wahid, *Renew. Sustain. Energy Rev.*, 2016, **57**, 850–866.
- 120 U. Eberle, M. Felderhoff and F. Schüth, *Angew. Chemie Int. Ed.*, 2009, **48**, 6608–6630.
- 121 J. Turner, G. Sverdrup, M. K. Mann, P.-C. Maness, B. Kroposki, M. Ghirardi, R. J. Evans and D. Blake, *Int. J. Energy Res.*, 2008, **32**, 379–407.
- 122 N. Armaroli and V. Balzani, *Angew. Chemie Int. Ed.*, 2007, **46**, 52–66.
- 123 N. H. M. Yasin, T. Mumtaz, M. A. Hassan and N. Abd Rahman, *J. Environ. Manage.*, 2013, **130**, 375–385.
- 124 K. Y. Show, D. J. Lee, J. H. Tay, C. Y. Lin and J. S. Chang, *Int. J. Hydrogen Energy*, 2012, **37**, 15616–15631.
- 125 H.-S. Lee, W. F. J. Vermaas and B. E. Rittmann, *Trends Biotechnol.*, 2010, **28**, 262–271.
- 126 W. Lubitz, H. Ogata, O. Rüdiger and E. Reijerse, *Chem. Rev.*, 2014, **114**, 4081–4148.
- 127 K. Vijayaraghavan, R. Karthik and S. P. Kamala Nalini, *Int. J. Hydrogen Energy*, 2009, **34**, 7964–7970.
- 128 M. Saleem, M. H. Chakrabarti, A. A. Abdul Raman, D. B. Hasan, W. M. Ashri Wan Daud and A. Mustafa, *Int. J. Hydrogen Energy*, 2012, **37**, 4930–4934.
- 129 J. E. W. Polle, S. Kanakagiri, E. Jin, T. Masuda and A. Melis, *Int. J. Hydrogen Energy*, 2002, **27**, 1257–1264.
- 130 N. Basak and D. Das, *World J. Microbiol. Biotechnol.*, 2007, **23**, 31–42.
- 131 G. Davila-Vazquez, S. Arriaga, F. Alatraste-Mondragón, A. de León-Rodríguez, L. M. Rosales-Colunga and E. Razo-Flores, *Rev. Environ. Sci. Bio/Technology*, 2008, **7**, 27–45.
- 132 F. Sargent, in *Advances in Microbial Physiology*, ed. K. P. Robert, Academic Press, 2016, vol. Volume 68, pp. 433–507.
- 133 C. Pinske, M. Jaroschinsky, S. Linek, C. L. Kelly, F. Sargent and R. G. Sawers, *J. Bacteriol.*, 2015, **197**, 296–306.
- 134 J. S. McDowall, B. J. Murphy, M. Haumann, T. Palmer, F. A. Armstrong and F. Sargent, *Proc. Natl. Acad. Sci.*, 2014, **111**, E3948–E3956.
- 135 S. C. Andrews, B. C. Berks, J. McClay, A. Ambler, M. A. Quail, P. Golby and J. R. Guest, *Microbiology*, 1997, **143**, 3633–3647.
- 136 M. Hippler, *Anal. Chem.*, 2015, **87**, 7803–7809.
- 137 O. Elsharnouby, H. Hafez, G. Nakhla and M. H. El Nagggar, *Int. J. Hydrogen Energy*, 2013, **38**, 4945–4966.
- 138 T. Maeda, V. Sanchez-Torres and T. K. Wood, *Appl. Microbiol. Biotechnol.*,

- 2007, **77**, 879–890.
- 139 T. Maeda, V. Sanchez-Torres and T. K. Wood, *Microb. Biotechnol.*, 2008, **1**, 30–39.
- 140 C. Pinske and F. Sargent, *Microbiologyopen*, 2016, **5**, 721–737.
- 141 M. Roger, F. Brown, W. Gabrielli and F. Sargent, *Curr. Biol.*, 2018, **28**, 140–145.e2.
- 142 R. Dobson, V. Gray and K. Rumbold, *J. Ind. Microbiol. Biotechnol.*, 2012, **39**, 217–226.
- 143 K. Trchounian and A. Trchounian, *Renew. Energy*, 2015, **83**, 345–351.
- 144 Y. Dharmadi, A. Murarka and R. Gonzalez, *Biotechnol. Bioeng.*, 2006, **94**, 821–829.
- 145 J. M. Clomburg and R. Gonzalez, *Trends Biotechnol.*, 2013, **31**, 20–28.
- 146 A. Murarka, Y. Dharmadi, S. S. Yazdani and R. Gonzalez, *Appl. Environ. Microbiol.*, 2008, **74**, 1124–1135.
- 147 P. M. Vignais, *Coord. Chem. Rev.*, 2005, **249**, 1677–1690.
- 148 H. McTavish, L. A. Sayavedra-Soto and D. J. Arp, *Biochim. Biophys. Acta - Protein Struct. Mol. Enzymol.*, 1996, **1294**, 183–190.
- 149 M. Bernhard, T. Buhrke, B. Bleijlevens, A. L. De Lacey, V. M. Fernandez, S. P. J. Albracht and B. Friedrich, *J. Biol. Chem.*, 2001, **276**, 15592–15597.
- 150 M. J. Lukey, M. M. Roessler, A. Parkin, R. M. Evans, R. A. Davies, O. Lenz, B. Friedrich, F. Sargent and F. A. Armstrong, *J. Am. Chem. Soc.*, 2011, **133**, 16881–16892.
- 151 N. Tamiya and S. L. Miller, *J. Biol. Chem.*, 1963, **238**, 2194–2198.
- 152 K. A. Vincent, J. A. Cracknell, O. Lenz, I. Zebger, B. Friedrich and F. A. Armstrong, *Proc. Natl. Acad. Sci. U. S. A.*, 2005, **102**, 16951–16954.
- 153 C. Li and H. H. P. Fang, *Crit. Rev. Environ. Sci. Technol.*, 2007, **37**, 1–39.
- 154 T. Jochum, A. Fastnacht, S. E. Trumbore, J. Popp and T. Frosch, *Anal. Chem.*, , DOI:10.1021/acs.analchem.6b03101.
- 155 Y. Hu and M. W. Ribbe, *J. Biol. Inorg. Chem.*, 2015, **20**, 435–445.
- 156 N. Cassar, J. P. Bellenger, R. B. Jackson, J. Karr and B. A. Barnett, *Oecologia*, , DOI:10.1007/s00442-011-2105-y.
- 157 M. J. S. Kelly, R. K. Poole, M. G. Yates and C. Kennedy, *J. Bacteriol.*, 1990, **172**, 6010–6019.

